Coherent gas flow patterns in heterogeneous permeability fields: From bench-scale to field-scale

To the Faculty of Geosciences, Geo-Engineering and Mining
of the Technische Universität Bergakademie Freiberg
is submitted this

THESIS

to attain the academic degree of
Doktor-Ingenieur
Dr. -Ing.

by   Msc. Shirin Samani

born on the   22.03.1983 in Shahrekord (Iran)

Referees: Prof. Dr. Helmut Geistlinger, Halle
                Prof. Dr. Broder J. Merkel, Freiberg

Freiberg, 8.2.2012

Abstract

Gas injection into saturated porous media has a high practical relevance. It is applied in groundwater remediation (air sparging), in CO_2 sequestration into saline aquifers, and in enhanced oil recovery of petroleum reservoirs. This wide range of application necessitates a comprehensive understanding of gas flow patterns that may develop within the porous media and required modeling of multi-phase flow. There is an ongoing controversy in literature, if continuum models are able to describe the complex flow pattern observed in heterogeneous porous media, especially the channelized stochastic flow pattern. Based on Selker's stochastic hypothesis, a gas channel is caused by a Brownian-motion process during gas injection. Therefore, the pore-scale heterogeneity will determine the shape of the single stochastic gas channels. On the other hand there are many studies on air sparging, which are based on continuum modeling. Up to date it is not clear under which conditions a continuum model can describe the essential features of the complex gas flow pattern. The aim of this study is to investigate the gas flow pattern on bench-scale and field scale using the continuum model TOUGH2. Based on a comprehensive data set of bench-scale experiments and field-scale experiments, we conduct for the first time a systematic study and evaluate the prediction ability of the continuum model.

A second focus of this study is the development of a "real world"-continuum model, since on all scales – pore-scale, bench scale, field scale – heterogeneity is a key driver for the stochastic gas flow pattern. Therefore, we use different geostatistical programs to include stochastic conditioned and unconditioned parameter fields.

Our main conclusion from bench-scale experiments is that a continuum model, which is calibrated by different independent measurements, has excellent prediction ability for the average flow behavior (e.g. the gas volume-injection rate relation). Moreover, we investigate the impact of both weak and strong heterogeneous parameter fields (permeability and capillary pressure) on gas flow pattern. The results show that a continuum model with weak stochastic heterogeneity cannot represent the essential features of the experimental gas flow pattern (e.g., the single stochastic gas channels). Contrary, applying a strong heterogeneity the continuum model can represent the channelized flow. This observation supports Stauffer's statement that a so-called sub-scale continuum model with strong heterogeneity is able to describe the channelized flow behavior. On the other hand, we compare the theoretical integral gas volumes with our experiments and found that strong heterogeneity always yields too large gas volumes.

At field-scale the 3D continuum model is used to design and optimize the direct gas injection technology. The field-scale study is based on the working hypotheses that the key parameters are the same as at bench-scale. Therefore, we assume that grain size and injection rate will determine whether coherent channelized flow or incoherent bubbly flow will develop at field-scale. The results of four different injection regimes were compared with the data of the corresponding field experiments. The main conclusion is that because of the buoyancy driven gas flow the vertical permeability has a crucial impact. Hence, the vertical and horizontal permeability should be implemented independently in numerical modeling by conditioned parameter fields.

Acknowledgement

Table of Contents

List of Figures

List of Tables

Nomenclature

a	Practical range
A	Cross-sectional area
ΔA_{LG}	Interface area between liquid and gas fluids
c_ϕ	Compressibility of porosity
d_k	Diameter of glass beads
$d_{k,critical}$	Critical grain diameter (to establish incoherent flow)
d_{lead}	Diameter of lead sphere
d_m	Mean particle size in Kozeny-Carman equation
d_{max}	Maximum pore diameter
d_{min}	Minimum pore diameter
$f(r)$	pdf function of pore radii
F_B	Buoyancy force
F_C	Capillary force
F_P	Pressure force
F_v	Viscous force
g	Gravitational acceleration
h	Piezometric head
h_a	Real entry pressure of a porous medium
$h(S_e)$	Matrix potential
I_g	Volumetric mass rate of production and injection of gas phase
I_i	Volumetric mass rate of production or injection of phase i
I_w	Volumetric mass rate of production and injection of water phase
$J(S_{wet})$	Leverett J-function
k	Absolute permeability value
k_{exp}	Experimental permeability value
k_{KC}	Permeability value by Kozeny-Carman
k_{mean}	Mean value of stochastic permeability field
$k_n{}'$	Modified permeability value of grid block n
k_n	Absolute permeability value of grid block n
k_{ri}	Relative permeability function of phase i
$k_{r\,nwet}$	Relative permeability function of non-wetting phase
$k_{r\,wet}$	Relative permeability function of wetting phase
k_{rg}	Relative permeability function of gas phases
k_{rw}	Relative permeability function of water phase
K	Coefficient of proportionality in Darcy law
l	Specific length
l_x, l_y and l_z	Dimension of grid block in TOUGH2 simulation in x-, y- and z-direction
L	Filter length
L_{ch}	Length of gas channel
$L_{cluster}$	Length of isolated gas cluster
L_x, L_y and L_z	Dimension of model in TOUGH2 simulation in x-, y- and z-direction
m	Parameter of van Genuchten-Mualem model $\left(=1-1/n\right)$
M	Viscosity ratio

n	Pore size distribution index in van Genuchten-Mualem model (1980)
N_B	Bond number
$N_B{}^*$	Modified Bond number
N_C	Capillary number
$N_{C,classic}$	Classical Capillary number
$N(l)$	Total numbers of data exist within length l
P	Pore pressure
P_c	Capillary pressure value
$P_c(S_{wet})$	Capillary pressure-saturation relationship
$P_{c,bubble}$	Capillary pressure of a trapped gas bubble
$P_{c,channel}$	Capillary pressure of a stable gas channel
$P_{c,n}$	Capillary pressure of grid block n
$P_{c,n}{}'$	Modified capillary pressure of grid block n
P_g	Gas pressure
P_e	Entry pressure
P_i	Pressure of phase i
P_{nwet}	Pressure of the non-wetting fluid
P_w	Pressure of water
P_{wet}	Pressure of the wetting fluid
q_i	Volumetric flux of the phase i
q_g	Volumetric flux of gas phase
q_w	Volumetric flux of water phase
Q	Volumetric flow rate of water
Q_{ch}	Flow rate through a macro channel
$Q_{critical}$	Critical flow rate (to establish stable channelized flow)
Q_g	Gas injection flow rate
Q_{exp}	Experimental flow rate
Q_{pore}	Flow rate through a micro channel
Q_{total}	Total flow rate
r	Pore radius
r_1 and r_2	Principle radii of a curved surface
r_b	Radius of spherical gas bubble
r_c	Mean pore radius
r_{ch}	Radius of gas channel
r_{gf}	Smallest gas-filled capillary radius
r_m	Mean value of pore size distribution
r_{th}	Radius of pore throat
s	Thickness
S_e	Effective saturation of wetting phase
S_g	Gas saturation
S_{eq}	Equilibrium saturation of the non-wetting phase
S_i	Saturation of phase i
S_m	Maximum saturation of wetting phase
S_{min}	Minimum saturation of wetting phase in capillary pressure curve
S_w	Water saturation
S_{wet}	Saturation of wetting phase
$S_{wet\,r}$	Residual saturation of wetting phase
t	Time
v	Velocity of fluid parallel to the boundary layer

v_g	Average flow velocity of gas phase
v_j - v_k	Difference between parameters that lay within the specific length l
V	Bulk volume
$V_{cap}(r)$	Volume of a capillary with radius r
V_g	Volume of gas phase
V_p	Volume of void space
V_w	Volume of water phase
z	Elevation
Z	Coordination number

Greek Letters

α	Aspect ratio equals to r_{th}/r_b
α_p	Reciprocal of entry pressure
$\gamma(l)$	Variogram
Δ	Difference (e.g., $\Delta\rho = \rho_{water} - \rho_{gas}$)
ζ_{min}	Minimum dimensionless diameter in units of d_k
ζ_{max}	Maximum dimensionless diameter in units of d_k
ζ_n	Permeability modifier of grid block n
θ	Contact angle
θ_g	Volumetric content of gas phase
θ_i	Volumetric content of phase i
θ_w	Volumetric content of water phase
λ	Pore size distribution index
λ_{nwet}	Tortuosity ratio of the non-wetting phase
λ_{wet}	Tortuosity ratio of the wetting phase
μ_g	Dynamic viscosity of gas phase
μ	Dynamic viscosity
ρ_g	Density of gas phase
ρ_i	Density of phase i
ρ_{lead}	Density of lead sphere
ρ_w	Density of water phase
σ_{dev}	Standard deviation of pore size distribution
σ_{GL}	Surface tension between gas and liquid phases
σ_k	Standard deviation of permeability field
σ_k^2	Variance of stochastic permeability field
σ_{SG}	Interfacial tension of solid and gas phases
σ_{SL}	Interfacial tension of solid and liquid phases
$\sigma_{wet,nwet}$	Interfacial tension of wetting and non-wetting fluids
$\sigma_{w,g}$	Interfacial tension between water and gas phases
τ_s	Shear stress
τ	Tortuosity factor
ϕ	Porosity

Subscripts

c	Capillary
g	Gas phase
i	Phase (e.g., water and gas)
n	Grid block
$nwet$	Non-wetting phase
r	Relative
w	Water phase
wet	Wetting phase

Acknowledgement

1   Introduction

This study is concerned with the gas flow patterns occurred in the gas injection processes, which are often considered in groundwater remediation, soil physics studies, and petroleum engineering. In this context, experimental investigations are required to study different gas flow pattern through the porous media. On the other hand, mathematical modeling is needed to simulate the gas injection and predict the performance of injection processes.

This study investigates and analyzes the numerical simulation of complex processes occurred within the porous media by the direct gas injection. The results of direct gas injection, which were carried out in bench-scale and at field-scale experiments, are considered to calibrate the simulation model. Then, the injection processes at these two scales were simulated to examine the ability of continuum model in representing different gas flow patterns. One focus of this study is to include the "real world" into the model by applying the stochastic hydrogeology. This work follows Rubin's paradigm, which states that all data must be included into the conditioned stochastic parameter fields to reduce the uncertainty in the model prognoses (see Rubin, 2003).

Therefore, experimental observations and simulation results of direct gas injection are used to find the elaborate answers to some of the unresolved questions. For instance, if the stochastic simulation by a continuum model can represent the gas channels of the coherent channelized flow pattern.

The first section of this chapter will emphasize the indistinct situation of stochastic simulation by continuum model and expresses the motivation of the work. The literature review on characterization and classification of gas flow patterns, and attempts of continuum modeling will be presented in section 1.2. The section 1.3 will list specific objectives of this dissertation. Furthermore, section 1.3 will give the scope and brief overview of the next following chapters.

1.1   Motivation

Different gas flow patterns may occur during the gas injection into the saturated porous media. Since many years, air and oxygen gas has been injected into the contaminated aquifer to remediate the organic contaminants. Gas injection process is applied not only in remediation technology, but also in CO_2 sequestration in saline aquifers, and enhanced oil recovery (EOR) in petroleum reservoirs. This wide range of application necessitates the comprehensive understanding of gas flow patterns that may develop within the porous media and required modeling of multi-phase flow. Many detailed studies are focused on investigating the multi-phase flow within the heterogeneous porous media. There is a controversy, if continuum models are able to describe the complex flow pattern observed in the heterogeneous porous media. Therefore, this work motivates to model the channelized flow pattern, which was observed in laboratory experiments, by a continuum model. To perform the modeling, TOUGH2 program (Pruess, 1999) is used, which is accepted and verified several times in literature of fluid flow and remediation technology. Moreover, it is motivated to examine whether the results of bench-scale experiments can be generalized for larger scales.

1.2   Literature review

Modern chemistry of Western civilization is based on chemical products (e.g., gasoline for cars, fertilizers for agriculture, polymers for semi-conductors, etc.). All these chemicals are potential pollutants of the environment, and especially the subsurface and the groundwater. And, many organic compounds (e.g., aromatics, polycyclic aromatic hydrocarbons, and chlorinated hydrocarbons) are hazardous for the human health and the environment.

Therefore, several remediation techniques have been used to clean up these organic contaminations (Semprini et al., 1990; Lee and Raymond, 1991; Johnson et al., 1993; Wilson et al., 1997; Schirmer, 2001). For example, air injection is frequently used to remove the dissolved volatile organic compounds (VOC) and non-aqueous phase liquid (NAPL) contaminants such as gasoline, jet fuel and chlorinated solvents (McCray, 2000). In air sparging process, the VOC- or NAPL-phase are carried by air and then collected by a soil vapor extraction (SVE) system.

Many of these organic contaminations migrate (or remove) as a separate phase through the groundwater because of low miscibility of contaminant in water. Therefore, a part of organic contaminant remains within the porous medium behind the mobilized water, and trapped by the capillary forces. The hydraulic remediation techniques (e.g., SVE) cannot recover most of the trapped contaminants. Therefore, in situ biodegradation becomes important, because it can reach to the trapped contaminants. In addition, the biodegradation process results in a complete and irreversible transformation of contaminants to the non-toxic compounds (Beckmann, 2006). Hence, biodegradation process, in which the direct gas injection is used to stimulate the bioremediation processes, is used as a low-cost and efficient remediation technology (Johnson et al., 1998; Brooks et al., 1999; McCray, 2000; Thomson and Johnson, 2000; Johnson et al., 2002; Geistlinger et al., 2006). Likewise, the mass transfer from gas phase into the water phase, the gas phase distribution is a key parameter in biodegradation technique, because higher gas saturation results in higher concentration of dissolved gas in water.

Therefore, determining the gas flow pattern is essential to optimize the gas injection, minimize the costs and achieve a successful injection process. Table 1.1 summarized the comprehensive laboratory experiments conducted to study the gas distribution and gas flow patterns.

Table 1.1: Overview of laboratory experiments performed to investigate the gas flow patterns (Krauss, 2007).

Method	Dimension of experimental set-up (cm)	Grain size, d (mm)	Investigation target	Gas injection rate (L/min)	Gas saturation	Citation
Column	10 × 30 19 × 90	Sand: d = 0.2-0.6 / 0.3-0.8 / 0.6-1.4 / 2.0-3.0 / 5.0-8.0	Air saturation, flow pattern	0.33-33	#	Brauns and Wehrle (1989)
Column	17.8 × 38.1	Course sand, fine sand	Gas distribution, air saturation	0.03-0.35	0.1-0.5	Chen et al. (1996)
Column	120 × 65	Quartz-sand: d = 0.46	Gas distribution	62-283	#	Hein et al. (1997)
Column	3.9 × 90 3.6 × 90	Glass beads: d = 4	Migration of individual air bubble	#	#	Roosevelt and Corapcioglu (1998)

Column	6	Sand: d = 0.16 / 0.21 / 0.27 / 0.36 / 0.46 / 0.61 / 0.72 / 0.92 / 1.35	Gas distribution, air saturation	#	0.02-0.14	Clayton (1998)
Column	5.3 × 30	Glass beads: d = 0.42-0.5 / 0.71-0.8 / 1 / 1.5 / 2 / 3	Air saturation, flow pattern	0.02-2	Dynamic: 0.1-0.35 Residual: 0.05-0.20	Brooks et al. (1999)
Column	7.6 × 28.6	Silty sand	Air saturation, flow pattern	#	0.3-0.8	Wong and Wibowo (2000)
Column	58 × 67	Medium sand, d = 0.25	Distribution of gas through capillaries	0.025-0.65	#	Lazik et al. (2002)
Tank	120 × 84 × 80	Sand: d = 0.2-0.6 / 0.3-0.8 / 0.6-1.4 / 2.0-3.0 / 5.0-8.0	Air saturation, flow pattern	0.33-33	Dynamic: 0.05-0.3 Residual: 0.04-0.18	Brauns and Wehrle (1989)
Tank	73 × 88 × 2.54	Glass beads: d = 0.2 / 0.3 / 0.4 / 0.75 / 2 / 4	Flow pattern	0.6-10	Dynamic: up to 0.5	Ji et al. (1993)
Tank	61 × 38 × 25	Gravel / sand: d = 15 / 4.5 / 0.75	Flow pattern	3 - 30	#	Semer et al. (1998)
Tank	90 × 90 × 2.5	Sand: d = 1.1 / 1.3 / 1.84 / 2.61 / 3.1 / 4.38	Flow pattern	0.2-1.1	0.09-0.25	Peterson et al. (1999)
Tank	40 × 44 × 3.8	Glass beads: d = 0.1-0.3 / 0.1-3 / 1-3	Size and length of gas channel	0.35-17	0.09-0.46	Elder and Benson (1999)
Tank	10×18.5×4	Sand: d = 0.305 / 0.190 / 0.168	Injection rate and distribution of gas channels	0.045-0.125	#	Rogers and Say Kee (2000)
Tank	91 × 72 × 10	Sand: d = 0.55	Influence of water flow on air injection zone	2.5, 4.7	#	Reddy and Adams (2000)
Tank	91 × 72 × 10	Gravel / sand: d = 4.5 / 0.66 / 0.52 / 0.12	Soil heterogeneity, flow pattern	2.5	#	Reddy and Adams (2001)
Tank	102 × 102 × 5 252 × 127 × 9	Sand: d = 0.07-0.3 / >0.18 / <0.212	Flow pattern, gas distribution	0.33-2.4	0.28	Peterson et al. (2001)
Tank	90 × 90 × 2.5 102 × 102 × 5 252 × 127 × 9	Sands and gravels: d = 0.078-3.7	Soil heterogeneity, flow pattern	0.2-2.4	#	Peterson and Murray (2003)
Tank	95 × 48 × 10 218 × 64 × 10	Quartz-sand: d = 0.84-1.68 / 0.42-0.59 / 0.17-0.29	Flow patterns, air barrier	7.2-66.7	#	Dror et al. (2004)
Tank	50 × 50 × 1	Quartz-sand: d = 0.2-2	Geometry of gas distribution	0.6-5	#	Selker et al. (2006)
Tank	45 × 50 × 1.2	Glass beads: d = 0.25-0.5 / 0.75-1.0 / 2.0-2.2	Flow patterns	0.01-3	#	Geistlinger et al. (2006)

The conceptual model of gas flow patterns through the homogeneous porous media is shown in Fig. 1.1, which is developed by Clayton (1998) for air sparging. In this model the channelized flow implies the discrete widely spaced channels that bypassed some part of the flow region. In contrast, continuum flow involves uniform distribution of smooth variation of gas saturation, without significant bypassed area. This conceptual model can be used to develop hypotheses of multi-phase flow modeling.
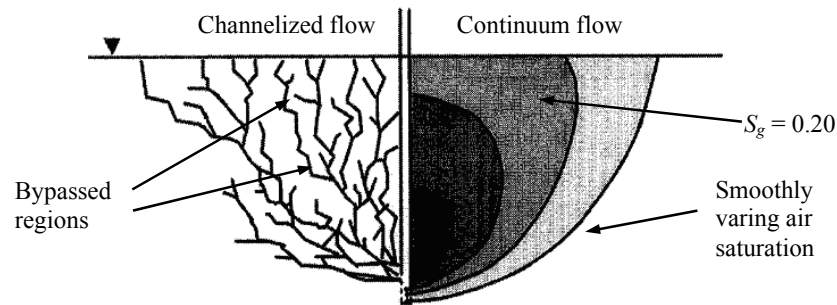
Fig. 1.1: Two possible conceptual flow patterns developed during air sparging (Clayton, 1998).

Brooks et al. (1999) categorized the gas flow pattern into four classes: channelized flow, bubbly flow, slug flow, and mixed flow. The flow is considered as channelized flow when the pores along a channel remain significantly unsaturated during the injection. Whereas, the bubbly flow and slug flow are characterized by moving bubbles and slugs, respectively, and some pores resaturated after desaturation process. Brooks et al. (1999) characterized the mixed flow as a combination of channelized flow with either bubbly flow or slug flow.

The gas flow pattern can be classified more accurately by using the physical concept of continuous phases. The channelized flow is the only coherent flow pattern, in which the gas flow through the undulating channels can be characterized as a continuous phase. The bubbly flow and slug flow are incoherent flow, because they are characterized by discrete discontinuous bubbles and slugs. Physically, the channelized flow is driven by the pressure difference along the coherent channels, while, incoherent flow is driven by the interplay of trapping and upward-moving discontinuous bubbles or clusters.

Two main flow patterns (i.e., channelized and bubbly flow) are schematically shown in Fig. 1.2. Both Fig. 1.2b and Fig. 1.2c show the channelized flow, but, the dense channel network is established in Fig. 1.2c due to the high injection flow rate. Beside that, different terms have been used in the literature to identify these two main flow patterns, but in this work the terms coherent (i.e., continuous flow) and incoherent (i.e., discontinuous flow) are used for channelized and bubbly flow, respectively.

To combine the models proposed by Clayton (1998) and Brooks et al. (1999), variation of gas saturation throughout the gas flow region can be considered. For example, the flow can be considered the continuum flow if the gas injection creates a dense channel network, in which the gas uniformly distributes throughout the affected area.
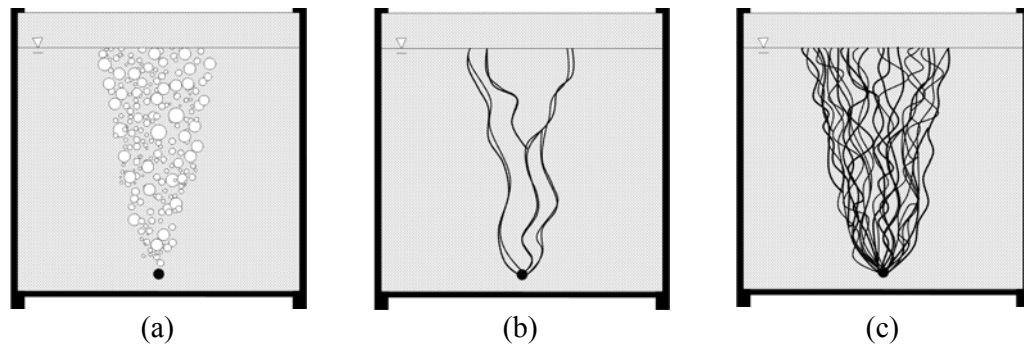
Fig. 1.2: Illustration of gas flow patterns in: (a) bubbly flow, (b) channelized flow, (c) channelized flow with dense channel network (Ji et al., 1993).

The flow patterns observed in the experiments of Table 1.1 are illustrated in Fig. 1.3. In each set of experiments in Fig. 1.3, filled-black symbols represent the coherent flow, while the others represent the incoherent flow pattern. In this figure, the area colored in yellow specifies the transition flow pattern, where both flow patterns can be occurred within one type of sediment or glass beads depending on the injection rate.
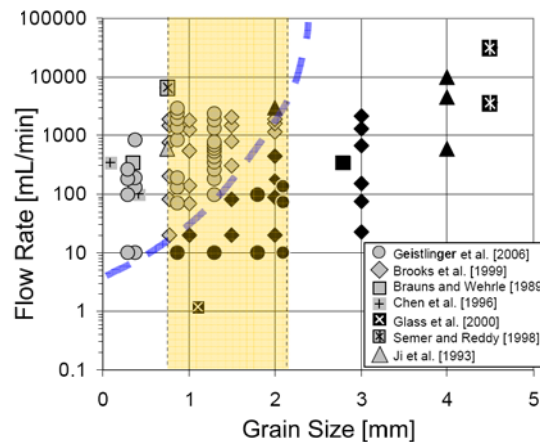
Fig. 1.3: Gas flow patterns observed in the experiments listed in Table 1.1. Filled-black symbols represent the coherent flow pattern (Krauss, 2007).

Many authors reported that the gas flow pattern in direct gas injection depends only on grain size. For instance, Ji et al. (1993) performed the series of bench-scale experiments through the saturated homogeneous glass beads, and concluded that the flow pattern depends on the grain size.

Clayton (1998) observed microscopic fingering within the fine-grained soils (e.g., silt and fine sands) that creates spatially uniform gas saturation. On the other hand, he found that widely-spaced channels commonly developed in coarse-grained soils. Clayton (1998) noticed that the gas injection through the fine-grained soils creates continuous and relatively high gas saturation. The conclusions by Clayton (1998) were confirmed later by Brooks et al. (1999) and Geistlinger et al. (2006).

Brooks et al. (1999) expressed that the flow pattern that developed through the medium sand or smaller, is channelized flow, while the flow pattern in porous media composed of coarse sand or larger, is bubbly flow. Likewise, Geistlinger et al. (2006) declared that not only the grain size, but also the injection rate influences the gas flow pattern. Geistlinger et al. (2006) particularly concluded that increasing the flow rate to a critical threshold can lead to initiate the coherent flow pattern for a certain sediment size.

To verify the statement by Geistlinger et al. (2006), a schematic flow chart derived from Fig. 1.3 is represented in Fig. 1.4, in which a neutral curve separates the coherent and incoherent flow patterns. Fig. 1.4 reveals that the flow pattern not only depends on the grain size, but also depends on the injection rate. For example, the gas injection with injection flow rate equal to $Q_g = 10$ ml/min establishes incoherent flow pattern through 1 mm same-size glass beads (1 mm-GBS). Increasing the flow rate up to 500 ml/min creates the coherent flow pattern.
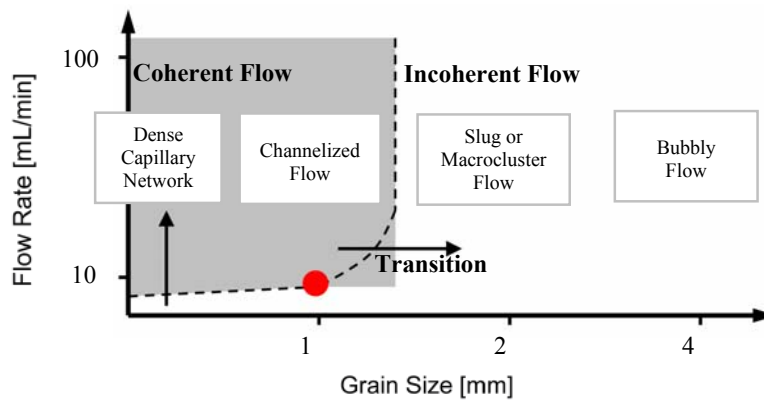
Fig. 1.4: Classification of gas flow patterns as a function of grain size and injection rate (Geistlinger et al., 2006).

However it is important to recognize and predict the gas flow pattern based on grain size and injection rates, but modeling the gas flow to predict the gas distribution for further gas injection is crucial. Comprehensive literature exists on modeling of gas transport in porous media that discussed the analytical and numerical approaches, (e.g., the review articles by McCray (2000) and Thomson and Johnson (2000)).

In most cases, the analytical solutions are derived under specific conditions and only valid in special circumstances. Because of the strong nonlinearity of multi-phase flow equations and the complexity of the flow problem, analytical models demand simplifying assumptions (e.g., steady state condition, simplified capillary pressure and relative permeability functions). To include the "real world" into the model several authors modeled the gas transport in porous media by numerical models (McCray and Falta, 1997; McCray, 2000; Thomson and Johnson, 2000; Ho and Webb, 2006). The numerical simulations provide the capacity of applying general boundary and initial conditions, heterogeneity of the porous media, and accurately represent the physical processes. Therefore, the numerical simulations can obtain the accurate estimation of injection parameters that are important to determine the injection process and design a cost-benefit injection process.

McCray (2000) reviewed the numerical models, which have been used to simulate the air sparging, and revealed that multi-phase flow models and lumped-parameter models,

which both utilize the continuum assumption, are mostly used by the authors. Although the lumped-parameter models are simpler, but multi-phase flow models offer more realistic simulation results of injection process (McCray, 2000). Further categories of numerical simulation (e.g., Lattice-Boltzmann simulation and invasion percolation approach) have been used to model the complex fluid dynamics occurring in multi-phase fluid flow through the porous media. Even though, Lattice-Boltzmann simulation can be taken only for very small domains because of large computational cost and efforts, and invasion percolation approaches are valid for pseudo-static or very slow processes (e.g., the processes undertaken only by the buoyancy forces) (Stauffer et al., 2009).

Therefore, all research papers discussed in this review are based on the continuum hypothesis that assumes the porous medium consists of overlapping fluid continua (e.g., air and water), which occupy their own pathways within the representative elementary volume (REV).

McCray and Falta (1997) used T2VOC program (a continuum model developed by Falta et al., 1995) to model the air sparging experiments conducted by Ji et al. (1993). Since there is no actual gas saturation measurement in the experiments by Ji et al. (1993), McCray and Falta (1997) undertook a quantitative comparison at the steady state. McCray and Falta (1997) emphasized the ability of T2VOC to approximate the plume size and plume shape, and the effect of heterogeneity.

Hein et al. (1997) observed that the results of modeling by T2VOC (Falta et al., 1995), underestimated the flux near the well region. Hein et al. (1997) suggested that incorrect capillary pressure function or neglecting the heterogeneity may create this level of uncertainty.

Later on, Brooks et al. (1999) declared that gas distribution at high flow rates is sufficient to apply the REV concept. But, with low flow rates, the large parts of porous medium remain unaffected where the average properties cannot describe the entire porous medium. Therefore, the continuum assumption may not be valid for low flow rate conditions (Brooks et al., 1999).

However, the continuum models have been applied, successfully, both on the bench scale and on the field scale (Unger et al., 1995; McCray and Falta, 1997; Hein et al., 1997; van Dijke and van der Zee, 1998) using homogeneous and heterogeneous permeability fields. But, several authors (e.g., Thomson and Johnson, 2000; Glass et al., 2000; Selker et al., 2007; Geistlinger et al., 2009) criticized the continuum modeling for describing the coherent channelized flow.

McCray (2000), and Thomson and Johnson (2000) reviewed the results of multi-phase flow models used, for instance, by Unger et al. (1995), Lundegard and Andersen (1996), McCray and Falta (1997), Hein et al. (1997), and van Dijke and van der Zee (1998). They concluded that continuum models can represent the bulk distribution of gas flow, but not the details of discrete gas channels. Also, McCray (2000) stated the continuum assumption is valid, if the gas channel distribution has a high density, which confirms the statement of Brooks et al (1999).

Glass et al. (2000) presented the visualization structure of gas invasion through the heterogeneous porous media. They noticed that the pore-scale properties of the gas injection process must be incorporated into the experimental observations, and therefore, they doubted about the ability of continuum model in simulating the experimental and field-site gas injection. Instead, they proposed a class of upscaled modified invasion percolation models (MIP) that is very different from the standard two-phase continuum model and requires sufficient geological details.

Selker et al. (2007) investigated the channelized flow pattern by a series of visualization experiments and confirmed the conceptual model of gas flow patterns described by Clayton (1998). The conceptual model that Clayton (1998) presented for air flow during air sparging illustrates the difference in gas saturation, lateral extent of gas flow and gas channel development within the coarse and fine sands. Clayton (1998) considered $S_g = 0.10$ as a threshold of developing the channelized flow. Fig. 1.5 shows a schematic picture of this model where a large lateral extent of airflow is developed in fine sand with $S_g > 0.10$, while in coarse sand the region with $S_g > 0.10$ is developed only near the injection point.

Selker et al. (2007) proposed that gas flow at the near-source region is governed by the continuum assumption, because most of the equiprobable channels are occupied by the injected gas. While in far-source region, the gas flows in discrete channels and leaves some portion of porous medium saturated by the liquid. Selker et al. (2007) stated that distribution of gas channels in far-source region contradicted to the continuity assumption of continuum models. Based on Selker's stochastic hypothesis, it can be anticipated that the injection can be simulated by continuum models when most of the possible gas channels are occupied by the gas (i.e., at high flow rate gas injection).
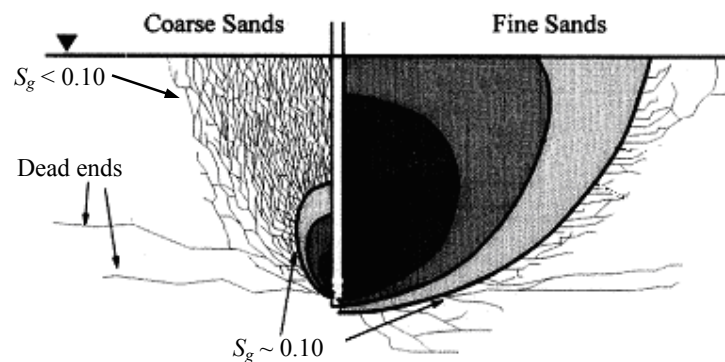
Fig. 1.5: Conceptual model for air flow during air sparging (Clayton, 1998).

After Selker et al. (2007), Geistlinger et al. (2009) conducted gas injection through a two-dimensional (2D) bench-scale experiment, and used TOUGH2 program (Pruess, 1991) to simulate the experimental gas injection. Geistlinger et al. (2009) achieved good agreement in integral properties of the experimental and simulation results (e.g., the gas volume inside the model). These results confirmed the conclusion by McCray (2000) that emphasized the ability of continuum model in simulating the integral properties.

Geistlinger et al. (2009) argued the sharp transition of gas saturation in experimental results is caused by the stochastic distribution of gas channels, while the widely, smooth Gaussian-like gas distribution in simulation results is created by the continuum assumptions. They noticed that the continuum models are developed based on the REV concept, which is in contradiction to the real stochastic distribution of gas flow that realizes a narrow range of capillaries within the porous media. Therefore, they verified the argument by Thomson and Johnson (2000), which criticized the continuum models in producing a continuous range of air saturations within the sparging zone. However the majority of analytical and numerical investigations study the gas flow pattern in

homogeneous or layered-homogeneous models, but few of them concentrate on applying the "real world" heterogeneity into multi-phase continuum modeling. To the author knowledge, there are no numerical multi-phase studies of gas flow pattern at field scale. At bench-scale, Stauffer et al. (2009) used classical continuum approach to simulate the gas flow pattern developed through a 2D gas injection experiments. They argued that applying heterogeneity when grid blocks are smaller than the corresponding REV, can scale the pore-scale properties in continuum modeling. Stauffer et al. (2009) called it sub-scale simulation. They concluded that if the sub-scale heterogeneity is applied, the continuum model could describe the channelized gas flow. They also argued that heterogeneity in capillary pressure has the main influence of the channelized flow pattern, compared with the heterogeneous permeability and porosity fields. Since Clayton (1998) and Stauffer et al. (2009) emphasized the necessity of special consideration in continuum modeling (i.e., applying the stochastic properties in simulation), it is decided to study the continuum modeling and investigate the effect of stochastic heterogeneity on simulation results. The stochastic heterogeneity is applied in continuum modeling at REV-scale. Furthermore, the sub-scale heterogeneity, which is proposed by Stauffer et al. (2009), is investigated.

Stauffer et al. (2009) compared the visualization results of gas distribution, but, they never compared the quantitative values of gas saturation or gas volume. For instance, Fig. 1.6a and Fig. 1.6b show image of gas distribution in 2D experiment and sub-scale simulations, respectively, for Q_g = 82 ml/min at t = 1.8 s. The simulation results in Fig. 1.6b show gas saturation through six different realizations of pore radii. In addition, investigation of simulation results by Stauffer et al. (2009) reveals that applying the sub-scale heterogeneity cannot guarantee obtaining the gas flow pattern with same specification of experimental results.

(a)   (b)
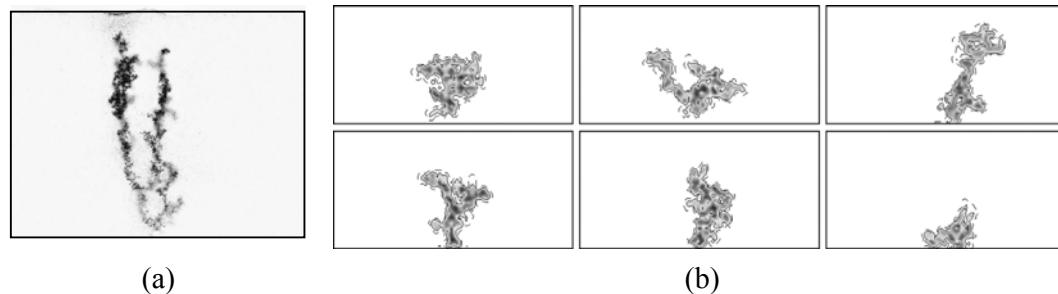
Fig. 1.6: Gas distribution in: (a) experimental image, and (b) subscale simulation by using six different realizations of pore radii. All images are provided with injection rate of Q_g = 82 ml/min at t = 1.8 s (Stauffer et al., 2009).

Summarizing the controversial discussion is best expressed by the two key papers:
1. Glass et al. (2000) doubted the ability of continuum model in simulating the channelized flow pattern in heterogeneous porous media and emphasized that only discrete models (e.g., MIP model or pore network modeling) could simulate the channelized flow pattern.
2. Stauffer et al. (2009) argued that using the sub-scale heterogeneity in continuum models is able to describe the main characteristics of the channelized gas flow.

This dissertation aims to give an answer to this controversy and will derive conditions at which continuum modeling can be successfully applied.

1.3   Objectives and structure of the work

The classification of gas flow pattern has been completed by many authors (Ji et al., 1993; Chen et al., 1996, Semer et al. 1998; Brooks et al., 1999; Peterson et al., 1999; Glass et al. 2000; Peterson et al., 2001; Reddy and Adam 2001; Lazik et al., 2002, Geistlinger et al. 2006). The particular interest of this study devotes on investigation and simulation of channelized flow pattern by continuum model. The main objectives of this dissertation are summarized as follows:

1. Developing the conceptual model of gas-water system that conceives the physical principles of gas flow through the porous medium at the pore-scale. The conceptual model should concern the main gas flow patterns and investigate the stability criteria, in which these flow patterns would develop under. To develop the simulation model, the conceptual model should obtain the specification (e.g., pore size distribution) of porous media.

2. Investigation of two main flow patterns (i.e., bubbly incoherent flow and channelized coherent flow) developed within the GBS in bench-scale experiments performed by Krauss (2007). Beside the investigation of gas flow pattern in experiments, the geometric shape of gas plumes obtained by continuum models investigate. The TOUGH2 program (Pruess, 1999) is used in this work. Therefore, the most part of this study will be devoted to examine the prediction ability of continuum model in simulating the direct gas injection in 2D and 3D. It is critical to investigate whether the continuum model could imply the effect of pore properties, since the continuum models use the average properties.

3. Applying the stochastic heterogeneity in continuum modeling. The most important goal of this work is to examine the prediction ability of TOUGH2 program (Pruess, 1999) in simulating the channelized coherent gas flow pattern. The existing literature inferred that the continuum model is able to characterize the averages properties of flow pattern (e.g., the shape of gas plume, and the averages gas saturation). But, recently, it is in dispute that the continuum model could represent the details of gas channels in channelized flow. Therefore, the qualitative and quantitative measurements performed by Krauss (2007) in bench-scale experiments are used to test the continuum model. First, the stochastic heterogeneity is applied in numerical simulation, and then, the simulation results are compared to the experimental data to justify the capability of continuum model to characterize the gas distribution.

4. Investigation the effect of heterogeneity (i.e., correlated and uncorrelated heterogeneity) on simulation results of continuum models. As the porous media is heterogeneous, it is critical to apply the appropriate heterogeneity in simulation model that can represent the specification of flow properties occurred in reality. Different heterogeneity is applied in simulation of gas injection in bench-scale experiments. Comparing the simulation results with the experimental observation could expose which stochastic field could appropriately demonstrate the real heterogeneity of a porous medium.

5. Derivation of an appropriate constitutive relationship (e.g., capillary pressure and relative permeability functions) that obtain the physical characteristics of the porous media. Generally, there is no conclusion about the accurate constitutive relationships. In soil-physics, hydrology, and petroleum engineering, different constitutive relationships are used in simulation work. Consequently, one of the objectives of this dissertation is finding out the appropriate relationship that can describe the physical aspects of gas injection in porous media.

6. Developing the 3D model to simulate the injection processes carried out in field-scale. The gas flow patterns developed in bench-scale experiments are analyzed to drive the hypotheses for gas injection in field-scale. Then, the high resolution measurements of sensor array at the test site are used to calibrate and correct the simulation model at field-scale. The field-scale 3D model can represent how the results in bench-scale can be generalized to the larger scales.

In order to cover these objectives, this dissertation consists of six chapters. The comprehensive literature review of direct gas injection and numerical modeling of gas flow were discussed in this chapter. The conceptual model, which involves the physical principles of gas flow within the porous medium, will be presented in Chapter 2. In addition, the mathematical background of different approaches for parameterization of constitutive relationships is studied in Chapter 2.
The Chapter 3 will be devoted to mathematical background of two-phase flow when gas displaces the water. It will review the mathematical formulation of immiscible two-phase flow, which is the basis of TOUGH2 program. The fourth chapter comprises an overview of bench-scale experiments performed by Krauss (2007). The observation of bench-scale experiments will be used to validate the results of stochastic simulation by TOUGH2 program. The results of stochastic simulation, which are obtained by utilizing different heterogeneity, will be summarized in Chapter 4. The observation and conclusion of Chapter 4 are used to perform an appropriate and efficient gas remediation process in Leuna test site. Development of gas injection in field site and the results of stochastic simulation of different four injection scenarios will be presented in Chapter 5. Finally, Chapter 6 concludes this study by summarizing the main results of the previous chapters, and providing the outlook for further research.

2   Conceptual Model for Direct Gas Injection into Water-saturated Porous Medium

To investigate direct gas injection into heterogeneous porous media, a conceptual model is needed, which simplifies the real multi-phase flow processes in porous media. This conceptual model should represent the flow behavior of immiscible fluids in a multi-phase flow system. This chapter focuses on developing the conceptual model for direct gas injection, and applying the mathematical relationships to develop an appropriate simulation model.

2.1   Forces acting at the pore scale

Different flow patterns can be developed in a multi-phase flow process. Thus, it is important to predict which flow pattern exists or dominates through a known porous medium. The porous medium is characterized by the pore size distribution, the connectivity of the pores and the topology of the pores.

The focus of this work is on the pore size distribution (i.e., on characterization of pore bodies and pore throats). For example, the movement of a gas bubble through a porous medium depends on the interaction of three different forces: buoyancy force, capillary force, and viscous force. Capillary force associates with the pore throats that resist the upward movement of gas bubbles. The competition between buoyancy force and capillary force defines the mobility criterion, which indicates if a trapped gas bubble can move upward. If the buoyancy force overcomes the capillary forces within the pore throats, gas moves upward. Otherwise, the gas is trapped into the pore body until an additional force is provided, for example by a gas channel that is connected to the injection source (Brooks et al., 1999).

The wetting behavior is a key characteristic of gas flow pattern. Fig. 2.1 represents the interfacial tensions (σ_{GL}) that exist between the fluid phases (while G and L represent gas and liquid phases respectively) and the solid surface (S) in static condition. The angle between the solid surface and the tangent line at the fluid-fluid interface is called the contact angle θ (see Fig. 2.1). The wettability of the fluid can be determined based on the static contact angle (Bear, 1972).

Regards to Fig. 2.1, when the $0 < \theta < 90$, the fluid L tends to wet the solid surface, and the fluid is called wetting fluid. The zero contact angle ($\theta = 0$) shows the solid surface becomes completely wet by the fluid L. Non-wetting condition occurs where $\theta > 90$ and the fluid L is called non-wetting fluid. In this work, gas is the non-wetting fluid and water is the wetting fluid.
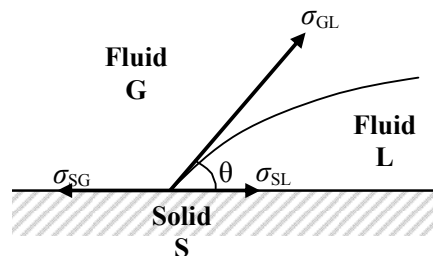
Fig. 2.1: Illustration of interfacial tensions between solid surface, fluids L and fluid G.

2.1.1 Capillary, buoyancy, and viscous forces

As it was stated in section 1.2, the two main flow patterns are channelized flow and bubbly flow. Therefore, the forces acting only on a trapped gas bubble (e.g., in bubbly flow), and on a gas channel (e.g., in channelized flow) are elucidated in this section. When two immiscible fluids (e.g., gas and water) are in contact, a discontinuity in pressure exists across the interface that separates these two fluids. The classical definition of the capillary pressure, P_c, is given by the pressure difference across the interface when the interface is in equilibrium:

$$P_c = P_{nwet} - P_{wet}$$ (2.1)

where,
P_{nwet} = pressure of the non-wetting fluid, [M L^{-1} T^{-2}]
P_{wet} = pressure of the wetting fluid, [M L^{-1} T^{-2}]

The interface has a curvature that represents the magnitude of the pressure difference. The interface between two immiscible fluids (e.g., Fluid L and fluid G) has two principal radii of curvature, r_1 and r_2 (Fig. 2.2). In this figure, red and blue vectors are the force components resulting from the interfacial tension that acts on the curved interface in principal directions. The vector F_C is the resultant capillary force (sum of the red and blue vectors) exerted on the interface area ΔA_{LG}, between these two fluids. The relationship between force per area (i.e., pressure) and the principal curvatures is given by the Laplace-Young equation:

$$P_c = \frac{F_C}{\Delta A_{LG}} = \sigma_{wet.nwet} \left(\frac{1}{r_1} + \frac{1}{r_2} \right)$$ (2.2)

where,
$\sigma_{wet,nwet}$ = Interfacial tension of wetting and non-wetting fluids, [M T^{-2}]
r_1 and r_2 = principal radii of curvature (Fig. 2.2), [L]
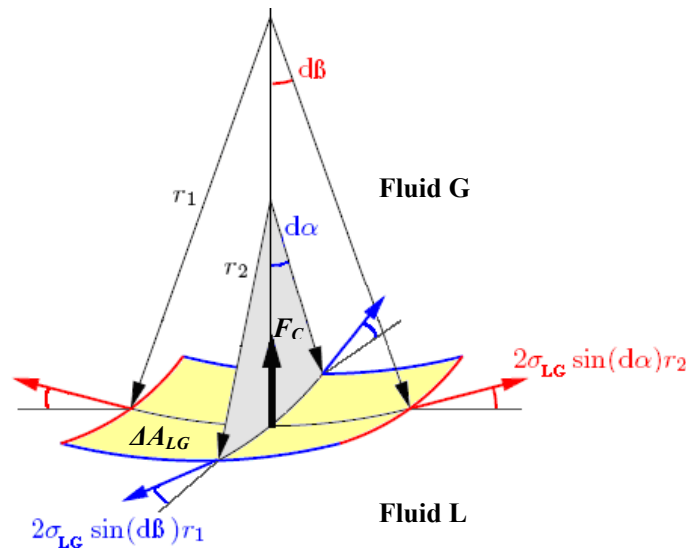
Fig. 2.2: Illustration of the forces acting at a small section of a curved interface between two immiscible fluids.

Based on the Laplace-Young equation, the capillary pressure depends on the geometry of void space (pore size distribution), the nature of solid and liquid phases (interfacial tension) and the saturation value (Bear, 1972).

The principal radii of a trapped gas bubble, and a cylindrical gas channel are equal to $r_1 = r_2 = r$ and $r_1 = \infty$, $r_2 = r$, respectively. Thus, the capillary pressure of a trapped gas bubble with radius r becomes:

$$P_{c,bubble} = \frac{2\sigma_{wet,nwet}}{r} \tag{2.3}$$

While, the capillary pressure in a gas channel that has the radius r is equal to:

$$P_{c,channel} = \frac{\sigma_{wet,nwet}}{r} \tag{2.4}$$

Therefore, the capillary pressure within a gas bubble is two times larger than the capillary pressure acts within a cylindrical gas channel, when both have the same radii. The capillary forces acting on a trapped gas bubble and a stable gas channel are presented in Fig. 2.3a and Fig. 2.3b.

Trapped gas bubble

The phase boundary of a gas bubble has the minimum state of energy for the gas phase. In other words, an irregular gas volume (e.g., the gas aggregate) cannot be maintained in equilibrium state because of inhomogeneous pressure distribution (Dullien, 1992).

Fig. 2.3a represents a trapped gas bubble within a porous medium. In this work, it is assumed that the solid surface becomes totally wet by the water phase ($\theta = 0$).
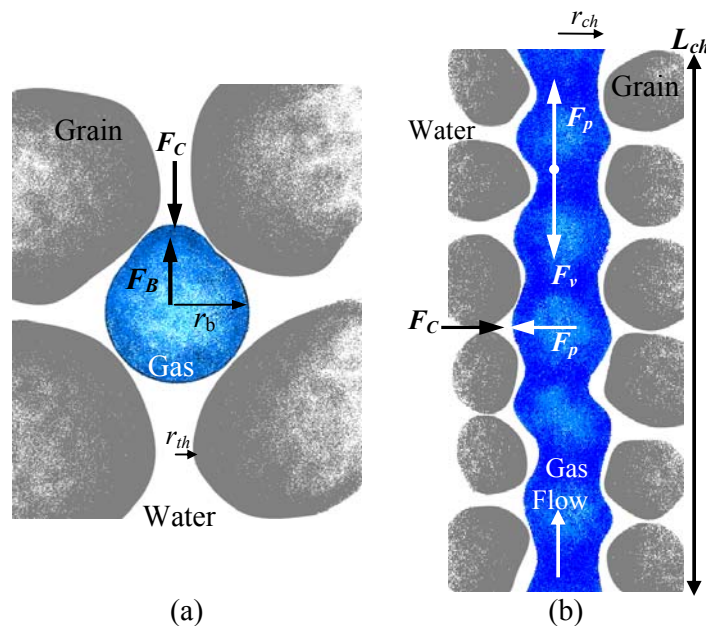
Fig. 2.3: Relevant forces in a three-phase system for: (a) a trapped gas bubble, (b) a stable gas channel.

Since the maximum capillary pressure is determined by the pore throat radius and the interfacial tension, the capillary force (F_C) acting on a gas bubble is equal to:

$$F_C = 2\pi\, r_{th}\, \sigma_{w,g} \tag{2.5}$$

where,
$\sigma_{w,g}$ = interfacial tension between water and gas phases, [M T^{-2}]
r_{th} = radius of pore throat, [L]

On the other hand, the buoyancy force (F_B) for a spherical gas bubble with radius r_b is:

$$F_B = V_{bubble}\, \Delta\rho\, g = \frac{4}{3}\pi\, r_b^3\, \Delta\rho\, g \tag{2.6}$$

where,
r_b = radius of spherical gas bubble, [L]
$\Delta\rho$ = density difference between water and gas phases, [M L^{-3}]
g = gravitational acceleration, [L T^{-2}]

The capillary and buoyancy forces acting on a gas bubble are shown in Fig. 2.3a. While the trapped bubble has not moved, no viscous force appears. When the gas bubble starts moving, the viscous force acts against the gas bubble movement. A pack of equal-sized glass beads is considered in this chapter to estimate the strength of the forces acting on a gas bubble (see bench-scale experiments in Chapter 3). The values of minimum and maximum pore radii through a pack of 0.5 mm glass beads (0.5 mm-GBS) are estimated about 0.11 mm and 0.23 mm, respectively (see Table 2.2). For $\Delta\rho_{w,g}$ = 997 kg/m^3 and $\sigma_{w,g}$ = 71.98 dyn/cm at 20°C, the F_c and F_B become equal to 2.49×10^{-5} N and 6.23×10^{-8} N. The value of capillary force is much higher than the buoyancy force. Consequently, a trapped gas bubble within the 0.5 mm-GBS cannot move upward, unless by connecting to the gas injection source (e.g., by a gas channel), or by upward flow of water phase (Brooks et al. 1999).

Stable gas channel
The forces acting within a gas channel are pressure force, viscous force, and the capillary force (Fig. 2.3b). The flow through a gas channel can be simplified as flow within a uniform capillary (capillary tube) with the radius of r_{ch}. It is assumed that the Hagen-Poiseuille law is valid for the gas flow through the gas channel. Hence, the pressure difference along the gas channel of length (L_{ch}) is:

$$\Delta P_g = \frac{8\, \mu_g\, Q_g\, L_{ch}}{\pi\, r_{ch}^4} \tag{2.7}$$

where,
P_g = gas pressure, [M L^{-1} T^{-2}]
μ_g = dynamic viscosity of gas phase, [M L^{-1} T^{-1}]
Q_g = gas injection flow rate, [L^{3}T^{-1}]
L_{ch} = length of gas channel, [L]
r_{ch} = radius of gas channel, [L]

Thus, the flow-driving pressure force (F_P) becomes:

$$F_P = \Delta P_g \, \pi \, r_{ch}^2 = \frac{8 \, \mu_g \, Q_g \, L_{ch}}{r_{ch}^2} \tag{2.8}$$

The pressure force has to overcome the flow-resisting viscous force (F_v), which is presented in Eq. (2.9).

$$F_v = 8\pi \, \mu_g \, v_g L_{ch} = \frac{8 \, \mu_g \, Q_g \, L_{ch}}{r_{ch}^2} \tag{2.9}$$

The viscous force is determined by the shear stress acting at the interface of the gas channel (i.e., $2\pi \, r_{ch} L_{ch}$). The shear stress of a laminar flow through the gas channel is equal to:

$$\tau_s = 4\mu_g \frac{v_g}{r_{ch}}$$

where,
τ_s = shear stress, [M L^{-1} T^{-1}]
v_g = average flow velocity, [M T^{-1}]

For steady-state gas flow, the pressure force has to overcome the viscous force (i.e., $F_P \geq F_v$ in Fig. 2.3b).
In addition, mechanical equilibrium must hold for a stable gas channel in steady-state condition. Thus, the pressure forces must balance the capillary force, otherwise, the gas channel would be snapped off. The capillary force acting along the gas-water interface of a stable gas channel is illustrated in Fig. 2.3b. According to the Laplace-Young equation the magnitude of capillary force is:

$$F_C = \pi \, r_{ch} \, \sigma_{w,g} \tag{2.10}$$

The viscosity of air is about 1.9×10^{-5} Pa.s at 20°C. According to Eq. (2.8), with the gas injection rate of Q_g = 10 ml/min in 0.5 mm-GBS, the flow-driving pressure force is about 3.35×10^{-3} N for a gas channel length of 35 cm. On the other hand, according to Eq. (2.10), the maximum capillary force acting on the gas-water interface is 1.25×10^{-5} N. The pressure force can create stabilized gas channels, since the capillary force is negligible respect to the pressure force.

2.1.2 Competition between capillary, buoyancy, and viscous forces

Bond number

The competition between buoyancy force and capillary force can be quantified by a dimensionless number called Bond number (N_B). The Bond number has been used by many authors to characterize the multi-phase flow in a porous medium (e.g., by Morrow and Songkran, 1981; Pennell et al., 1996). Morrow and Songkran (1981) assumed zero contact angle, and defined the Bond number as the ratio of buoyancy force (Eq. (2.6)) and capillary force (Eq. (2.5)):

$$N_B = \frac{4\pi r_b^3 \, \Delta\rho \, g}{3} \frac{1}{2\pi r_{th} \, \sigma_{w,g}} = \frac{2}{3} \frac{\Delta\rho \, g \, r_b^2}{\sigma_{w,g}} \frac{r_b}{r_{th}} \approx \frac{\Delta\rho \, g \, r_b^2}{\sigma_{w,g}} \tag{2.11}$$

Eq. (2.11) is based on the assumption that the aspect ratio (i.e., $\alpha = r_{th}/r_b$) and pre-factor are equal to one (see the last equality in Eq. (2.11)).

N_B is greater than unity when buoyancy force is dominant. While, for a process with dominant capillary force, N_B becomes less than unity.

In order to take the physical aspect ratio into account (Eq. (2.11)), Brooks et al. (1999) introduced a modified Bond number, N_B^*:

$$N_B^* = \frac{N_B}{\alpha} = \frac{\Delta\rho \, g \, r^2}{\sigma \, \alpha} \tag{2.12}$$

For example, the Bond number and the modified Bond number are approximately 0.034 and 0.07, respectively, for vertical air flow through the 0.5 mm-GBS (aspect ratio is about 0.5, see Table 2.2). The value of 0.07 shows that the capillary forces are dominant and the gas bubble remains trapped within the 0.5 mm-GBS.

Brooks et al. (1999) conducted gas injection experiments through six different glass beads (0.42-0.50, 0.71-0.80, 1, 1.5, 2, 3 mm-GBS). They plotted the modified Bond numbers versus the grain size, and used this plot for classifying the experimental flow patterns. Fig. 2.4 shows that Brooks et al. (1999) classified the coherent channelized flow for modified Bond numbers less than unity. The flow pattern changes to incoherent bubbly flow, if the modified Bond number becomes greater than one. Therefore, they concluded that the flow pattern would change when capillary and buoyancy forces reverse their dominance. The grey symbols in Fig. 2.4 indicate the gas flow patterns that Geistlinger et al. (2006) observed in their experiments through 0.5 mm-, 1 mm- and 2 mm-GBS. Geistlinger et al. (2006) observed coherent and incoherent flow through 0.5 mm- and 2 mm-GBS, respectively. While, the flow pattern through 1 mm-GBS is changed from incoherent to coherent flow by increasing the injection rate. Therefore, modified Bond number can be used to predict the flow pattern. However, it is not a strict classification. For example, they observed bubbly flow for 2 mm-GBS, while transition flow pattern is predicted respect to the graph by Brooks et al. (1999) for 2 mm-GBS pack. Using a single aspect ratio to characterize the bead size and also using the simplified Bond number to characterize the competition between buoyancy and capillary forces, gives an inaccurate transition zone. It means that the viscous forces cannot be neglected in order to describe the complicated process of multi-phase flow in complex porous media.
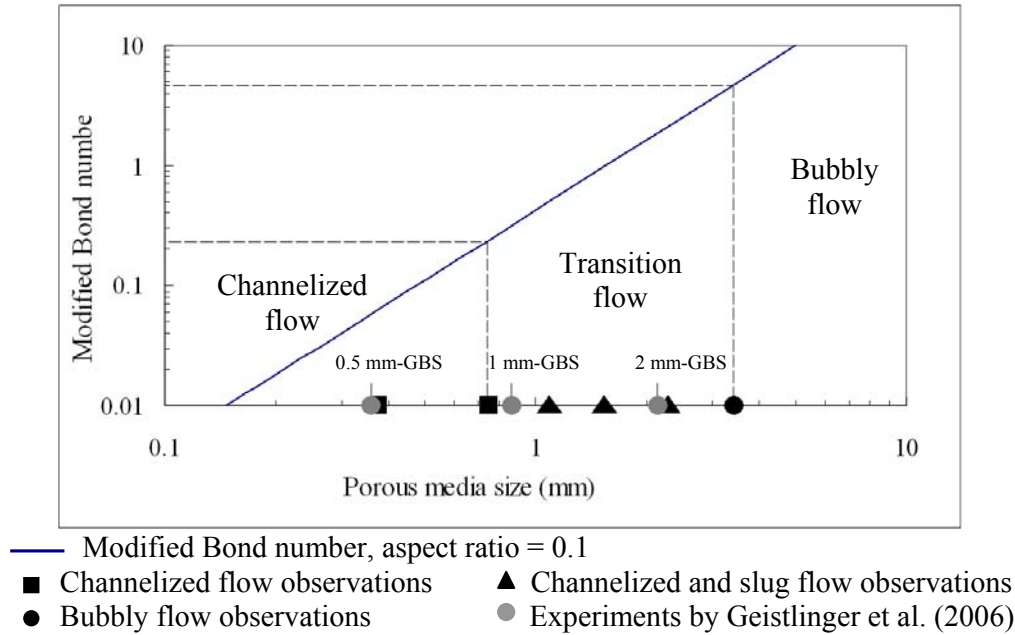
Fig. 2.4: Characterization of gas flow pattern by using modified Bond number (Brooks et al., 1999)

Capillary number

The competition between viscous forces and capillary force can be quantified by a dimensionless number called Capillary number (N_C). Using the viscous force in Eq. (2.9) and the capillary force in Eq. (2.5), one can obtain the Capillary number according to Dullien (1992, Eq. (5.383)):

$$N_C = \frac{8\mu_g\, Q_g\, L_{ch}}{r_{ch}^2} \frac{1}{2\pi\, r_{th}\, \sigma_{w,g}} = \frac{4L_{ch}}{r_{ch}} \frac{\mu_g\, Q_g}{\pi\, r_{ch}^2\, \sigma_{w,g}} = \frac{4L_{ch}}{r_{ch}} N_{C,classic} \tag{2.13}$$

where, $N_{C,classic}$ is the classical Capillary number. Dullien (1992) criticized that the classical Capillary number is not sufficient to specify the dynamic conditions of flow through porous media. He stated that the classical Capillary number obtains small values, because of incorrect unphysical definition.

The values of classical Capillary number for 0.5mm-, 1mm- and 2mm-GBS are equal to 1.9×10^{-3}, 3.1×10^{-4} and 6.0×10^{-5}, where the gas injected with $Q_g = 10$ ml/min and the mean radii of gas channel are 0.085, 0.21 and 0.48 mm, respectively (see Table 2.2). The main drawback of the classical Capillary number in all cases is that the viscous forces are negligible (i.e., by five orders of magnitude smaller than capillary forces). But, Dullien stated that the simple criterion $N_{C,classic} < 1$ has not the physical meaning that capillary forces are larger than viscous forces.

By using Dullien's definition in Eq. (2.13) and applying the length scale of gas channels in bench-scale experiments ($L_{ch} \sim 0.35$ m), the Capillary numbers become equal to 31.92, 2.11 and 0.17 for 0.5mm-, 1mm- and 2mm-GBS, respectively. It means that the viscous forces dominate the capillary forces in 0.5mm-GBS. While one

anticipated that viscous forces have the same order of magnitude as capillary forces in 1mm-GBS, and capillary forces dominate the viscous forces in 2mm-GBS. These results reflect the experimental observations by Geistlinger et al. (2006), in which for instance, the channelized flow pattern was established within 0.5 mm-GBS.

Therefore, any parameter that represents the competition between viscous and capillary forces has to be corrected by the pre-factor of $4L_{ch}/r_{ch}$.

Lenormand and Zarcone (1988) proposed a phase-diagram that divides two-phase immiscible displacement processes into three dominant flow regimes: stable displacement, viscous fingering, and capillary fingering. According to Lenormand and Zarcone (1988), capillary fingering implies that the injected phase flows throughout the path that has least capillary resistance, while in viscous fingering the injected phase flows primarily by the viscous forces.

In this phase-diagram, the displacement processes are characterized by two dimensionless numbers: the viscosity ratio and the classical capillary number. Since the Capillary number is modified in Eq. (2.13), therefore the phase-diagram of Lenormand and Zarcone (1988) should be scaled by the pre-factor, which is about 10^4 for gas injection within three different GBS (i.e., 0.5 mm-, 1 mm- and 2-mm GBS). Fig. 2.5 represents the scaled phase-diagram of Lenormand and Zarcone (1988), in which the viscosity ratio (M) is defined in Eq. (2.14) when phase 2 displaces phase 1.

$$M = \frac{\mu_2}{\mu_1} \tag{2.14}$$
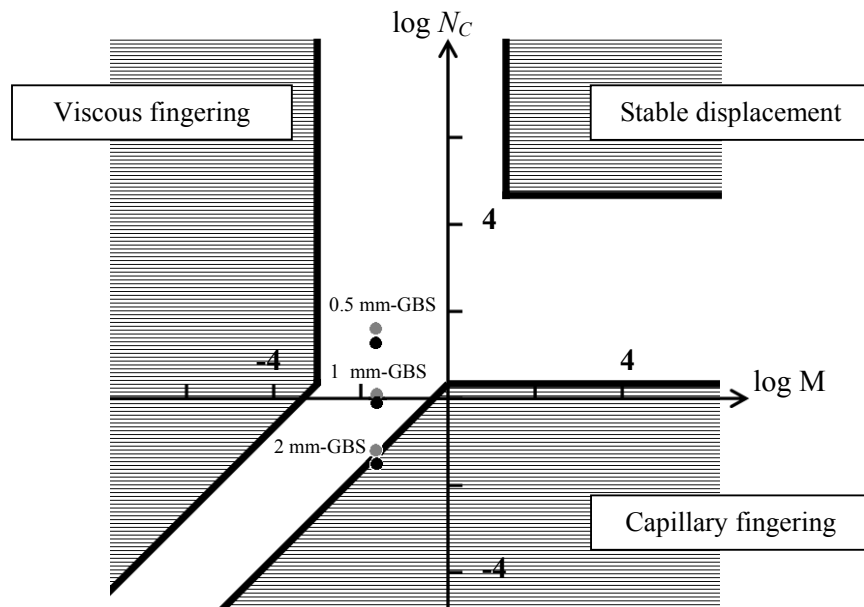
Fig. 2.5: Modified phase-diagram for two-phase immiscible displacement (originally by Lenormand and Zarcone, 1988).

In this work, the displacing fluid is gas and displaced fluid is water. Hence, the viscosity ratio is about 0.01. The logarithm of capillary numbers for 0.5 mm, 1 mm- and 2 mm-GBS when injection rate Q_g = 10 ml/min passes through one channel, are equal to 1.5, 0.32, and -0.76, respectively. Since the logarithm of M is equal to -1.73, the capillary numbers of 2 mm-GBS lays in capillary fingering region, while the capillary number of 0.5 mm- and 1 mm-GBS lay in transition region. These results are shown with gray symbols in Fig. 2.5.

If it is assumed that the gas injection Q_g = 10 ml/min creates three channels, the corresponding capillary numbers become equal to 1.03, -0.15, and -1.23 for 0.5 mm, 1 mm- and 2 mm-GBS, which are shown in Fig. 2.5 by black symbols. The estimations with three gas channels predict the same displacement processes.

The gas injection in 2 mm-GBS is bubbly flow, which is highly affected by capillary forces, and the gas injection in 1 mm-GBS is in transition between channelized and bubbly flow. Therefore, the estimations for 1 mm- and 2 mm-GBS are consistent with the experimental observations by Geistlinger et al. (2006). But, the prediction for 0.5 mm-GBS is not consistent with their experimental results in which the flow was channelized and highly affected by viscous forces. It means that the phase-diagram in Fig. 2.5 is not able to predict all the displacement process. The most shortage of this phase-diagram is that the destabilizing buoyancy forces, which affect the vertical gas flow, are not considered.

In conclusion, the investigation by using the dimensionless numbers reveals that they have high degree of uncertainty. In other words, estimations based on these two dimensionless numbers (i.e., Bond number and Capillary number) are insufficient to describe the complex multi-phase flow process through the porous media. Consequently, without numerical models, which map the essential dynamics and physics of the multi-phase flow process, the prognoses of flow pattern are rather speculative.

2.2   Gas flow pattern and stability criteria

2.2.1   Incoherent flow

The competition between buoyancy and capillary forces determines whether the trapped gas bubbles start to move, or not. The incoherent flow occurs when buoyancy forces are larger than capillary forces such that the gas could rise upward in discrete bubbles or clusters (Brooks et al. 1999). When the capillary forces at the pore throats are large enough and prevent the upward advancement of bubbles, the gas is trapped in pores. In conclusion, any parameter that affects the pore size distribution of the porous medium could change the gas flow pattern. Brooks et al. (1999) considered the grain-size distribution, grain angularity and packing configuration as the determining parameters.

In isotropic homogenous porous media, the incoherent flow develops symmetrically around the injection point (Ji et al., 1993; Peterson, 1999; Selker et al., 2007; Geistlinger et al., 2009). Peterson et al. (1999) argued that the volume invaded by incoherent gas flow has certain lateral boundaries. The incoherent gas flow is illustrated in Fig. 2.6.
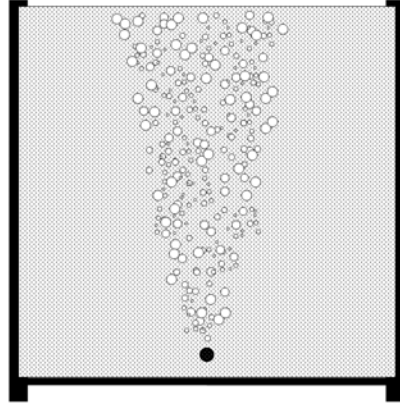
Fig. 2.6: Illustration of incoherent flow pattern (Ji et al., 1993).

The mobility criterion is important to find out when the trapped gas bubbles becomes mobile and moves upward. If the buoyancy force balances the trapping capillary forces, the gas bubble starts to move upward. By using Eqs. (2.5) and (2.6), one obtains:

$$2\pi r_{th}\,\sigma_{w,g} = \frac{4}{3}\pi r_b^3\,\Delta\rho\,g \tag{2.15}$$

By defining the aspect ratio the critical value of grain radius, in which the incoherent flow may occur, is equal to:

$$d_{k,critical} = \sqrt{\frac{6\sigma_{w,g}\,\alpha}{\zeta_{max}^2\Delta\rho\,g}} \tag{2.16}$$

where,
$d_{k,critical}$ = critical grain diameter to establish the incoherent flow, [L]
ζ_{max} = maximum dimensionless diameter in units of d_k, [-]
d_k = diameter of glass beads (or grains), [L]

Based on the mobility criterion (Eq. (2.16)), one can estimate the critical grain size, $d_{k,critical}$, of about 7 mm (ζ_{max} = 0.6 and α = 0.4, see the Eqs. (2.27a) and (2.27b)). It means that for sediments with grain sizes larger than 7 mm, buoyancy forces overcome the capillary forces and incoherent bubbly flow occurs. Ji et al. (1993), Brooks et al. (1999), and Geistlinger et al. (2006) observed the incoherent flow through the glass bead pack with d_k equals to 4 mm, 3mm, and 2 mm, respectively. Hence, Eq. (2.16) gives too larger, unphysical values for the critical grain diameter. The estimated values of $d_{k,critical}$ are not consistent with the experimental observations, because the viscous forces are neglected. In other words, the static mobility criterion cannot explain the experimental incoherent bubbly flow.
Another important parameter of incoherent bubbly flow is the length scale of moving bubbles or clusters. Fig. 2.7 shows a gas cluster that tends to move upward.
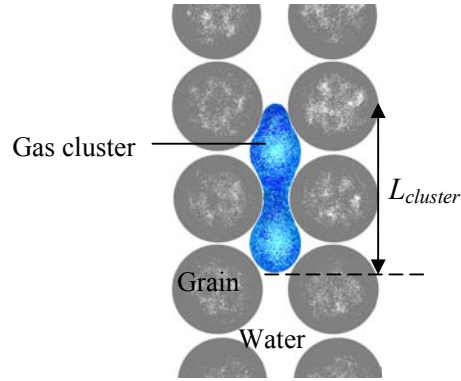
Fig. 2.7: Movement of a gas cluster with length L.

The gas cluster should overcome the capillary pressure acting at the front, and moves upward. Since the gas pressure within the cluster is constant, then the length of the gas cluster can be obtained by considering the difference in water pressure along the cluster:

$$L_{cluster} = \frac{P_{c,max} - P_{c,min}}{\rho_w g} = \frac{2\sigma_{w,nw}}{\rho_w g}\left(\frac{1}{r_{th}} - \frac{1}{r_b}\right)$$

(2.17)

where,

$L_{cluster}$ = length of isolated gas cluster, [L]

ρ_w = density of water, [ML^{-3}]

Eq. (2.17) shows that the length of a gas cluster depends on the sizes of pore throat and pore body that exist in a porous medium. Chatzis et al. (1983) investigated the cluster size of residual oil through the pack of spherical sediments. They observed that the large clusters (e.g., 10 times larger than the size of spheres) were not stable and divided into smaller units and mobilized. But, the gas bubbles in incoherent flow have higher mobility, because of smaller viscosity and density compared to the residual oil clusters. Thus, the instability of large clusters results in gas clusters with smaller extent. By using Eq. (2.17), the length of gas cluster is equal to 2.5 cm within 2 mm-GBS ($d_{min} = 0.6$ mm, and $d_{max} = 1.3$ mm, see Table 2.2). On the other hand, Geistlinger et al. (2006) used the average values of measured $P_{c,max}$ and $P_{c,min}$, and obtained the cluster length of 1.3 cm through 2 mm-GBS. The cluster size calculated by Eq. (2.17) is higher than the experimental value by Geistlinger et al. (2006), but they have the same order of magnitude.

2.2.2 Coherent flow

The competition between viscous forces and capillary forces determines whether the injection process establishes stable gas channels. According to the discussion in section 2.1.2, if the viscous force overcomes the capillary force, the gas flow becomes channelized flow. Fig. 2.8 shows the conceptual model for channelized flow in different scales. The total gas injection rate, Q_{total}, is applied at macroscopic-scale. This total flow rate splits into different macroscopic gas channels, which can be observed by visualization experiments. The flow rate through each macro channel is denoted by Q_{ch}.

The sum of all Q_{ch} gives Q_{total}. On the pore-scale, the gas flow goes through few pores and creates micro channels (Glass et al., 2000). The flow rate within each micro channel is denoted as Q_p, where the sum of all micro channels gives Q_{ch}. Fig. 2.8a shows the gas channels of coherent flow in macroscopic-scale, in which the flow occurs through the meandering macro channels. A segment of a macro channel is shown in Fig. 2.8b. If the injection rate increased, a network with higher channel density is developed. Fig. 2.8c represents the gas flow at pore-scale, in which the gas follows through the pore bodies, where some pores are remained unaffected. The gas flow in pore-scale depends on the microscopic properties of the porous medium. On the other hand, the gas channels of macroscopic-scale can represent the average flow properties of the pore-scale.
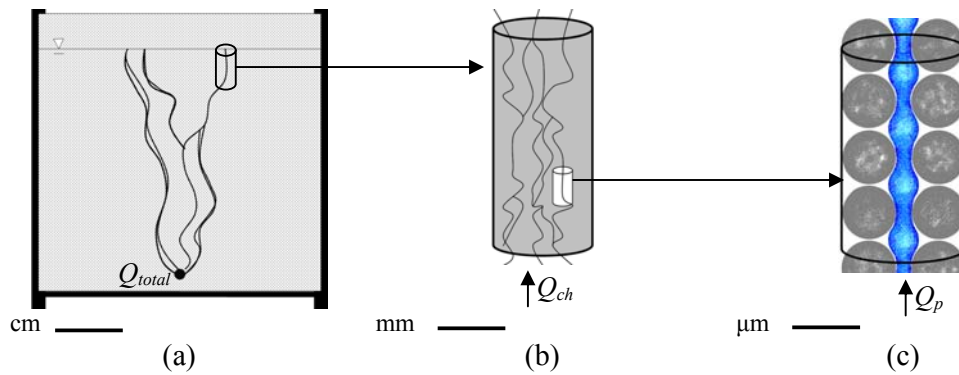
Fig. 2.8: Channelized flow on different scales (Geistlinger et al., 2006).

Fig. 2.9 represents the gas flow through an undulating gas channel that is shown in Fig. 2.8c. To conceptualize the microscopic flow, the undulating channel is approximated by a straight gas capillary with the mean radius of r_{ch}.

According to Eq. (2.7), the flow through a gas channel of length L_{ch} is described by the following equation:

$$Q_g = \frac{\pi\, r_{ch}^4\, \Delta P_g}{8\, \mu_g\, L_{ch}}$$

For a stable gas channel, the pressure gradient is equal to the hydrostatic gradient of water (i.e., $\Delta P_g / L_{ch} = \rho_w g$). Therefore, the flow within a stable gas channel has to satisfy the following condition:

$$Q_{critical} = \frac{\pi\, \rho_w g}{8 \mu_g}\, r_{ch}^4 \tag{2.18}$$

The flow rate in Eq. (2.18) is called the critical flow rate ($Q_{ritical}$). Through a specified porous medium, any flow rate smaller than the $Q_{ritical}$ creates unstable incoherent flow (i.e., $Q_g < Q_{critical}$ results in unstable flow and $Q_g > Q_{critical}$ results in stable flow).

The stability condition can be interpreted in two ways:

 (1) If the specific pore size distribution of certain sediment is known, the mean gas channel can be estimated. Then, Eq. (2.18) gives the critical flow rate needed to reach stable, channelized flow. Thus for a certain sediment, increasing the flow rate may yield a transition from incoherent bubbly flow to coherent channelized flow.
 (2) If a certain flow rate Q_{ch} is known, then, Eq. (2.18) gives the mean gas channel. One can considered different sediments (e.g., 0.5 mm-, 1 mm- and 2 mm-GBS), but, larger sediments have larger pore size radii, where the injection tends to create unstable incoherent bubbly flow more than through the finer sediments.

If the mean radius of capillaries in 0.5 mm-GBS is considered equal to the minimum pore radius (i.e., r_{ch} = 0.055 mm), then, the critical flow rate becomes equal to 0.11 ml/min. Beside that, the corresponding flow rate to establish the stable channel with mean radius of 0.14 mm (equal to the maximum pore radius in 0.5 mm-GBS) is equal to 4.67 ml/min. Hence, it can be concluded that for the lowest experimental flow rate of 10 ml/min, the stability criterion is satisfied, and one expects that stable gas channels develop within the 0.5 mm-GBS.
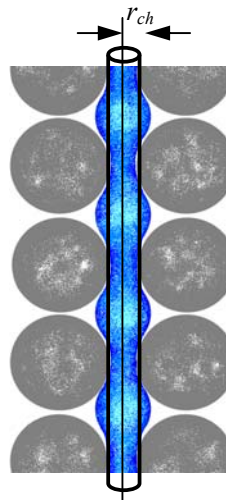
Fig. 2.9: Steady-state coherent gas flow through an undulating capillary.

2.3   Definition of the scales, and validity range for continuum modeling

The microscopic fluid flow process and the forces acting at the pore-scale, have been discussed in previous sections. But, it is extremely difficult to model the pore-scale processes which occur in a porous medium that involves millions of connected pores. There are two different conceptual models that simplify the real multi-phase flow process through the porous media: (1) the discrete model (e.g. pore network model), (2) the continuum model. Each of these models has its own advantages and disadvantages:

(1)   The discrete model applies the realization probabilities to describe the properties of porous medium, and then to model the fluid flow at the pore-scale.

(2)   The continuum model uses average properties over pore-scale and introduces effective properties at macroscopic-scale instead of pore-scale. The volume that represents the average properties at macroscopic-scale is called Representative Elementary Volume (REV). In this work, the REV is defined by using the concept of porosity (ϕ) that is defined in Eq. (2.19).

$$\phi = \frac{V_p}{V} \tag{2.19}$$

where,
V = bulk volume, [L^3]
V_p = volume of void space within the bulk volume, [L^3]

When the bulk volume is chosen large, but smaller than the volume of whole porous medium, the porosity values fluctuate due to the different geological rock types (e.g., fine sand, medium sand, or coarse sand). If the arbitrary bulk volumes are chosen within a specific rock type, the fluctuation in porosity decreases gradually when the bulk volume shrinks (Fig. 2.10). The fluctuation in porosity values exists until the bulk volume V_1 is reached. If the bulk volume is chosen smaller than V_1, the porosity value remains constant until the bulk volume becomes equal to V_0. The porosity exhibits oscillations, if the bulk volume becomes smaller than V_0.

Therefore, any arbitrary volume chosen between the V_0 and V_1 is REV, in which the properties do not depend on volume and remain constant. The V_0 and V_1 are called the minimum and maximum REV.

When V tends to zero the volume shrinks to a point, and depends on whether the point is placed inside a pore or within the solid matrix, the porosity becomes equal to 0 or 1, respectively.

Fig. 2.10 shows different scales that are defined by using the concept of REV. All the REVs between V_0 and V_1 yield the properties that could refer to the whole porous medium. This scale is called REV-scale (macroscopic-scale, or bench-scale). The scale smaller than the minimum REV (i.e., $V < V_0$), is called pore-scale (microscopic-scale), and the scale larger than the maximum REV (i.e., $V > V_1$) is called field-scale (Fig. 2.10).

Since the porosity is defined over the REV-scale, adding or subtracting one or several pores have no effect. Therefore, the porosity is considered a continuous property within the porous medium. By introducing the concept of continuous properties, the porous medium can be replaced by a fictitious continuum, where a property can be assigned to any point within the porous medium. Then, the multiphase flow through a porous medium can be replaced by a number of overlapping continua that fills the entire porous medium (e.g., solid phase, gas phase, and water phase in a gas-water system). The kinematic and dynamic variables of each continua at macroscopic-scale create the continuous functions (Bear 1972). The corresponding system of differential equations, which describe the behavior of continuum phases through a porous medium, is called continuum model. The solution of the continuum model gives average spatial and temporal behavior of fluid phases at macroscopic-scale. Therefore, important properties of the porous media will be introduced in the next section, before concentrating the differential equations of a continuum model.
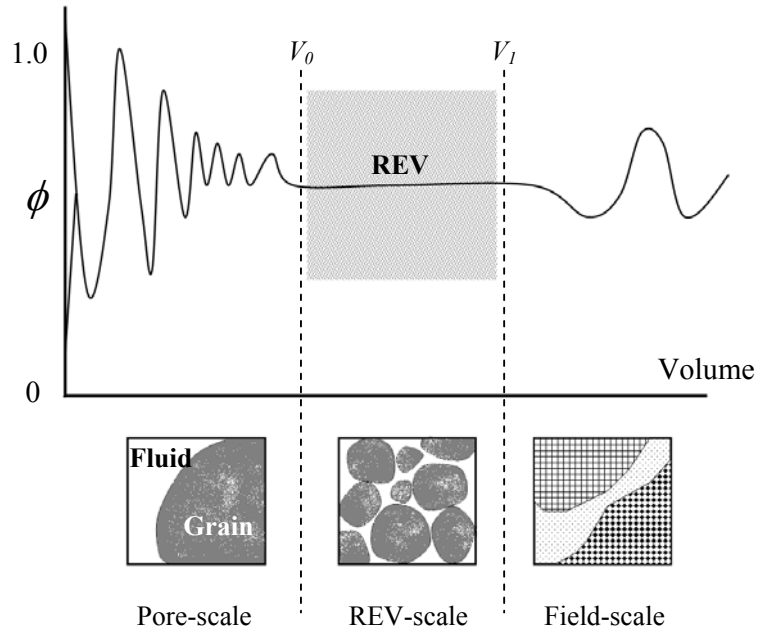
Fig. 2.10: Illustration of REV concept by presenting the variation in porosity at different scales (Bear, 1972).

2.3.1   Characteristic variables of porous media and phase properties

The bulk volume of a porous medium consists of the rock matrix and the void spaces (pores). The ratio of the pore volume and the bulk volume defines the porosity in Eq. (2.19). Two different types of porosity can be identified: the total porosity, and the effective porosity. Total porosity includes the connected and non-connected pores, while the effective porosity only considers the pores that participate in fluid flow.

Any changes in pore pressure affect the porosity value. Therefore, the isothermal compressibility of porosity is defined to specify the changes in pore volume. However equation (2.20) shows the classical definition of isothermal compressibility of porosity, but in most cases the compressibility of porosity (c_ϕ) is considered as a constant number.

$$c_\phi = \frac{1}{\phi}\left(\frac{\partial \phi}{\partial P}\right)_T \tag{2.20}$$

where,
P = pore pressure, [M L^{-1} T^{-2}]

In a multi-phase system, the fraction of bulk volume filled by fluid phase i, is called the volumetric content, θ_i. For example, in gas-water system, the volumetric content of water and gas phases, θ_g and θ_w, are defined as follows:

$$\theta_w = \frac{V_w}{V} \text{ and } \theta_g = \frac{V_g}{V} \tag{2.21}$$

Where, V_w and V_g are the volume of water and gas phase, respectively. The following constraint holds for phase contents:

$$\theta_w + \theta_g = \phi$$

The volumetric content relative to the porosity gives the corresponding phase saturation, S_i. Then, water and gas saturation, S_w and S_g, of gas-water system are defined as:

$$S_w = \frac{V_w}{V_p} \; , \; S_g = \frac{V_g}{V_p} \tag{2.22}$$

where the following constraint holds for saturations:

$$S_w + S_g = 1.0$$

The most important variables characterize a multi-phase system are density and viscosity, which depend on temperature and phase pressure. The density of phase i (ρ_i), is defined as the mass of phase per unit volume. The density of water and gas are presented in Eq. (2.23).

$$\rho_w = \frac{m_w}{V_w}, \; \rho_g = \frac{m_g}{V_g} \tag{2.23}$$

The dynamic viscosity (μ) is caused by the intermolecular attraction forces that impede the displacement of molecules. This is Newton's classical law for friction or viscous forces of laminar flow, which the Hagen-Poiseuille law is derived based on. After Newton, the shear stress is defined as follows, where the proportionality constant is called dynamic viscosity:

$$\tau_s = \mu \frac{\partial v}{\partial s} \tag{2.24}$$

where,
v = velocity of fluid parallel to the boundary layer, [L T^{-1}]
s = thickness, [L]

2.4 Packing density, pore size distribution, and channel diameter for a glass-bead pack

This work focuses on the bench-sale experiments performed by Krauss (2007), in which different size of glass beads (i.e., 0.5 mm-, 1 mm- and 2 mm-GBS) are used. Consequently, the hydraulic properties of a GBS, which can be applied in multi-phase flow modeling, are investigated in this section.

2.4.1 Porosity and permeability values

In Krauss (2007), the porosity of different GBS is measured gravimetrically. The experimental values of porosity are 0.36 for 0.5 mm- and 2 mm-GBS, and 0.39 for 1mm-GBS. Dullien (1992) introduced four packing groups: (1) very loose random packing with $\phi = 0.44$, (2) loose random packing with $\phi = 0.40 - 0.41$, (3) poured random packing with $\phi = 0.375 - 0.391$, and (4) close random packing with $\phi = 0.359 - 0.375$. Hence, all GBS are closely random packed, which is the best packing that can be reached for laboratory experiments.

By using these values, a theoretical estimation of permeability can be calculated by Kozeny-Carman equation (Bear, 1972):

$$k_{KC} = \frac{d_m{}^2}{180} \frac{\phi^3}{(1-\phi)^2}$$

(2.25)

where,
k_{KC} = permeability value by Kozeny-Carman, [m^2]
d_m = mean particle size, [m]

Krauss (2007) obtained the permeability value of each GBS in bench-scale experiments. The comparison between the theoretical permeability values, which are calculated by the Kozeny-Carman equation, and the experimental values listed in Table 2.1 for three different GBS. The values of mean and standard deviation of permeability field were estimated from the permeability values obtained in several experiments.

Table 2.1: Comparison of experimental permeability (k_{exp}) and the theoretical permeability by Kozeny-Carman (k_{KC}) for three different GBS (Geistlinger et al., 2006).

Experiment	k_{exp} (m^2)	k_{KC} (m^2)
0.5 mm GBS	$9.23 \pm 0.36 \times 10^{-11}$	8.90×10^{-11}
1 mm GBS	$5.50 \pm 0.14 \times 10^{-10}$	4.84×10^{-10}
2 mm GBS	$2.34 \pm 0.14 \times 10^{-9}$	2.53×10^{-9}

2.4.2 Pore size distribution

Sahimi (1999) proposed an empirical relationship between porosity and coordination number (Z) for the random packed spheres:

$$\phi = 0.0043\langle Z \rangle^2 - 0.1193\langle Z \rangle + 1.072$$

(2.26)

The minimal and maximal coordination numbers for the packed glass beads are given by simple cubic and cubic-face-centered packing are measured, respectively, which are equal to 6.8 and 12. The simple cubic and cubic-face-centered packing are shown in Fig. 2.11. By using Eq. (2.26), one obtains the coordination number 8.7 for 0.5 mm- and 2 mm-GBS, and 8.1 for 1 mm-GBS.

The maximum and minimum values of pore diameter, d_{max} and d_{min}, that exist within glass beads can be calculated according to Busch et al. (1993):

$$d_{max} = \zeta_{max} . d_k = (0.458...0.732)\, d_k$$

(2.27 (a))

$$d_{min} = \zeta_{min} . d_k = (0.155...0.414)\, d_k$$

(2.27 (b))

where,
ζ_{min} = minimum dimensionless diameter in units of d_k, [-]

In Eqs. (2.27a) and (2.27b), the minimum and maximum values in parentheses correspond to the cubic-face-centered and simple cubic packing. Therefore, the linear interpolations in Eqs. (2.27a) and (2.27b) give the corresponding values of ζ_{min} and ζ_{max} equal to 0.30 and 0.61 for $Z = 8.7$ (0.5 mm- and 2 mm-GBS), and 0.33 and 0.64 for $Z = 8.1$ (1 mm-GBS).

(a)   (b)

Fig. 2.11: Visualization of: (a) simple cubic packing, and (b) cubic-face-centered packing (Geistlinger et al., 2006).

The value of mean pore radius (r_c) is an important parameter that can be calculated by the minimum and maximum pore radii:

$$r_c = 0.25\left(\zeta_{min} + \zeta_{max}\right) d_k \tag{2.28}$$

Three different types of glass beads (0.5 mm-, 1 mm- and 2 mm-GBS) are used by Krauss (2007) in bench-scale experiments. The details about the bench-scale experiments come in Chapter4, but Table 2.2 gives the geometric characterizations (e.g., the minimum and maximum pore size, the values of induced capillary pressure, and the critical flow rate in different glass beads).

Table 2.2: Geometric properties of three different GBS.

Sediment Name	0.5 mm GBS	1 mm GBS	2 mm GBS
Average d_k (mm)	0.375	0.875	2.1
d_{min} [a] (mm)	0.11	0.28	0.60
d_{max} [b] (mm)	0.23	0.56	1.3
r_c [c] (mm)	0.085	0.21	0.48
P_{c1} [d] (mbar)	8.5	3.4	3.0 [e]
P_{c2} [f] (mbar)	12.9	5.1	4.6 [e]
P_{c3} [g] (mbar)	16.9	6.8	3.0
$P_{c,exp}$ (mbar)	15.9	8.0	3.2
Q_g [h] (ml/min)	0.1 - 0.6	4.7 - 22	110 - 594

[a] calculated according to Eq. (2.27a)
[b] calculated according to Eq. (2.27b)
[c] calculated according to Eq. (2.28)
[d] capillary pressure calculated by Eq. (2.2), $r_1 = r_c$ and $r_2 = \infty$
[e] according to the conceptual model in Fig. 2.7
[f] capillary pressure calculated by Eq. (2.2), $r_1 = d_{min}/2$ and $r_2 = \infty$
[g] capillary pressure calculated by Eq. (2.2), $r_1 = r_2 = r_c$ (Eq. (2.28))
[h] critical flow rate to establish the channelized flow (Eq. (2.18))

In the literature, it is argued that the pore size distribution can be described by the log-normal function (e.g., by Kosugi, 1996). It other words, the probability density function (pdf) of pore radii can be characterized by a lognormal function, that is for example presented in Eq. (2.29).

$$f(r) = \frac{1}{\sqrt{2\pi}\ \sigma_{dev}\ r} \exp\left(-\left[\frac{\ln(r) - r_m}{\sqrt{2}\ \sigma_{dev}}\right]^2\right)$$

<div align="right">(2.29)</div>

where,

$f(r)$ = pdf function of pore radii, [-]

r = pore radius, [L]

r_m = mean value of pore size distribution, [L]

σ_{dev} = standard deviation of pore size distribution, [L]

The values in Table 2.2 are used to estimate the mean value and the standard deviation of pore radii for different GBS. Fig. 2.12 shows the log normal distribution of pore radii of 0.5 mm-GBS (with r_m = 0.09 mm and σ_{dev} = 0.03 mm), and 1 mm-GBS (with r_m = 0.21 mm and σ_{dev} = 0.07 mm). The gray areas under the pdf function show the corresponding pore radii through 0.5 mm- and 1 mm-GBS that can be invaded when gas saturation is measured equal to 10 % in both GBS.
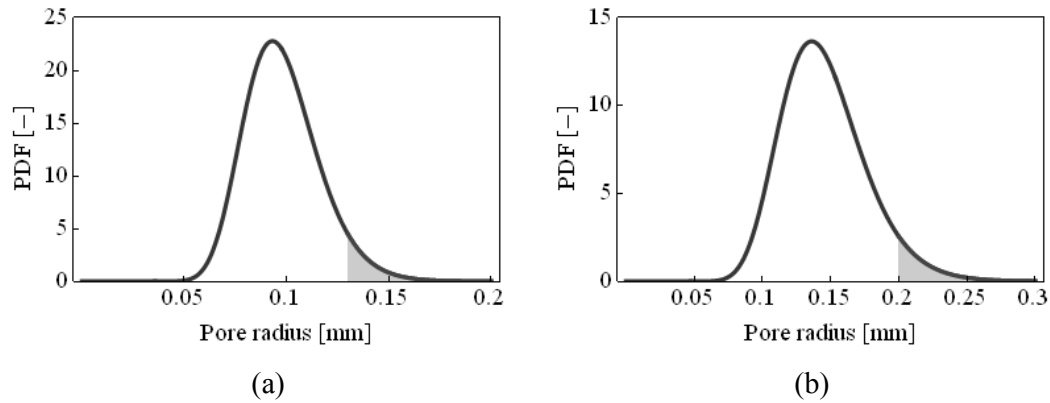
Fig. 2.12: The pore size distribution for: (a) 0.5 mm-GBS, and (b) 1 mm-GBS. The pdf functions are plotted by Mathematica (version 7.0, Wolfram Research, Inc., Champaign, IL, 2008).

In capillary bundle model, the porous medium is simplified as a bundle of capillaries, in which the capillary radii have the same distribution of pore radii described in Eq. (2.29). The relationships (e.g., capillary pressure-saturation relationship) derived from pore-scale models (e.g., capillary bundle model that uses pore size distribution), are effective description on larger scale (e.g., bench-scale or field-scale). These relationships are the basis or constitution of two-phase continuum theory. Therefore, they are called constitutive relationships.

2.5 Constitutive relationships

As it was stated in previous section, the constitutive relationships can be derived by using different pore-scale models. This section does not discuss different pore-scale models, which are used to build an effective description of multi-phase dynamics within the porous media.

Instead, an overview of three different approaches is presented, which are often used in the literature to calculate the relative permeability function (relative permeability-saturation relationship, $k_{rw}(S_{wet})$) for unsaturated porous media by using the retention curve of wetting phase.

1) Purcell approach (Purcell, 1949) that ignores the effect of tortuosity.
2) Burdine approach (Burdine, 1953) that includes the tortuosity factor.
3) Mualem approach (Mualem, 1976).

These approaches yield different relative permeability functions that are explained briefly in this section.

Purcell approach

Purcell (1949) developed an approach to obtain the relative permeability of water phase by using the capillary pressure function (capillary pressure-saturation relationship, $P_c(S_{wet})$). Purcell (1949) simply considered the porous medium consists of a bundle of capillaries with varying sizes.

The relative permeabilities in Purcell approach (1949) for a two-phase flow system, which consists of wetting and non-wetting phases, are equal to:

$$k_{r\,wet} = \frac{\int_0^{S_{wet}} dS_{wet}/(P_c)^2}{\int_0^1 dS_{wet}/(P_c)^2} \tag{2.30}$$

$$k_{r\,nwet} = \frac{\int_{S_{wet}}^1 dS_{wet}/(P_c)^2}{\int_0^1 dS_{wet}/(P_c)^2} \tag{2.31}$$

where,

$k_{r\,wet}$ = relative permeability of wetting phase, [-]
$k_{r\,nwet}$ = relative permeability of non-wetting phase, [-]
S_{wet} = saturation of wetting phase, [-]

In both equations, P_c is the capillary pressure-saturation relationship. At a specific saturation, the summation of Eqs. (2.30) and (2.31) equals to one. Since this condition is not true in general, the Purcell approach (1949) is not considered in this work.

Burdine approach

The Burdine approach (1953) is similar to the Purcell approach (1949), but it applies the tortuosity ratio in the equations.

$$k_{r\,wet} = (\lambda_{wet})^2 \frac{\int_0^{S_{wet}} dS_{wet}/(P_c)^2}{\int_0^1 dS_{wet}/(P_c)^2} \tag{2.32}$$

$$k_{r\,nwet} = \left(\lambda_{nwet}\right)^2 \frac{\int_{S_{wet}}^{1} dS_{wet} / \left(P_c\right)^2}{\int_{0}^{1} dS_{wet} / \left(P_c\right)^2} \tag{2.33}$$

where,
λ_{wet} = tortuosity ratio of the wetting phase, [-]
λ_{nwet} = tortuosity ratio of the non-wetting phase, [-]

Burdine (1953) stated that the tortuosity ratio can be calculated as follows:

$$\lambda_{wet} = \frac{\tau_{wet}(1.0)}{\tau_{wet}(S_{wet})} = \frac{S_{wet} - S_{min}}{1 - S_{min}}$$

$$\lambda_{nwet} = \frac{\tau_{nwet}(1.0)}{\tau_{nwet}(S_{wet})} = \frac{1 - S_{wet} - S_{eq}}{1 - S_{min} - S_{eq}}$$

where,
S_{min} = minimum saturation of wetting phase in the capillary pressure curve, [-]
S_{eq} = equilibrium saturation of the non-wetting phase, [-]

Mualem approach
Mualem (1976) assumed that the pores are randomly connected to each other and the Hagen-Poiseuille law is valid for fluid flow through the pores. In Mualem model (1976) the effect of tortuosity and variety of pore radii is represented by a power function of effective saturation.
The relative permeability function of wetting phase in this model is:

$$k_{r\,wet} = \left(S_e\right)^{\tau} \left[\frac{\int_{r_{min}}^{r} r\,f(r)\,dr}{\int_{r_{min}}^{r_{max}} r\,f(r)\,dr}\right]^2 \tag{2.34}$$

where,
τ = tortuosity factor, [-]
S_e = effective saturation of wetting phase, which is equal to:

$$S_e = \frac{S_{wet} - S_{wet\,r}}{S_m - S_{wet\,r}}$$

where,
$S_{wet\,r}$ = residual saturation of wetting phase, [-]
S_m = maximum saturation of wetting phase, [-]

In Eq. (2.34), Mualem model integrated the pdf function of pore radii ($f(r)$). It means that Mualem model derives the effective property from the pore-scale. Therefore, this model gives a pore-scale constitutive relationship, which is much more fundamental than Purcell and Burdine models.
By using Laplace-Young equation, Mualem (1976) derived the final equation for relative permeability of wetting phase:

$$k_{r\,wet} = \left(S_e\right)^{\tau} \left[\frac{\int_{0}^{S_e} dS_e / h(S_e)}{\int_{0}^{1} dS_e / h(S_e)}\right]^2 \tag{2.35}$$

He assumed the Hagen-Poiseuille law is valid for the flow through the pores that results in $k \sim r^2$. Thus, the pore radius, does not exist in the porous medium, can dominate the behavior of relative permeability function. Therefore, if the water retention curve is not chosen properly in Eq. (2.35), it is possible that the arbitrary large pore sizes dominate the behavior of relative permeability function.

Following Roth (2006), one can substitute different capillary pressure-saturation relationship in these approaches to derive the relative permeability function. The van Genuchten-Mualem (1980) and Brooks-Corey (1966) models are mostly used in the simulation work in the literature (Roth, 2006; Ippisch et al., 2006). Therefore, these two models are developed and utilized in this work.

The van Genuchten-Mualem model
In 1980, van Genuchten proposed the retention curve of wetting phase as a power function of effective saturation:

$$h(S_e) = \frac{1}{\alpha_p} \left(S_e^{-1/m} - 1 \right)^{1/n} \tag{2.36}$$

where,
$h(S_e)$ = matrix potential, [M L^{-1} T^{-2}]
α_p = reciprocal of entry pressure, [M^{-1} L T^2]
m and n = pore size distribution indices in van Genuchten-Mualem model, [-]

The entry pressure (P_e) is the minimum capillary pressure to invade the fully saturated porous medium, at which a continuous non-wetting phase exists. In other words, the entry pressure is a measure of maximum pore size (Honarpour, 1986). In Eq. (2.36), parameter n is a constant value interpreted as the width of the pore size distribution of the porous medium, which shows the sparseness of the pore radii between the maximum and minimum pore sizes. Substituting Eq. (2.36) into Eq. (2.35) yields:

$$k_{r\,wet} = \left(S_e \right)^{\tau} \left[\frac{\int_0^{S_e} dS_e / \left(S_e^{-1/m} - 1 \right)^{1/n}}{\int_0^1 dS_e / \left(S_e^{-1/m} - 1 \right)^{1/n}} \right]^2 \tag{2.37}$$

Van Genuchten (1980) showed that the integrals in Eq. (2.37) can be solved by considering $m = 1 - 1/n$, and obtained:

$$k_{r\,wet} = \left(S_e \right)^{\tau} \left[1 - \left(1 - S_e^{1/m} \right)^m \right]^2 \tag{2.38}$$

Eq. (2.38) is the van Genuchten-Mualem model, which is called classical model by Ippisch et al. (2006). Ippisch et al. (2006) expanded the Mualem model (i.e. Eq. (2.35)) based on the retention curve:

$$k_{r\,wet} = \left(S_e \right)^{\tau} \left[\int_{h(S_e)}^{\infty} \frac{1}{h(S_e)} \frac{dS_e}{dh} dh \middle/ \int_{h(S_e=1)}^{\infty} \frac{1}{h(S_e)} \frac{dS_e}{dh} dh \right]^2 \tag{2.39}$$

They argued that the denominator in Eq. (2.39) gives reasonable results if the dS_e / dh reduces faster than the increasing of h when S_e tends to 1.0 (i.e., the full saturated

condition). On the other hand, the dS_e / dh, which is the derivation of Eq. (2.36) and comes in Eq. (2.40), fulfills this condition only if $n > 2$ (Ippisch et al., 2006).

$$\frac{dS_e}{dh(S_e)} = -\alpha_p \, mn \left(\alpha_p \, h\right)^{n-1} \left[1 + \left(\alpha_p \, h\right)^n\right]^{-(m+1)}$$

(2.40)

Ippisch et al. (2006) argued the condition $n > 2$ only guarantees that the permeability function is not influenced by infinitely large pores. Therefore, they recommended that the value of α_p^{-1} should be larger than the real entry pressure that exists in the porous medium. In other words, if the real entry pressure of the porous medium is considered equal to h_a, then $\alpha_p h_a < 1$, to exclude all pores with radius larger than the biggest pore size (i.e., r_{max}). Then, Ippisch et al. (2006) modified the van Genuchten-Mualem model and argued that in case of $n < 2$ or $\alpha_p^{-1} < h_a$, the modified van Genuchten-Mualem or another model that includes the entry pressure (e.g., Brooks-Corey model), should be used instead of classical van Genuchten-Mualem model (1980).

The Brooks-Corey model

Brooks and Corey (1966) proposed the following function to express the capillary pressure-saturation relationship:

$$P_c = P_e \, S_e^{-1/\lambda}$$

(2.41)

where,
λ = pore size distribution index in Brooks-Corey model, [-]

The parameter λ in Eq. (2.41) is equivalent of parameter n in Eq. (2.36) (i.e., λ is a measure of pore size distribution of the porous media). The Brooks-Corey model consists of an air entry value that corresponds to the largest pore size, therefore it avoids modification due to the largest unrealistic pore size.

The relative permeability functions of wetting and non-wetting phases are derived by substituting Eq. (2.41) into the Eqs. (2.32) and (2.33), respectively, while it is assumed $S_{eq} = 0$ and $S_{min} = S_{wr}$ in Burdine approach. The Eqs. (2.42) and (2.43) are called relative permeability functions of Brooks-Corey model.

$$k_{r\,wet} = S_e^{(2+3\lambda)/\lambda}$$

(2.42)

$$k_{r\,nwet} = \left(1 - S_e\right)^2 \left[1 - S_e^{(2+\lambda)/\lambda}\right]$$

(2.43)

The van Genuchten-Mualem model is continuous over the whole saturation range, it means the function has no "jumps" in this region like the Brooks-Corey model. Due to this mathematical advantage, the van Genuchten model is the most commonly used constitutive relationship in the literature. On the other hand, its continuity at complete saturation must assume infinite large pore radii. This is an unphysical drawback of the van Genuchten-Mualem mod``el.

2.5.1 Constitutive relationships obtained from capillary bundle model

Kosugi (1996) derived the capillary pressure-saturation relationship, depending on the pore size distribution. Thus, the effective relationship at larger scales is derived from pore-scale characteristics. Deriving the constitutive relationships from the capillary bundle model gives the advantage of using the physical properties of the porous medium.

Gas is a non-wetting phase that initially invades the largest pores spaces in a real gas-water flow. Therefore, the gas saturation in capillary bundle model can be calculated by integration over the largest gas-filled capillaries as follows:

$$S_g = \frac{\int_{r_{gf}}^{r_{max}} V_{cap}(r) f(r)\, dr}{\int_{r_{min}}^{r_{max}} V_{cap}(r) f(r)\, dr} \tag{2.44}$$

where,

r_{gf} = smallest gas-filled capillary radius, [L]
$V_{cap}(r)$ = the volume of a capillary with radius r, [L^3]

Eq. (2.44) can be solved to obtain the smallest gas-filled capillary radius for any value of gas saturation. Moreover, the capillary pressure-saturation relationship can be calculated for the whole range of gas saturation by using Laplace-Young equation (see Eq. (2.2)). This capillary pressure-saturation relationship, which is developed by using the capillary bundle model, is called Kosugi-relationship.

Fig. 2.12 shows the pore size distribution of 0.5 mm- and 1 mm-GBS, where the gray area under the curve indicates 10 % gas saturation for both GBS. The corresponding r_{gf} value for 10 % gas saturation within 0.5 mm- and 1 mm-GBS is equal to 0.13 mm and 0.20 mm, respectively.

For the upper boundary in the integration (r_{max} in Eq. (2.44)), a finite capillary radius was estimated, which results in a finite entry pressure in capillary pressure-saturation relationship. The cutoff values of the pore size distribution are considered equal to 0.11, 0.15 and 1 mm for 0.5 mm-GBS, and equal to 0.1, 0.28 and 0.35 for 1 mm-GBS.

Fig. 2.13 shows the capillary pressure curves obtained by log-normal distributions of pore radii in 0.5 mm- and 1 mm-GBS based on Kosugi-relationship. This figure shows the capillary pressure curves of Kosugi-relationship for different cutoff values (thick blue lines), fitting capillary pressure curve of van Genuchten-Mualem model (dashed green lines), and fitting capillary pressure curve of Brooks-Corey model (dashed red lines).

In 1 mm-GBS, there is no difference between the capillary pressure curves obtained by different cutoff values, but in 0.5 mm-GBS, the capillary pressure curves with cutoff r_{max} = 0.11 mm deviates from capillary pressure curve of Kosugi-relationship. In addition, the experimental capillary pressures, which are measured at the lowest injection rate (i.e., Q_g = 10 ml/min), are shown by black dots in Fig. 2.13. Therefore, the cutoff values equal to 0.15 mm and 0.35 mm are selected for 0.5 mm- and 1 mm-GBS respectively, because the corresponding capillary pressure curves fit to the experimental values.
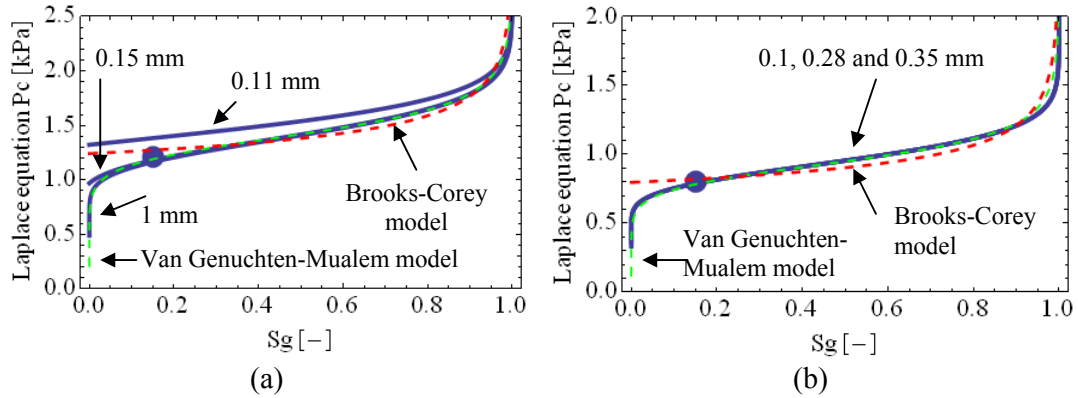
Fig. 2.13: The capillary pressure curves for: (a) 0.5 mm-GBS and (b) 1 mm-GBS. The black dotes represents the experimental values of capillary pressure measured in bench-scale experiments.

The parameters of capillary pressure-saturation relationship in van Genuchten-Mualem model (1980) and Brooks-Corey model (1966) are estimated by curve fitting in Fig. 2.13. Table 2.3 and Table 2.4 represent the corresponding parameters of van Genuchten-Mualem model and Brooks-Corey model, respectively. Since n values estimated based on the experimental measurements are bigger than two for both 0.5 mm- and 1 mm-GBS (see Table 2.3), therefore it is not necessary to use the modified van Genuchten-Mualem model.

Table 2.3: Parameters of van Genuchten-Mualem model for 0.5 mm- and 1 mm-GBS.

Parameter	0.5 mm-GBS	1 mm-GBS
α_p (m^{-1})	7	10.5
n in Eq. (2.36)	10	9.2
S_{wr}	0.01	0.01
$S_m = 1 - S_{nwr}$	1.0	1.0

Table 2.4.: Parameters of Brooks-Corey model for 0.5 mm- and 1 mm-GBS.

Parameter	0.5 mm-GBS	1 mm-GBS
α_p (m^{-1})	8.2	12.3
λ in Eq. (2.41)	6.514	5.5
S_{wr}	0.01	0.01
$S_m = 1 - S_{nwr}$	1.0	1.0

3   Continuum Theory and Numerical Modeling

The importance of multi-phase flow modeling has been investigated in soil physics, hydrogeology and petroleum engineering. There are many difficulties associated with conceptualization and modeling of multi-phase flow, because of the complexity of the physical processes and inadequate measured data. But, various models and mathematical approaches have been developed to describe multi-phase flow. For instance, Lattice-Boltzmann simulation and pore network modeling are used to simulate the multi-phase flow at the pore-scale. These models are based on realistic pore size distributions, which can be measured with X-ray computer tomography (Vogel et al., 2010). In addition, the dynamics of these models are developed based on simplifying rules and assumptions about the dominance of the forces acting at pore-scale. If one accepts these rules and assumptions, then multi-phase flow at the pore-scale can be investigated by using these models. On the other hand, continuum models utilize the classical fluid flow laws (e.g., Navier-Stokes equation) and classical thermodynamics laws (e.g., Fourier law). In contrast to pore-scale modeling, continuum models are developed based on the continuum theory, which assumes that the average properties over REV (e.g., average permeability and capillary pressure values) can be considered as the properties of the whole multi-phase system. The continuum model is applied in this work to describe the gas-water flow at macroscopic scale.

3.1   Mathematical model of continuum multi-phase flow

The classical continuum model for two-phase flow is developed based on generalized Darcy's law and equation of mass conservation (continuity equation). To be instructive, first the physics of Darcy's law and its generalization for gas-water system is presented. Then, Darcy's law is applied in equation of mass conservation to develop the flow equations for gas-water system.

The experimental law of Darcy

The Darcy's law is an empirical relation that Henry Darcy published in 1856 based on his experimental results. Darcy (1856) found that the volumetric flow rate of water between two measuring points is proportional to the cross sectional area, and the piezometric head (h_1 - h_2), and inversely proportional to the filter length measured between these two points. Eq. (3.1) represents the Darcy's law, in which K is the coefficient of proportionality.

$$Q = KA\frac{(h_1 - h_2)}{L} \qquad \qquad (3.1)$$

where,
Q = volumetric flow rate of water, [L^3 T^{-1}]
A = cross-sectional area, [L^2]
L = filter length, [L]

The piezometric head, which is measured respect to a datum or a reference level, is the sum of pressure head and potential energies per unit weight of fluid. In Darcy's law, the piezometric head can be interpreted as hydraulic head of water and is given by:

$$h = \frac{P_w}{\rho_w g} - z \tag{3.2}$$

where,
P_w = pressure of water, [M L^{-1} T^{-2}]
z = elevation, [L]

The coefficient of proportionality in Darcy's law (see Eq. (3.1)) is called hydraulic conductivity that represents how ease a fluid phase can be transported through a porous medium. Hydraulic conductivity is not only a function of rock characteristics (e.g., pore size distribution, and tortusity), but it also depends on fluid properties (e.g., density and viscosity) (Bear, 1972). The definition of hydraulic conductivity of water is presented in Eq. (3.3), in which the absolute permeability value, k, quantifies the resistance of the porous media to transport the fluid, which depends only on the rock properties.

$$K = k \frac{\rho_w g}{\mu_w} \tag{3.3}$$

Using the definition of volumetric flux, q, (volumetric flow rate per unit cross sectional area normal to the direction of flow) another form of Darcy's law can be obtained:

$$q = -K \nabla h \tag{3.4}$$

where, ∇ denotes the Nabla operator yielding the spatial gradient of the scalar function, $h(x,y,z)$.

Generalized Darcy's law
Darcy's law is derived for a single-phase flow system. Muskat (1949) extended Darcy's law for the multi-phase flow system. In multi-phase flow system, the volumetric flux of the phase i (q_i), has the following form:

$$q_i = -\frac{k\,k_{ri}}{\mu_i} \nabla(P_i - \rho_i\,gz) \tag{3.5}$$

where,
k_{ri} = relative permeability function of phase i, [-]
P_i = pressure of phase i, [M L^{-1} T^{-2}]

The volumetric flux in Eq. (3.5) is also called Darcy velocity of phase i. In a gas-water system, the volumetric fluxes of water and gas phases, q_w and q_g, are equal to:

$$q_w = -\frac{k\,k_{rw}}{\mu_w} \nabla(P_w - \rho_w gz) \tag{3.6}$$

$$q_g = -\frac{k\,k_{rg}}{\mu_g} \nabla(P_g - \rho_g gz) \tag{3.7}$$

where, k_{rw} and k_{rg} are relative permeability functions of water and gas phases, respectively. The concept of relative permeability is based on the assumption that all immiscible phases can flow simultaneously through the porous medium. It means that, one phase can flow through the pores that may be saturated partially by other phases.

The concept of relative permeability extends the fluid flow equations from single-phase to the multi-phase flow system. Muskat (1949) emphasized that the relative permeability functions are only determined by saturation distribution. Section 2.5 describes different approaches to obtain the relative permeability functions for wetting and non-wetting phases in a multi-phase flow system.

Equation of mass conservation

The equation of mass conservation (equation of continuity) expresses the conservation of mass respect to the time and space (Bear, 1972). The equation of mass conservation for phase i of a multi-phase flow through a constant control volume is presented in Eq. (3.8).

$$\frac{\partial(\rho_i\,S_i\,\phi)}{\partial t} + \nabla\cdot(\rho_i\,q_i) = I_i \qquad (3.8)$$

where,

t = time, [T]

I_i = volumetric mass rate of production or injection of phase i, [M L^{-3} T^{-1}]

Physically, Eq. (3.8) represents that the mass changes respect to time is equal to the mass flux and the summation of mass injection or mass production. In Eq. (3.8), the Nabla operator yields the divergence of the vector function $\rho_i\,q_i$.

The equations of mass conservation for water and gas phases, in which the volumetric mass rate of production and injection of water and gas phases are considered equal to I_w and I_g, are respectively:

$$\frac{\partial(\rho_w\,S_w\,\phi)}{\partial t} + \nabla\cdot(\rho_w\,q_w) = I_w \qquad (3.9)$$

$$\frac{\partial(\rho_g\,S_g\,\phi)}{\partial t} + \nabla\cdot(\rho_g\,q_g) = I_g \qquad (3.10)$$

3.1.1 Mathematical model for a gas-water flow system

The flow equation of phase i in a multi-phase flow system is obtained by substituting the volumetric flux of phase i (q_i in Eq. (3.5)) in the equation of mass conservation (Eq. (3.8)). Hence, the flow equations of the water and gas phases within a gas-water flow system become:

$$\frac{\partial(\rho_w\,S_w\,\phi)}{\partial t} + \nabla\cdot\left(-\rho_w\,\frac{k.k_{rw}}{\mu_w}\,\nabla(P_w - \rho_w g\,z)\right) = I_w \qquad (3.11)$$

$$\frac{\partial(\rho_g\,S_g\,\phi)}{\partial t} + \nabla\cdot\left(-\rho_g\,\frac{k.k_{rg}}{\mu_g}\,\nabla(P_g - \rho_g g\,z)\right) = I_g \qquad (3.12)$$

In this system, water and gas phase fill all the pore spaces, in which the following constrain holds:

$$S_w + S_g = 1.0 \qquad (3.13)$$

Based on the classical definition of capillary pressure in Section 2.1.1, the capillary pressure is defined as pressure difference between the gas and water phase:

$$P_c(S_w) = P_g - P_w \qquad (3.14)$$

Expressing the gas pressure of Eq. (3.12) by the capillary pressure gives the following flow equation for the gas phase, in which has the independent variables are S_w and P_w.

$$\frac{\partial\left(\rho_g\,\phi\left(1-S_w\right)\right)}{\partial t} - \nabla\cdot\left(\rho_g\,k\,\frac{k_{rg}}{\mu_g}\nabla\left(P_c + P_w - \rho_g gz\right)\right) = I_g \qquad (3.15)$$

The expansion of Eqs. (3.11) and (3.15) for 1D (e.g., in z-direction) and for Newtonian fluids leads to the following system of non-linear partial differential equations:

$$\begin{cases} \rho_w\,\phi\dfrac{\partial\left(S_w\right)}{\partial t} - \rho_w\dfrac{k}{\mu_w}\dfrac{\partial k_{rw}}{\partial z}\left(\dfrac{\partial P_w}{\partial z} - \rho_w g\right) = I_w \\[3mm] -\phi\dfrac{\partial\left(\rho_g\,S_w\right)}{\partial t} - \dfrac{k}{\mu_g}\dfrac{\partial\left(\rho_g\,k_{rw}\right)}{\partial z}\left(\dfrac{\partial P_w}{\partial z} + \dfrac{\partial P_c}{\partial z} - \rho_g g\right) = I_g \end{cases} \qquad (3.16)$$

In Eq. (3.16), it is assumed that water is an incompressible fluid (i.e., ρ_w is constant) and the compressibility of pore space is negligible (i.e., $\partial\phi/\partial P \approx 0$ in Eq. (2.20)). Eq. (3.16) consists of two equations and two independent variables, P_w and S_w. The partial differential equations in Eq. (3.16) can be solved by using analytical or numerical methods when the values of independent variables are known at $t = 0$ (i.e., initial condition) and at the boundaries in each dimension (i.e., boundary condition). The expansion of Eqs. (3.11) and (3.15) in x- and y-direction, is similar to the results presented in Eq. (3.16), except that the term for hydrostatic gradient ($\rho_w g$) would be deleted in these two directions.

3.2 Application of TOUGH2 program

Although, several analytical solutions exist in the literature for the system of non-linear partial differential equations (e.g., Eq. (3.16)), most of them are restricted to 1D, to the certain boundary conditions, and to the assumption of a homogeneous porous media. For instance, McWhorter and Sunada (1990) developed a semi-analytical solution for two-phase flow equation of horizontal flow through a homogeneous porous medium. This analytical solution can be used for sensitivity analysis, and qualitative discussion about time scales and length scales of two-phase flow, in which the capillary pressure is significant.

Despite the application of analytical solutions, most of the partial differential equations can be solved numerically without applying the simplifying conditions. For instance, heterogeneity of characteristic properties of the porous media (e.g., heterogeneity in permeability values) can be implemented in numerical models. The steps involved in developing a numerical model are summarized in Fig. 3.1.
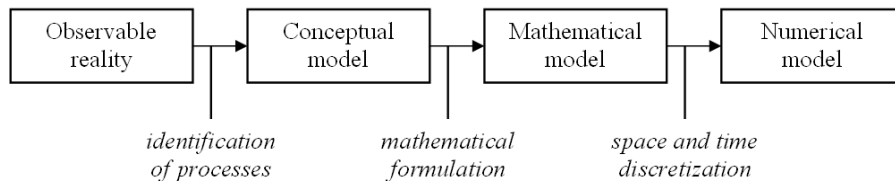
Fig. 3.1: Steps in development of a numerical model (Juanes, 2003).

Since this work concentrates on gas injection into heterogeneous porous media, the TOUGH2 program is used as a numerical model to simulate the two-phase flow occurred in direct gas injection. The TOUGH2 program was released originally by K. Pruess (1991) to model the multi-dimensional fluid flow and heat flow in a multi-phase, multi-component system. The accuracy of TOUGH2 program has been tested and verified with respect to different analytical and numerical solutions, and the results of laboratory experiments (Pruess et al., 1999). Additional to the TOUGH2 core program, several supplementary programs have been written to facilitate the TOUGH2 application (e.g., the programs that create the initial and boundary conditions). The TOUGH2 program has the modular source code written in FORTRAN that facilitates the user-defined changes in different modules.

The TOUGH2 program consists of nine different fluid-property modules, which are addressed by EOS (equation of state). Table 3.1 listed all the fluid-property modules of TOUGH2 program. At the time, only one module can be used in TOUGH2 execution.

All the modules in Table 3.1, except EOS2, EOS4 and EOS9, have capability to simulate the constant-temperature (i.e., isothermal) condition (Pruess et al. 1999). EOS3 is used in this work to solve the system of non-linear partial differential equations presented in Eq. (3.11) and Eq. (3.15), because it considers a gas-water system and calculates the fluid properties of this two-phase flow system.

Table 3.1: Fluid-property modules applied in execution of TOUGH2 program (Pruess et al., 1999).

Module	Capable phases
EOS1	water, water with tracer
EOS2	water, CO_2
EOS3	water, air
EOS4	water, air, with vapor pressure lowering
EOS5	water, hydrogen
EOS7	water, brine, air
EOS7R	water, brine, air, parent-daughter radionuclides
EOS8	water, dead oil, non-condensible gas
EOS9	variably-saturated isothermal flow according to Richards' equation
EWASG	water, salt (NaCl), non-condensible gas (includes precipitation and dissolution, with porosity and permeability change; optional treatment of vapor pressure lowering effects)

Compile the TOUGH2 program
To run the TOUGH2 program, the source files (e.g., t2cg2.f, meshm.f, eos3.f, ma28.f, t2f.f, and t2solv.f, and one EOS module) must be linked and compiled together. When TOUGH2 program runs, an executable file is created in Visual Fortran compiler (Compaq Visual Fortran Professional 6.5, Compaq Computer Corporation, 2000) that links all the source files. The executable file can be compiled at Command Prompt by addressing the valid names of input and output files.

3.2.1   Numerical solution of flow equations in TOUGH2 program

TOUGH2 program solves the integral form of mass continuity and energy balance equations, in which the fluid advection flow is described by generalized Darcy's law and diffusive transport can be exist in all phases. The Integral Finite Difference method (IFDM) is utilized in TOUGH2 program, which avoids referring to a global coordinate system and offers the advantage of being applicable for regular or irregular discretization in 1D, 2D, and 3D (Pruess et al., 1999).

In TOUGH2 simulation, the thermodynamic variables and thermophysical parameters are called primary and secondary variables, respectively. The primary variables are determined for all grid blocks at the specific time by the system of partial differential equation, whereas the secondary variables are calculated by EOS module using the primary variables.

During the execution, TOUGH2 creates two large arrays that hold the primary and secondary variables, individually. Fig. 3.2 represents the iterative algorithm in TOUGH2 program to calculate the primary and secondary variables.
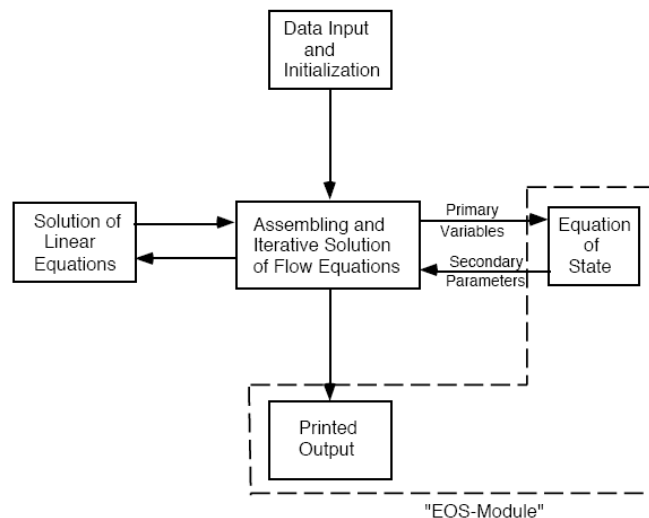
Fig. 3.2: The iterative algorithm in TOUGH2 program (Pruess et al., 1999).

The discretization of fluid flow and energy-balance equations, results in a set of coupled nonlinear equations, in which the primary variables (e.g., saturation and pressure) become time-dependent properties. TOUGH2 uses the Newton-Raphson method to handle the nonlinearity in the equation system. The time is discretized fully implicitly by the first-order backward scheme (i.e., $t_{k+1} = t_k + \Delta t$). The automatic time step adjustment can be used in TOUGH2 for efficient simulation, which increases or decreases the time step depending on the convergence of the iteration process during one simulation run.

TOUGH2 handles the input data by using different data files (e.g., INPUT, MESH, GENER, and SAVE files) that use a keyword architecture with the fixed 80 characters in a line. As the INPUT and MESH files are the most important files, they are introduced briefly in the next sections.

3.2.2 INPUT file

The INPUT file can have an arbitrary valid name. The INPUT file is an ASCII data file that provides the hydrogeologic parameters (e.g., porosity, absolute permeability), and computational parameters (e.g., criterion of time- and space-discretization). In addition, the INPUT file provides the values of initial and boundary conditions, and the sink/source (i.e., injection and production) criteria. The data in INPUT file are provided in different blocks, in which every five-character keyword (in place 1-5) specifies a block. Table 3.2 presents a list of the blocks used in INPUT file.

Table 3.2: The blocks used in INPUT file (Pruess et al., 1999).

Block keyword	Function
TITLE	the first record; title for the simulation problem
MESHM	optional; internal grid generation through MESHMaker
ROCKS	specifying hydrogeologic parameters of rock domains
MULTI	optional; number of fluid components and balance equations per grid block; applicable only for certain EOS-modules
SELEC	supply thermophysical property data with certain EOS-modules
START	optional; data record for more flexible initialization
PARAM	computational parameters; time step and convergence parameters
DIFFU	diffusivities mass components
FOFT	optional; grid blocks for which time series data are desired
COFT	optional; connections for which time series data are desired
GOFT	optional; sinks/sources for which time series data are desired
RPCAP	optional; parameters for relative permeability and capillary pressure functions
TIMES	optional; specification of times for generating printout
ELEME	list of grid blocks
CONNE	list of flow connections between grid blocks
GENER	optional; list of mass or heat sinks and sources
INDOM	optional; initial conditions for specific rock domains
INCON	optional; initial conditions for specific grid blocks
NOVER	optional; suppresses the version numbers and executed dates of TOUGH2 run
ENDCY	the last record; close the TOUGH2 input file and initiate the simulation
ENDFI	alternative to ENDCY for closing a TOUGH2 input file; while causes flow simulation to be skipped; useful if only mesh generation is desired

Some blocks (e.g., ROCKS, ELEME, and CONNE), which provide the geological properties of the model, may have a variable number of records. While, other blocks (e.g., MULTI, START, and PARAM) have specified numbers of variables that should be specified for TOUGH2 simulation. ELEME, CONNE, GENER, and INCON blocks can be omitted in INPUT file and provided as separate disk files, but with the same format that they have as a part of INPUT file. Even though, specifying the GENER and INCON data block in the input file offers more conveniences, especially when a new simulation run is initiated. Because, the changes in initial condition or sink/source data overwrite the INCON and GENER files that exist from previous simulation run. All the data should be provided in international system of units (SI) (meter, second and kilograms), and the corresponding derived units (e.g., Newton and Pascal). The

specification of ROCK, and INCON blocks are explained in this section. For detailed description of the INPUT file, one should refer to the TOUGH2 manual.

ROCKS block
The ROCKS block is used to introduce the parameters of up to 27 different rock types (rock domains). In the ROCKS block, each rock type is addressed by a material name that consists of five characters. The values of rock properties (e.g., grain density, porosity, the absolute permeability along the principal directions, heat conductivity, compressibility, Klinkenberg parameter) are specified for each rock type. In addition, the integer parameters that specify the type of relative permeability and capillary pressure functions (see section 2.5) should be determined in the ROCKS block.

INCON block
INCON block supplies the values of independent variables (i.e., the primary variables defined specifically for each EOS) for all grid blocks for initiation the simulation run. The name and the corresponding porosity value of the grid blocks are listed in INCON block. In most cases, the simulation is performed in several subsequent runs that make it necessary to use the result of previous run as the initial condition for the next run. That is possible by using the data stored in SAVE file after each simulation run. The contents of the SAVE file can be copied in the INCON block of the INPUT file for the next simulation run.

3.2.3   MESH file
The MESH file describes the geometry of the grid blocks and consists of two parts: ELEME and CONNE blocks. The ELEME block lists the number of grid blocks in principal directions (e.g., x, y, and z in Cartesian system), and the size and volume of each grid block. The CONNE block specifies the connections between the grid blocks.
The MESH file can be generated by the supplementary programs, or by using the Mesh-maker module of the TOUGH2 program. The Mesh-maker module can create radial and Cartesian grids, or grids of fractured media. If there is no ELEME, CONNE or MESHM blocks in INPUT file, TOUGH2 will automatically search for a disk file (i.e., MESH file) which one has to denote as MESH.DAT.
The type of boundary condition (e.g., Dirichlet or Neumann conditions) can also be defined within the MESH file. For example, grid volume equals to zero specify the Dirichlet (constant boundary condition), while Neumann conditions are specified by no connection between the grid blocks.

3.3   Implementation of simulation run
Running the simulation starts by compiling the executable TOUGH2 program, and giving the valid names and the addresses of the input and output files. Then, the computation starts by reading the geometry and the primary variables of the grid blocks. On the first time step, all the secondary variables of the corresponding EOS module are initialized by using the values supplied as initial condition in INCON block. For the next time step, the primary variables are calculated by solving the fluid flow equations (e.g., Eqs. (3.11) to (3.15) for the gas-water system). The flow equations are solved by Newton-Raphson iteration method. The sequence of iteration process is controlled by several parameters (e.g., KCYC (time step counter), ITER (iteration

counter), and KON (convergence flag)), which are defined in PARAM block of INPUT file. If convergence is achieved (i.e., KON = 2), the primary variables are being updated. Otherwise, the control shifts to LINEQ, which applies the linear equation solvers which was selected by the user. In other words, the program proceeds to the next iteration procedure for KON = 1, or to the next time step for KON = 2.

The time step is reduced and the calculation is repeated, if a failure occurs in computation of secondary variables, solving the linear equations, or achieving convergence criterion within the given maximum number of iterations.

The compilation continues until one of the termination criteria is reached (e.g., the specified simulation time, or the total number of time steps). When the simulation run is terminated, then the results will be stored in the OUTPUT file. If convergence is achieved on first iteration (i.e., ITER = 1) for 10 consecutive time steps, the process terminates, because the changes in primary variables are negligible. Therefore, it is considered to achieve the steady state condition. But, sometimes the unrealistic change or unrealistic values may create the convergence on ITER=1. Therefore, it is necessary to follow the results in OUTPUT file to find if there is any problem in calculations and iteration scheme. The convergence problem is one of the most critical problems in TOUGH2 simulation that cannot be handled easily, unless the OUTPUT file is investigated.

3.4 Heterogeneous parameter fields

As mentioned before, analytical solutions are restricted to homogeneous porous media. This restriction is crucial for field scale applications, because the gas flow patterns are determined by the heterogeneous sediments with heterogeneity in permeability and capillary pressure fields.

The results of heterogeneous simulation by TOUGH2 in literature reveal that the TOUGH2 program gives reasonable results also for strong heterogeneous fields, in which the standard deviation is given by the mean values of the stochastic field. Even though, the processing time (CPU time) increases and the convergence problems become more difficult.

Formally, the macroscopic heterogeneity can be implemented by defining different rock types, which the grid blocks are referred to. The heterogeneity within one rock type can be implemented by the permeability modifiers. The permeability modifiers are a set of random values that can be generated by geostatistical software (e.g., GSLIB (Deutsch & Journel, 1998) or Hydro-gen program (Bellin and Rubin, 1996)). Therefore, random and conditioned stochastic fields can be applied using the permeability-modifier option.

The permeability modifier of grid block n is defined by Eq. (3.17) in units of absolute permeability of the porous medium.

$$\zeta_n = \frac{k_n^{'}}{k_n} \tag{3.17}$$

where,
ζ_n = permeability modifier of grid block n, [-]
$k_n^{'}$ = modified permeability value of grid block n, [L^2]
k_n = absolute permeability value of grid block n, [L^2]

The modified permeability of each grid block is calculated via Eq. (3.17), while the absolute permeability of a certain rock type is provided in INPUT file. The permeability modifiers can be provided within the MESH file (position 41-50) as external data, or can be generated by TOUGH2 program internally. To activate the permeability-modifier option, a dummy rock domain with the name SEED must be defined in ROCKS block. The presence of domain SEED will switch on permeability-modifier option. In addition, the data in the SEED domain specifies if the modifiers are provided in the MESH file or they should be generated internally by TOUGH2.

If the user provides a stochastic permeability field in TOUGH2 simulation, the stochastic capillary pressure field can be internally generated by Leverett scaling (Leverett, 1941). This dependency is obvious, since the permeability varies with the square of the pore radius (see Hagen-Poiseuille law in Eq. (2.7)), and the capillary pressure is inversely proportional to the pore radius (see Laplace-Young equation in Eq. (2.2)). Leverett (1941) suggested a semi-empirical approach to relate the changes of permeability values to the capillary pressure values. Eq. (3.18) gives the Leverett J-function, $J(S_{wet})$, which is a function of wetting-phase saturation (Leverett, 1941). In his approach, the dimensionless function, which is called Leverett J-function, represents a specific curve when the dimensionless values of $J(S_{wet})$ (Eq. (3.18)) is plotted versus the saturation of wetting phase for several samples of one rock type (Bear, 1989). It means that different rock type (or different soil textures) can be characterized by differences in the curves of their J-functions.

$$J\left(S_{wet}\right) = \frac{P_c}{\sigma_{wet,nwet}\cos\theta}\sqrt{\frac{k}{\phi}} \tag{3.18}$$

Therefore, the Leverett J-function can be used to extrapolating the changes in capillary pressure values for a known rock type by using the permeability, porosity and wetting properties this rock type.

TOUGH2 uses Leverett J-function (Leverett, 1941) to apply the effect of heterogeneity in capillary pressure based on the heterogeneity in permeability values. In one rock type (i.e., $\sigma_{wet,nwet}$, θ, and ϕ remain constant) the permeability and capillary pressure are dependent according to Eq. (3.19):

$$P_{c,n}^{'} = \frac{P_{c,n}}{\sqrt{\varsigma_n}} \tag{3.19}$$

where,
$P_{c,n}{'}$ = modified capillary pressure of grid block n, [M L^{-1} T^{-2}]
$P_{c,n}$ = capillary pressure of grid block n, [M L^{-1} T^{-2}]

Eq. (3.20) shows the relationship between the absolute and modified permeability in 2D cases. In this equation, the modified permeability of grid block n, is defined in x- and y-direction by $k_n^{'}(x)$ and $k_n^{'}(y)$, respectively.

$$k_n^{'}\left(x\right) = k_n\left(x\right)\varsigma_n$$
$$k_n^{'}\left(y\right) = k_n\left(y\right)\varsigma_n \tag{3.20}$$

In 3D cases, the absolute permeability in z-direction is also multiplied by the permeability modifier provided in MESH file. However, the heterogeneity in vertical direction is totally different from the heterogeneity in horizontal direction, but

TOUGH2 can read just one set of permeability modifier. It is the disadvantage of applying the heterogeneity by using the modifiers in TOUGH2. The source code of TOUGH2 program should be changed, if it is interested to apply independent modifiers in z-direction.

4   Gas Injection in Bench-scale Experiment

Many authors conducted bench-scale experiments of point-like gas injection to investigate the local gas flow pattern (e.g., Clayton, 1998; Brooks et al., 1999; Lazik et al., 2002; Ji et al., 1993; Semer et al., 1998; Peterson et al., 1999; Reddy and Adams, 2001; Selker et al., 2006; Geistlinger et al., 2006). They used their observations to estimate the average flow properties (e.g., the gas volume inside the model), or the local properties (e.g., the heterogeneous gas distribution). The focus of this chapter is mainly on modeling the bench-scale experiments that Krauss (2007) performed in his work. At first, a brief overview of Krauss's experiments is presented, and then the simulation results of gas injection are discussed in detail.

4.1   Bench-scale experiments

4.1.1   Experimental Set-up

Krauss (2007) used a 2D Plexiglas flow-cell with inner dimension of $L_x \times L_y \times L_z = 40 \times 1.2 \times 45$ cm to conduct the laboratory experiments. The images of phase displacement at the surface of the flow-cell were considered as the displacement occurred inside the flow-cell. Plexiglas was used to minimize the influence of the flow-cell material (e.g., the effect of light transferring, and the difference in wettability behavior of the Plexiglas and GBS). In laboratory experiments, each class of GBS is characterized by a size interval (e.g., 0.25 – 0.5 mm). Krauss (2007) used three different classes of glass beads (Carl Roth GmbH + Co. KG): 0.25 – 0.5 mm, 0.75 – 1.0 mm, and 2.0 – 2.2 mm, which are named as 0.5 mm-GBS, 1 mm-GBS and 2 mm-GBS, respectively.

The packing procedure and the stability of the sediment pack during the experiments affect the gas flow pattern (Ji et. al., 1993; Brooks et al., 1999; Glass et al., 2000; Selker et al., 2001; Geistlinger et al., 2006). In Krauss's experiments, wet glass beads were poured gradually in the flow-cell up to the height of 35 cm. In each step of pouring, mechanical pulses were applied to build a tight packing. The glass beads were covered by 6 cm of lead spheres ($d_{lead} = 3$ mm, $\rho_{lead} = 11.2$ g/cm³) as a litho-static layer to prevent the grain re-arrangement and achieve a stable pack. Fig. 4.1 shows the experimental set-up that Krauss (2007) used to perform the bench-scale experiments.

The bench-scale experiment was equipped with two measuring systems: the optical system, and the gravimetrical system. For the optical system, the light reflection technique was used to record the gas distribution and gas flow pattern with respect to time. Krauss (2007) used an overflow system to maintain a constant water level and applied a constant hydrostatic potential. At the same time, the gravimetrical system measured the mass of water displaced by the injected gas.

By considering the flow-cell as a volumetric system, the volume of displaced water can be considered equal to the injected gas volume. Eq. (4.1) shows the calculation:

$$V_g(t) = \Delta V_w(t) = \frac{\Delta m_w(t)}{\rho_w} = \frac{m_w(t) - m_w(t=0)}{\rho_w} \tag{4.1}$$

where,

m_w = mass of water, [M]
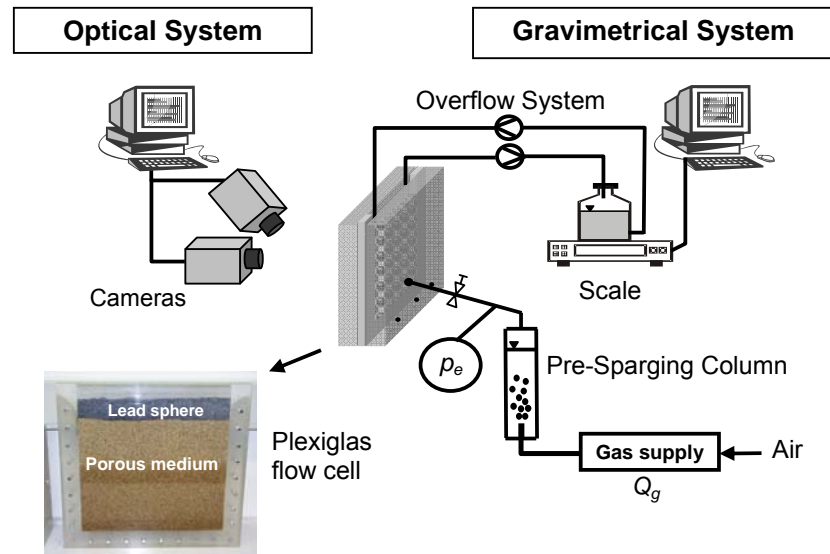
Fig. 4.1: Experimental set-up for bench-scale experiments (Krauss, 2007).

4.1.2 Gas injection into the flow-cell

The injection pressure was measured at the injection point by a pressure transducer. The injection pressure should overcome the sum of the hydrostatic pressure of water column above the injection point, and the capillary pressure at the injection point. Therefore, the experimental entry pressure would be the difference of the injection pressure and the hydrostatic pressure at the steady-state. During the injection processes, the entries pressure (P_e) and the gas volume (V_g in Eq. (4.1)) were measured with respect to time. The air was injected with a constant flow rate until the steady-state was reached. The steady-state was defined as a condition when entry pressure and volume of displaced water did not change. After reaching the steady-state, the injection rate was increased. The values of injection rates, entry pressure at the injection point and total gas volume at the steady-state are listed in Table 4.1 and Table 4.2 for 0.5 mm- and 1 mm-GBS, respectively.

Table 4.1: Steady-state values of injection rate, capillary pressure, and gas volume for injection process in 0.5 mm-GBS.

	Q_1	Q_2	Q_3	Q_4	Q_5	Q_6	Q_7	Q_8	Q_9	Q_{10}	Q_{11}
Injection rate (ml/min)	10	31	59	146	233	321	407	495	582	669	844
P_c (kpa)	1.2	1.9	2.3	3.4	4.9	6.0	6.8	8.1	9.9	11.6	15.8
V_g (cm^3)	17.7	22.4	29.1	50.2	66.5	77.4	88.8	98.9	108.0	114.0	136.0

Table 4.2: Steady-state values of injection rate, capillary pressure, and gas volume for injection process in 1 mm-GBS.

	Q_1	Q_2	Q_3	Q_4	Q_5	Q_6	Q_7	Q_8	Q_9
Injection rate (ml/min)	10	70	130	188	808	1377	1912	2417	2901
P_c (kpa)	4.4	4.4	4.5	4.5	4.7	5.1	5.5	5.9	6.3
V_g (cm^3)	18.3	22.9	27.9	32.1	66.0	93.3	110.3	122.9	134.2

4.2   Results of image processing

4.2.1   Investigation of gas flow pattern

In section 2.2, the gas injection through 0.5 mm- and 1 mm-GBS that creates coherent flow were studied. The flow patterns at steady-state are shown in Fig. 4.2 for 0.5 mm- and 1 mm-GBS, in which the injection rate was $Q_g = 10$ ml/min. Both GBS show similar channelized flow pattern, while the number of channels in the 0.5 mm-GBS is smaller than those in the 1 mm-GBS. This difference is due to higher entry pressure in the 0.5 mm-GBS that resists developing the new channels. Even though, Krauss (2007) classified the flow pattern in 1 mm-GBS as coherent flow, but he reported the development of new channels and snap-off behavior in the early transient phase.

(a)   (b)

Fig. 4.2: Steady-state channelized flow pattern in: (a) 0.5 mm-GBS, and (b) 1mm-GBS, for $Q_g = 10$ ml/min (Krauss, 2007).

The image of incoherent flow that is developed in 2 mm-GBS for injection rate $Q_g = 10$ ml/min, is presented in Fig. 4.3. Fig. 4.3a represents the gas flow pattern at $t = 6000$ s when the quasi steady-state is established. The quasi steady-state refers to a condition when the injection process is developed for a long time but still some oscillations occur in measuring properties. The difference between two subsequent images ($\Delta t = 1$s), which are taken at the quasi steady-state, is shown in Fig. 4.3b. This figure represents the gas clusters developed in 1 s time interval, which is a proof of incoherent bubbly flow pattern.

(a)   (b)

Fig. 4.3: Gas flow pattern in 2 mm-GBS: (a) at quasi steady-state, (b) for difference of two subsequent images ($\Delta t = 1$ sec) in quasi steady-state (Krauss, 2007).

Fig. 4.4 shows the changes in entry pressure and gas volume for 0.5 mm-, 1 mm- and 2 mm-GBS, when gas is injected with Q_g = 10 ml/min. The plateau of the entry pressure indicates that the injection process has reached to the steady-state. For instance, the steady-state is established in 0.5 mm-GBS after 100 sec, when the entry pressure reaches its plateau in Fig. 4.4a. The entry pressure of the 1 mm-GBS shows some oscillations, which are numbered 1 - 4 in Fig. 4.4a. These oscillations can be interpreted as higher pressure needed to create new gas channels. Comparison of entry pressure and gas volume of 1 mm-GBS reveals that the oscillations in entry pressure are correlated to the step-like increase in gas volume (compare Fig. 4.4a and Fig. 4.4b for 1 mm-GBS). The steady-state is established in 1 mm-GBS after 2500 sec, which is much longer than the corresponding time in 0.5 mm-GBS. In conclusion, the transient time (i.e., the time before the steady-state is established) becomes significantly longer when the grain size increases. The random and strong oscillations of the entry pressure and gas volume of the 2 mm-GBS show that the gas injection through 2 mm-GBS did not create stable gas channels. The gas cluster shown in Fig. 4.3b confirms that the gas is transported by discontinuous gas clusters in 2 mm-GBS. Therefore, developing new gas bubbles and snap-off behavior of gas channels create the instability of the entry pressure.
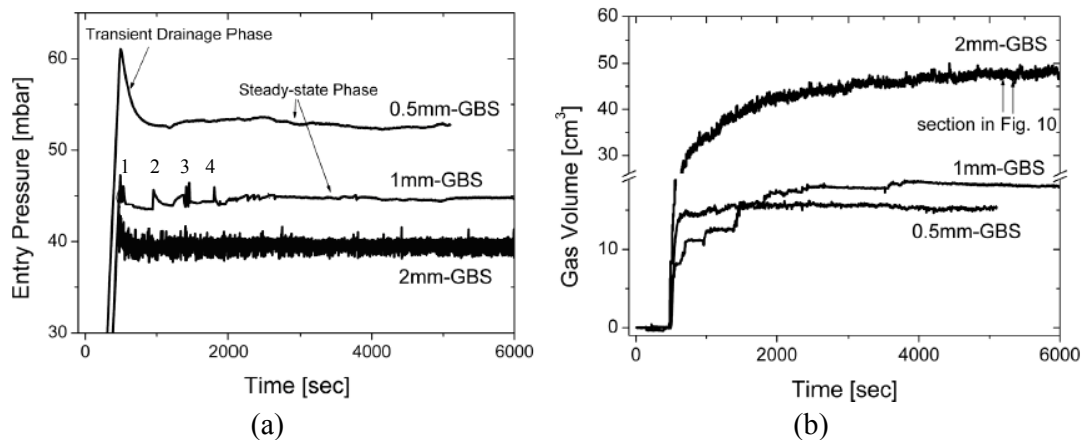
Fig. 4.4: Experimental measurement of: (a) entry pressure, and (b) gas volume, versus time in 0.5 mm-, 1 mm- and 2 mm-GBS for Q_g = 10 ml/min (Geistlinger et al., 2006).

Fig. 4.5 shows the measured entry pressure and the gas volume for the 1 mm-GBS for all injection rates listed in Table 4.2. According to Eq. (2.18), the critical flow rate for gas injection in 1 mm-GBS with mean radius of 0.21 mm (see Table 2.2) is equal to $Q_{critical}$ = 23.60 ml/min. The oscillations of the entry pressure observed for Q_g = 10 ml/min in Fig. 4.5 confirmed that the injection with Q_g < 23.60 ml/min cannot create stable gas channels. These oscillations were not observed for a higher injection rate (i.e., Q_g > 23.60 ml/min), because the higher injection rate applies higher pressure forces that develop stable channelized flow pattern. This observation confirms that the transition from incoherent to coherent flow is a rate-dependent phenomenon.

The transient time decreases (i.e., the steady-state is reached earlier) when injection rate increases (see the dashed lines in Fig. 4.5), because higher injection rate applies higher pressure forces (and therefore higher viscous forces) that establish stable channels during smaller time interval (see Eq. (2.8)).
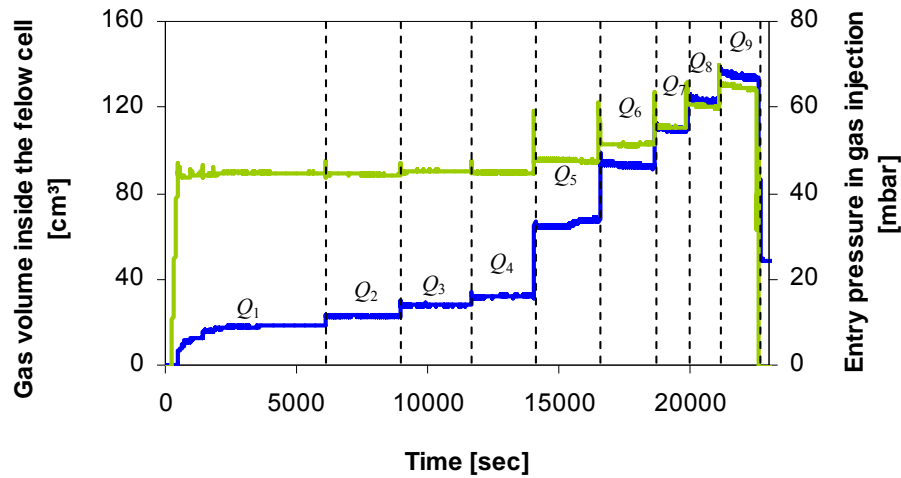
Fig. 4.5: Experimental measurement of entry pressure and gas volume versus time for stepwise gas injection in 1 mm-GBS (Krauss, 2007).

4.2.2 Investigation of gas injection into 1 mm-GBS

Gunner Krauss (2007) investigated the channelized flow pattern established in gas injection through 0.5 mm-GBS. Since the 1 mm-GBS shows a transition behavior from unstable to stable channelized flow at the smallest injection rate of 10 ml/min, this work focus to this interesting case. The images of gas flow pattern of 1 mm-GBS are presented in Fig. 4.6 when gas is injected with Q_g = 10 ml/min. Fig. 4.6a to Fig. 4.6d show the transient gas flow pattern at 3 s, 6 s, 11 s, 14 s, and 10 min, respectively. Fig. 4.6d to Fig. 4.6e show the flow pattern at breakthrough and steady-state for Q_g = 10 ml/min.
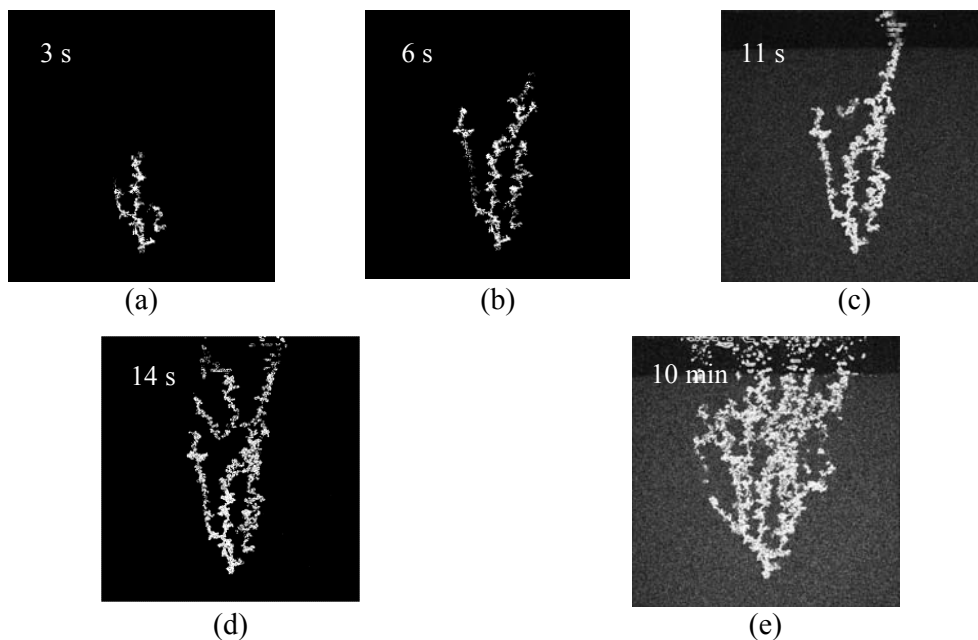
Fig. 4.6: Gas flow pattern in 1 mm-GBS at: (a) 3 s, (b) 6 s, (c) 11 s, (d) 14 s, (e) 10 min where injection rate is Q_g = 10ml/min (Krauss, 2007).

Comparing Fig. 4.6d and Fig. 4.6e reveals that new gas channels developed after breakthrough. The time between breakthrough and steady-state is identified in Fig. 4.4a, where the oscillations (peaks) in the entry pressure are labeled by 2 - 4.

Fig. 4.7 shows the breakthrough and the corresponding images of peak 2 - 4. Fig. 4.7a shows the gas distribution at breakthrough, where the gas-filled pores are shown in white. Fig. 4.7b to Fig. 4.7d represent the new channels developed at the corresponding pressure peaks. For example, Fig. 4.7b represents the new channels developed at pressure peak labeled (2) in Fig. 4.4a. In these figures and the following ones, the new channels are presented in white and refilled channels are presented in black. Fig. 4.7 indicates the changes of the channel lengths and the snap-off that breaks the pathways of gas channels. For instance, the circles in Fig. 4.7b show that the snap-off is occurred, when new gas channels are created to transport the injected gas. Similar behavior can be seen in Fig. 4.7c and Fig. 4.7d.

(a)   (b)

(c)   (d)
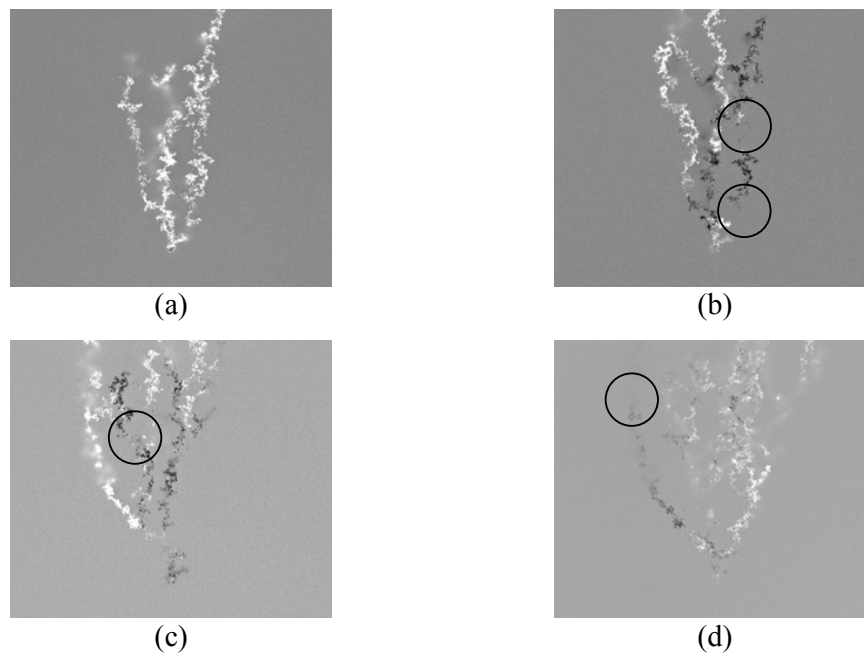
Fig. 4.7: Development of gas-filled channels in 1 mm-GBS for Q_g =10 ml/min. The images in (b) - (d) correspond to the pressure peaks labeled 2 - 4 in Fig. 4.4. The new and refilled channels are presented in white and black, respectively (Krauss, 2007).

The higher gas injection rate creates new channels and additional splits, however, some branches terminates at dead-ends, which may be refilled by water. The new established channels within the 1 mm-GBS are presented in Fig. 4.8a to Fig. 4.8d, when the injection rate is increased from Q_1 - Q_2, Q_3 - Q_4, Q_4 - Q_5, and Q_5 - Q_6, respectively. When all available capillaries inside the gas plume are filled by the gas, the influence zone is extended (e.g., Fig. 4.8d). In other words, the higher injection rate results in a wider gas plume and a larger radius of influence (ROI).

(a)   (b)

(c)   (d)
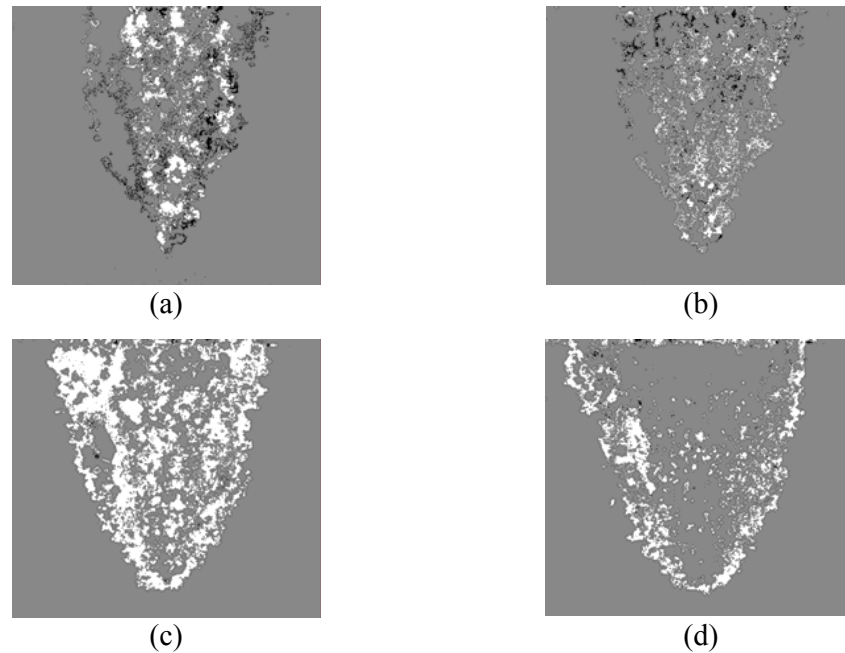
Fig. 4.8: Development of gas channels in 1 mm-GBS when injection rate increased. Images in (a) - (d) correspond to stepwise injection increase Q_1 - Q_2, Q_3 - Q_4, Q_4 - Q_5, and Q_5 - Q_6 (Krauss, 2007).

4.2.3 Investigation of parabolic gas plume within the 1 mm-GBS

Most bench-scale experiments confirmed the parabolic shape of the gas plume at moderate and high injection rates (Ji et al., 1993; Semer et al., 1998; Brooks et al., 1999; and Selker et al., 2007).

This section follows the phenomenological model that was developed by Selker et al. (2007). This model describes the local geometry of the gas plume, both at the near-source and far-source region, by simple algebraic relations when gas is injected into a saturated homogeneous porous medium. Fig. 4.9 shows the near- and far-source regions schematically.
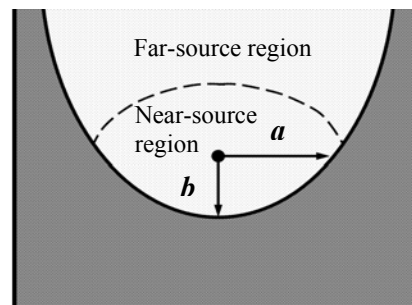
Fig. 4.9: Illustration of near- and far-source regions in direct gas injection (Selker et al., 2007).

Near-source region

In the near-source region, the velocity of gas injection is high and the pressure force dominates the capillary and buoyancy forces (see section 2.1). The buoyancy force acts only in the vertical direction and tends to transport the gas in upward direction.

Therefore, the downward resultant force (i.e., pressure force minus buoyancy force) is smaller than the horizontal resultant (i.e., pressure force). In other words, gas distributed in horizontal direction more than in vertical direction. Hence, the geometrical shape of the gas plume should be a horizontal ellipsoid.

For the near-source region, Selker et al. (2007) proposed a symmetrical ellipsoid in which the lateral extension (i.e., the horizontal width) is the major axis, which is twice the minor axis ($a = 2b$ in Fig. 4.9). Selker et al. (2007) proved the validity of this argument by using the experimental results performed by Semer et al. (1998).

Fig. 4.10 shows the images of steady-state gas distribution in 1 mm-GBS when the gas injection rate is increased stepwise (the injection rates are listed in Table 4.2).

The values of a and b are measured for these images and listed in Table 4.3. The values of b / a in Table 4.3 is approximately 2, and confirmed the argument by Selker et al. (2007) for near-source region. It should be mentioned that the values of a and b are not reported for injection rate $Q_g = 10$ ml/min, because with this injection rate distinct channels were established instead of a complete parabolic shape of gas plume.

(a) Q_2 (b) Q_3 (c) Q_4

(d) Q_5 (e) Q_6 (f) Q_7

(g) Q_8 (h) Q_9
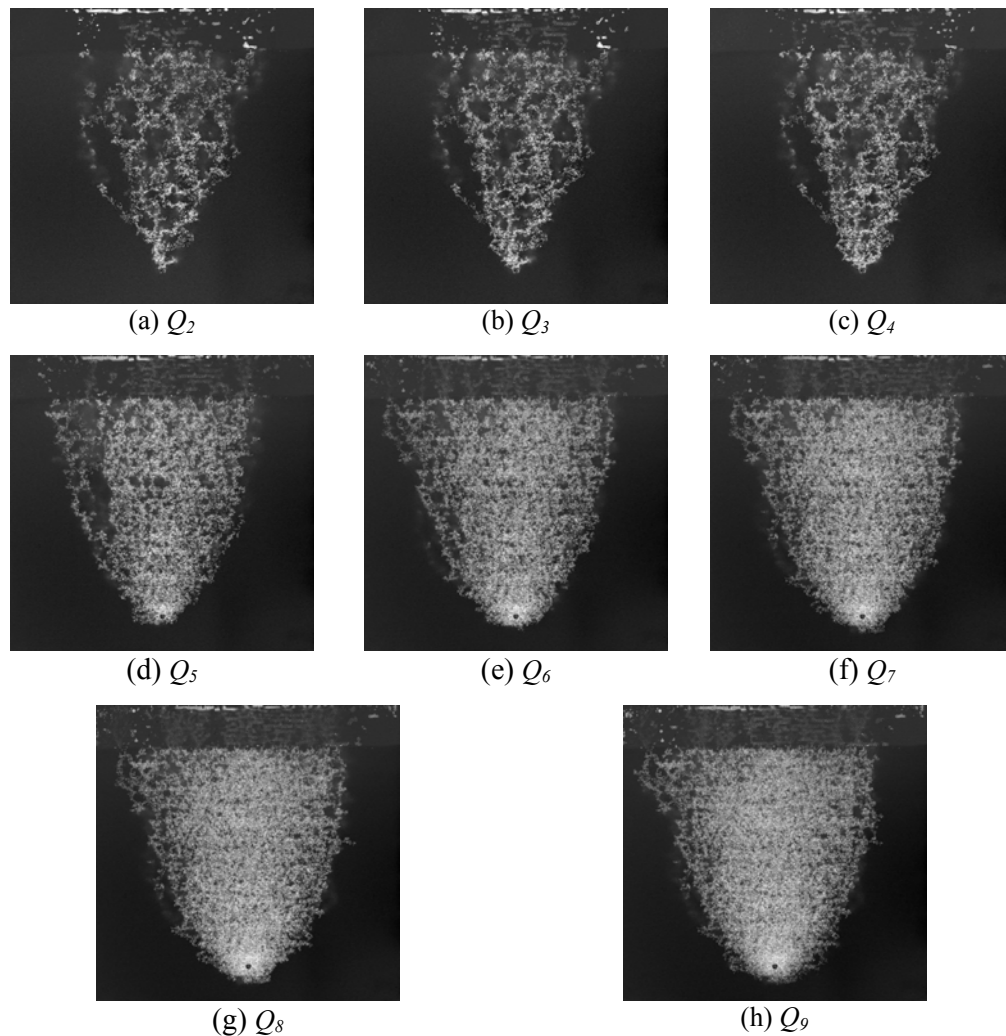
Fig. 4.10: Steady-state gas distribution through 1 mm-GBS for injection rates listed in Table 4.2 (Krauss, 2007).

Table 4.3: Geometric characterization of gas plumes in gas injection process through 1mm-GBS

Q_g (ml/min)	a (cm)	b (cm)	a / b
Q_5	1	0.5	2
Q_6	1.6	0.6	2.6
Q_7	1.7	1	1.7
Q_8	1.8	1.1	1.6
Q_9	2.55	1.2	2.1

Far-source region

In the far-source region, gas expands and the gas-filled area increases. Therefore, the gas velocity is decreased and buoyancy forces become significant with respect to pressure forces. Therefore, the gas channels are formed by competition between buoyancy force and capillary force (see section 2.1). For the far-source region, the parabolic shape of gas plumes is proposed to be a simple ensemble of the random lateral displacements of the distinct gas channels. Selker et al. (2007) predicted the variance of the Gaussian model increases with the square root of total displacement. Physically, that means the gas channels are created by the stochastic Brownian motion process, in which the horizontal travel distance depends on the square root of the travel time. Since the gas moves from pore to pore with an averaged velocity, the travel time can be expressed by the vertical distance divided by the averaged velocity. Finally, one obtains Selker's hypothesis: the horizontal extension of the gas-filled area increases linearly with the square root of the vertical distance that is measured from the injection point. Selker et al. (2007) investigated the gas distribution in the far-source region for high injection rates (e.g., Q_g = 640 ml/min – 5200 ml/min) and found reasonable agreement.

In order to prove Selker's stochastic hypothesis, the horizontal extension of gas-filled area was measured at difference distances from the injection point in Fig. 4.10. The measured vertical distance from the injection point is called the vertical extension. Fig. 4.11 presents the evaluation of flow pattern for injection rates Q_6 and Q_9, where the linear relationship between the horizontal extension and the square root of vertical extension confirms Selker's hypothesis, at least for modest and high injection rates.

Based on the stochastic hypothesis, only a dense capillary network can be described by the phenomenological model of the gas plume (i.e., the near-source region by an ellipsoid and the far-source region by a square-root relationship). For low flow rates or a sparse capillary network, this phenomenological model is questionable and a dynamic multi-phase modeling is required.

(a)   (b)
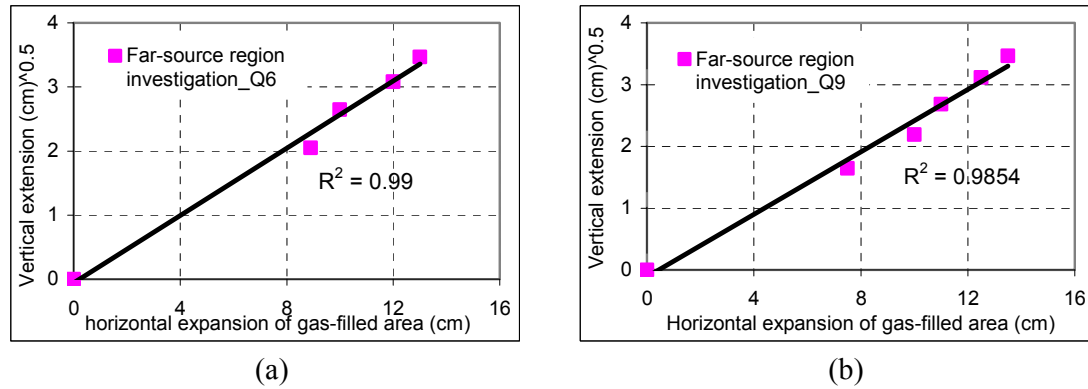
Fig. 4.11: The square root of vertical extension versus horizontal extension of gas-filled area in far-source region for: (a) Q_6 = 1377 ml/min, and (b) Q_9 = 2901 ml/min.

4.3 Continuum modeling using TOUGH2 program

As discussed in Chapter 2, the interplay of the forces (i.e., capillary, buoyancy and viscous forces) determines the gas flow pattern, geometry of gas-water interface, and the stability of gas channels. The TOUGH2 program, which was introduced in Chapter 3, is used to simulate the gas injection at REV-scale.

The TOUGH2 is not able to simulate the incoherent bubbly flow, which occurred for example in 2 mm-GBS, because it is developed based on the continuum assumption, and it uses the Darcy law to describe the multi-phase flow. Hence, only the gas injection in 0.5 mm- and 1 mm-GBS are considered in this section.

As stated in section 2.5, the van Genuchten-Mualem model (1980) and Brooks-Corey model (1966) are commonly used in the literature. Therefore, these two models are used in simulation of channelized coherent flow.

Relative permeability of non-wetting phase of van Genuchten-Mualem model

The relative permeability function of the wetting phase of the van Genuchten-Mualem model (1980) is presented in Eq. (2.36). In TOUGH2 program, the tortuosity factor of van Genuchten-Mualem model (1980) is considered equals to 0.5.

The corresponding relative permeability of non-wetting phase in TOUGH2 program is:

$$k_{r\,nw} = \begin{cases} 1 - k_{rw} & S_{nw\,r} = 0 \\ Eq.\,(2.43) \; with \; \lambda = 2 & S_{nw\,r} > 0 \end{cases} \tag{4.2}$$

The summation of the relative permeability of all phases is always less than unity due to the interference among the phases (Honarpour, 1986). It means that, Eq. (4.2) calculates the relative permeability of non-wetting phase much higher than the actual values when $S_{nw\,r} = 0$. In this work, Eq. (4.3) is used instead of the original function presented in Eq. (4.2).

$$k_{r\,nw} = \sqrt{1 - S_e} \left[1 - S_e^{1/m} \right]^{2m} \qquad S_{nwr} \geq 0 \tag{4.3}$$

Brooks-Corey model

The Brooks-Corey model (1966) is not implemented in original version of TOUGH2 program. Therefore, the source code of TOUGH2 program was changed to implement the Brooks-Corey model (1966). Considering the entry pressure in Brooks-Corey model may create numerical problems in calculation of derivatives close to the full saturation condition. But in TOUGH2 program, a minimum saturation is applied as a cut-off to avoid the full saturation limit.

Parameters of TOUGH2 simulation

Krauss (2007) reported the experimental values of porosity, absolute permeability, and entry pressure of 0.5 mm- and 1 mm-GBS. These values were reported in Chapter 2, but they are summarized and listed in Table 2.3. Krauss (2007) reported the variance of permeability values, since he measured the permeability of the GBS in several experiments.

Table 4.4: Experimental parameters of 0.5 mm- and 1 mm-GBS.

	0.5 mm-GBS	1 mm-GBS
Porosity (%)	0.36	0.39
k_{exp} (m^2)	$9.23 \pm 0.36 \times 10^{-11}$	$5.50 \pm 0.14 \times 10^{-10}$
P_e (Pa)	1210	850

The log-normal distribution of pore radii in 0.5 mm- and 1 mm-GBS were derived in section 2.4.2 by using the experimental properties. The minimum and maximum pore radii of different GBS were also calculated using the experimental characteristics and reported in Table 2.2 for different GBS. The capillary pressure-saturation relationship was derived depending on the pore size distribution, and maximum and minimum pore radii (see section 2.5.1). Kosugi (1996) derived an analytical expression for the capillary pressure-saturation relationship based on a log-normal pore size distribution. This capillary pressure-saturation relationship was calibrated by the experimental entry pressure. Since the Kosugi-relationship cannot be implemented in the TOUGH2 program, the capillary pressure curve in van Genuchten-Mualem and Brooks-Corey models were fitted to the calibrated Kosugi-relationship.

The parameters of capillary pressure-saturation relationship (e.g., α_p and n in Eq. (2.36)) of these two models (van Genuchten-Mualem and Brooks-Corey model) are estimated by curve fitting shown in Fig. 2.13 and summarized in Table 4.5.

The parameters of the relative permeability functions (e.g., α_p and m in Eq. (2.38)) were considered equal to the corresponding parameters of capillary pressure functions as a first estimation, and then modified during the simulation work (for details see Ho and Webb, 2006). Table 4.5 represents the modified parameters of relative permeability functions of van Genuchten-Mualem and Brooks-Corey models used in simulation of 0.5 mm- and 1 mm-GBS.

The simulation of this work has no degree of freedom to estimate the properties, since all the parameters required in TOUGH2 simulation were obtained or estimated from the experimental properties.

Table 4.5: Parameters of van-Genuchten and Brooks-Corey models for 0.5 mm- and 1 mm-GBS.

Parameter	van Genuchten-Mualem model		Brooks-Corey model	
	0.5 mm-GBS	1 mm-GBS	0.5 mm-GBS	1 mm-GBS
α_p (m^{-1})	7	10.5	8.2	12.3
n in Eq. (2.36)	10	9.2	-	-
m in Eq. (4.3)	0.9	0.95	-	-
λ in Eq. (2.41)	-	-	6.514	5.5
λ in Eq. (2.42)	-	-	1.6	3
S_{wr}	0.01	0.01	0.01	0.01
$S_m = 1 - S_{nwr}$	1.0	1.0	1.0	1.0

4.3.1 Homogeneous simulation of 0.5 mm-GBS

The cell size of TOUGH2 simulation was $l_x \times l_y \times l_z = 1.0 \times 1.0 \times 1.0$ cm. Applying the capillary-gravity equilibrium yields the initial condition. For gas injection, the following conditions are assumed: no-flow boundary condition at the bottom, Dirichlet boundary condition at the top, the left and the right side were assumed. Applying Dirichlet boundary conditions at the left and right side allows that water can flow through the sides and prevents an increasing water table during the gas injection.

Fig. 4.12 shows the experimental images and the theoretical results for the gas distribution at steady-state when injection rates are equal to 10, 146 and 844 ml/min. The theoretical results were visualized by Tecplot (Tecplot 360, Tecplot, Inc., 2009).

As can be seen from Fig. 4.12 (the experimental flow pattern in the left column), few channels are established with $Q_g = 10$ ml/min, while the theoretical gas distribution is uniform over the whole gas plume.

The higher gas injection rate creates a dense channel network, which results in uniform gas distribution. Therefore, the simulation can represent the theoretical gas distribution with higher degree of prediction ability for higher injection rates (e.g., $Q_g = 844$ ml/min).

In conclusion, the TOUGH2 program can represent the average properties of the gas flow pattern (e.g., the average values of gas saturation, the geometry of gas flow pattern, and gas-water interface), because it was developed based on the continuum assumptions, which consider the average properties over an REV.

Comparing the 2D visualization of the theoretical results (Fig. 4.12) reveals that the Brooks-Corey model creates a narrow gas plume (right column of Fig. 4.12), which describes the experimental gas plume significantly better than the van Genuchten-Mualem model (middle column of Fig. 4.12). For all injection rates presented in Fig. 4.12, the van Genuchten-Mualem model creates a too wide gas plume. The differences between these two models will be investigated in more details in the following. But before that, the prediction ability of TOUGH2 simulation is investigated.
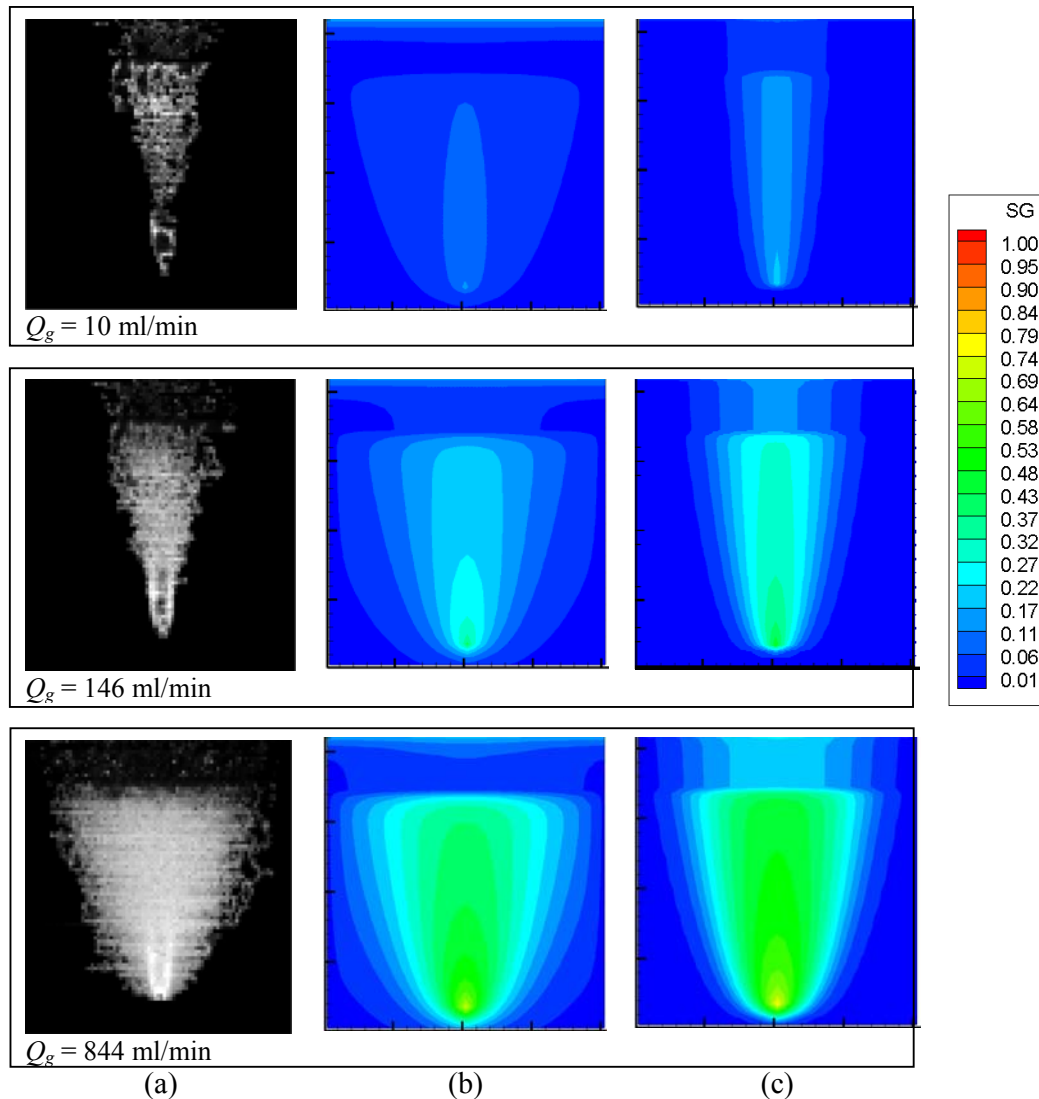
Fig. 4.12: 2D visualization of gas flow pattern in 0.5 mm-GBS for Q_g = 10, 146 and 844 ml/min: (a) bench-scale experiments by Krauss (2007), (b) TOUGH2 simulation using van Genuchten-Mualem model, and (c) TOUGH2 simulation using Brooks-Corey model.

Fig. 4.13 shows the comparison between the experimental gas volumes and theoretical values. The measurement of experimental gas volume by the gravimetrical method was described in section 4.1.2 (see Eq. (4.1)). The theoretical gas volumes were calculated by integration of gas saturation over the whole model. The relative error calculates the difference between the experimental and theoretical gas volumes with respect to the experimental one. The relative errors of theoretical gas volumes are represented in Fig. 4.13 (left axes).

It can be concluded that the continuum model predicts accurately the average gas volume for the applied injection rates, where a dense capillary network has been established. Although, the theoretical values overestimate the gas volume for low injection rates (e.g., the relative error increase up to 30 % for Q_g = 31 ml/min). This

overestimation is due to the fact that a continuum model cannot describe the single gas channels. A continuum model always yields a parabolic gas plume (see Fig. 4.12) that overestimate the gas saturation.

(a)   (b)
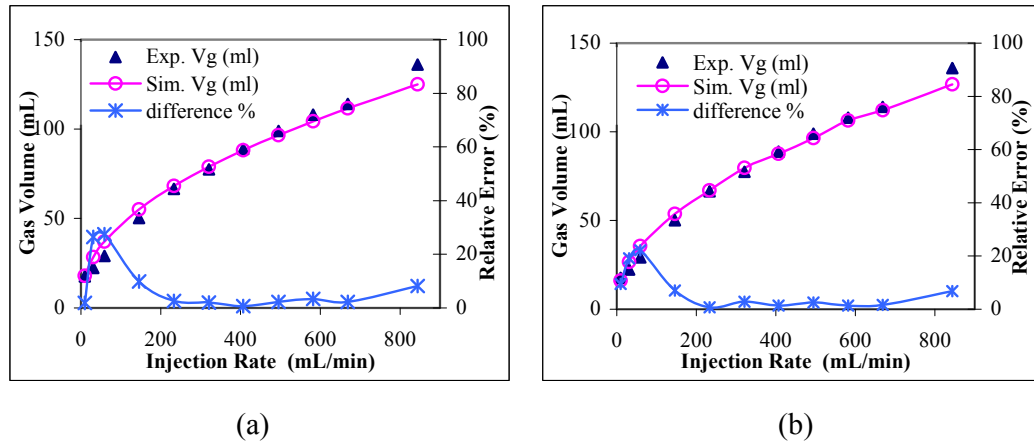
Fig. 4.13: Comparison of experimental and theoretical gas volume versus injection rate in 0.5 mm-GBS: (a) van Genuchten-Mualem model, (b) Brooks-Corey model.

It is surprising that the continuum model TOUGH2 has the same prediction ability for both relationships. However, the Brooks-Corey model is superior to the van Genuchten-Mualem model, since it yields a narrower gas plume that describes better the bench-scale experiments (Fig. 4.12).

Fig. 4.14 shows the 3D gas distribution in correspondence to Fig. 4.12. The 3D-gas distributions in Fig. 4.14 are obtained by Mathematica software (version 7.0, Wolfram Research, Inc., Champaign, IL, 2008).These 3D visualizations show that Brooks-Corey model not only creates the narrower gas plume, but also represents the sharp transition in gas saturation (i.e., an abrupt change in gas saturation between saturated and unsaturated zones). In contrast, the gas distribution of the van Genuchten-Mualem model shows a too large and too smooth extension.

In conclusion, the Brooks-Corey model is superior to the van Genuchten-Mualem model, since it gives the key features of the experimental gas distribution (i.e., the sharp gas-water interface at the boundary of gas plume).

The Brooks-Corey model is able to create this sharp interface, because it takes into account the existence of a finite entry pressure (i.e., existence of an upper maximum radius in pore size distribution, see section 2.5). In opposite, the van Genuchten model is based on the unphysical assumption of an infinite small entry pressure (infinite large pore radius).
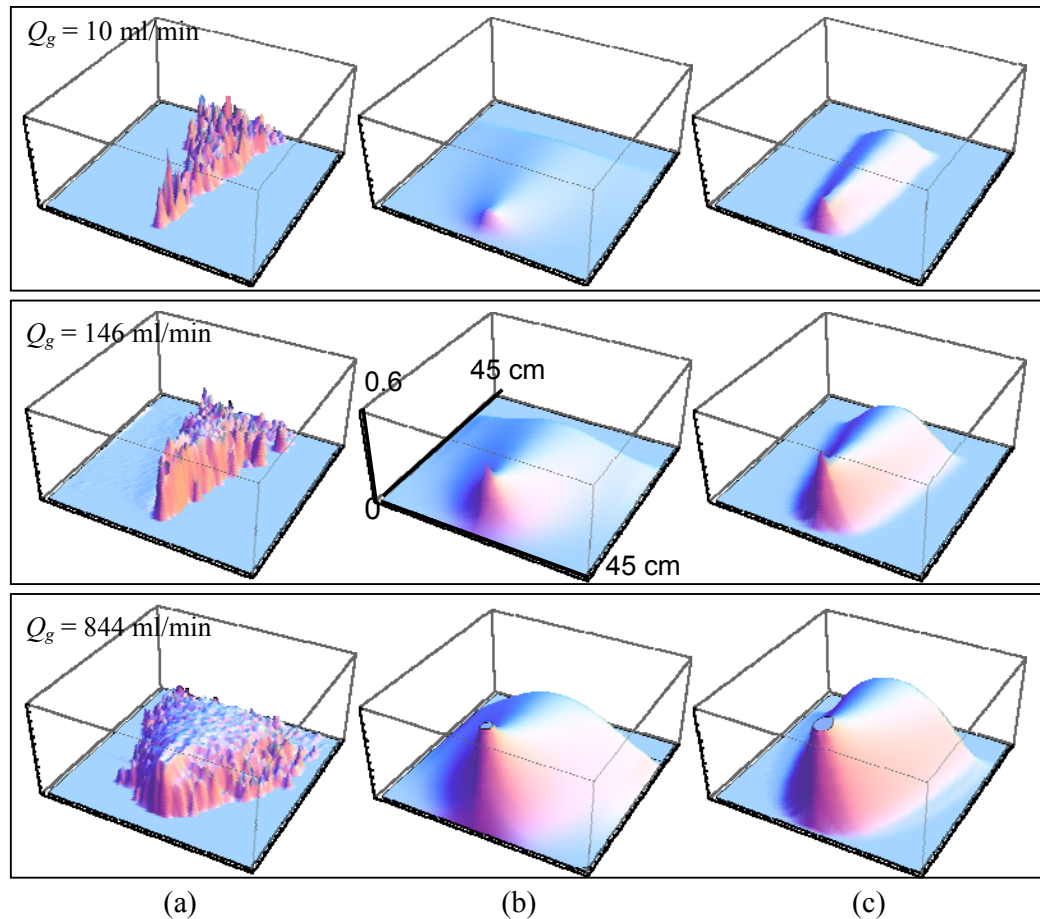
Fig. 4.14: 3D visualization of gas distribution in 0.5 mm-GBS for Q_g = 10, 146 and 844 ml/min: (a) bench-scale experiments by Krauss (2007), (b) TOUGH2 simulation using van Genuchten-Mualem model, and (c) TOUGH2 simulation using Brooks-Corey model.

In summary, it can be concluded that the continuum model gives reasonable agreement between the theoretical and experimental results. For the geometric shape the van Genuchten model gives a too wide distribution, due to its unphysical assumption of an infinite small entry pressure. The Brooks-Corey model fits the experimental shapes reasonable well. As discussed in section 4.2.1, the 1 mm-GBS shows some unstable behavior for the smallest flow rate of 10 mL/min. However, for larger flow rates the flow pattern was always stable coherent flow. Therefore, it is interesting to apply the continuum approach and examine to which extent the continuum model can explain the experimental results of the 1mm-GBS, especially at higher flow rates.

4.3.2   Homogeneous simulation of 1 mm-GBS

All the experimental values used in the simulation of 1 mm-GBS are listed in Table 2.3 and Table 4.5. The initial and boundary conditions, and the cell size were the same as considered for 0.5 mm-GBS.

Fig. 4.15 shows the comparison between the experimental and theoretical gas volumes in 1 mm-GBS. Likewise the conclusion of 0.5 mm-GBS, the TOUGH2 program is able to accurately simulate the average property of the moderate and high injection rates, in which gas flows through the most of possible coherent gas channels.

The relative error of gas injection with $Q_g = 10$ ml/min is noticeable in Fig. 4.15 a and Fig. 4.15 b. However, Fig. 4.13 shows a significant error for the lowest injection rate (i.e., $Q_g = 10$ ml/min). This error was addressed to the inability of the continuum model in describing the few distinct gas channels. The error of continuum modeling in 1 mm-GBS reaches up to 50 % for $Q_g = 10$ ml/min. A second reason for this large error may be unstable flow behavior at the smallest flow rate (section 4.2.1).

(a)   (b)
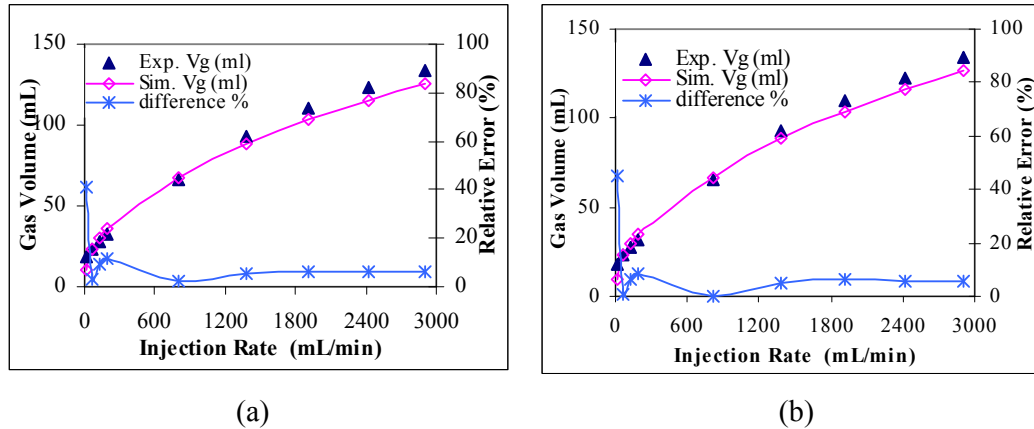
Fig. 4.15: Comparison of experimental and simulation results of steady-state gas volume versus injection rate in 1 mm-GBS when: (a) van Genuchten-Mualem model, (b) Brooks-Corey model are applied in TOUGH2 simulation.

Fig. 4.16 shows the 3D visualization of the gas distribution within the 1 mm-GBS for three different injection rates. These visualizations represent similar behavior of gas distribution shown in Fig. 4.14   for 0.5 mm-GBS. Consequently, the Brooks-Corey model predicts the gas distribution qualitatively better than van Genuchten-Mualem model. Accordingly, the Brooks-Corey model was used in TOUGH2 simulation.

The inability of TOUGH2 simulation in predicting the gas saturation of $Q_g = 10$ ml/min within 1 mm-GBS is visualized in Fig. 4.16.
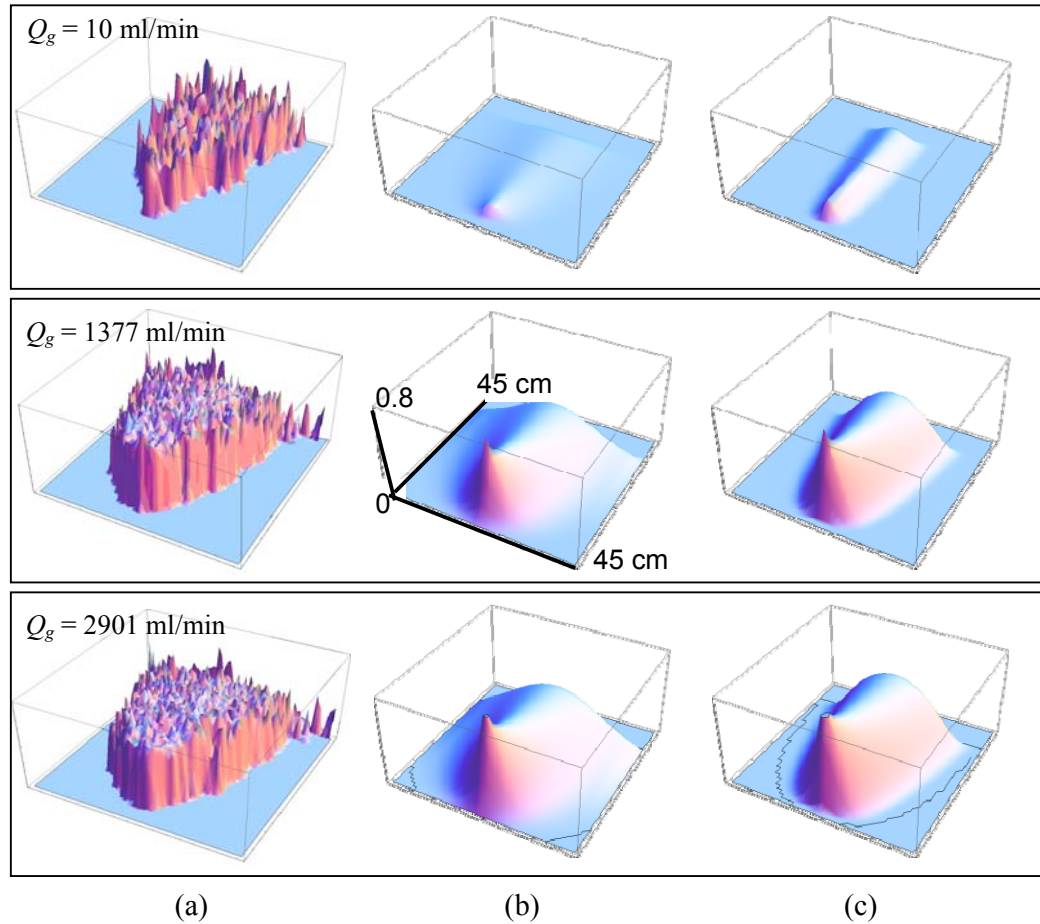
Fig. 4.16: 3D visualization of gas distribution in 1 mm-GBS for Q_g = 10, 1377 and 2901 ml/min: (a) bench-scale experiments by Krauss (2007), (b) TOUGH2 simulation using van Genuchten-Mualem model, and (c) TOUGH2 simulation using Brooks-Corey model.

4.4   Application of stochastic heterogeneity in continuum modeling

The experimental GBS is not a homogeneous porous medium, because all the glass beads do not have exactly the same size and pore spaces. This pore-scale heterogeneity is expressed by a specific pore size distribution. The experimental images by Krauss (2007) represented the heterogeneity of the distribution of the gas channels, which confirm that the GBS is a heterogeneous porous medium. The stochastic nature of gas channels may be due to the pore-scale heterogeneity as discussed in the introduction. Consequently, the stochastic heterogeneity is applied in TOUGH2 simulation to study the effect of heterogeneity on gas flow pattern.

4.4.1 Generation of 2D stochastic fields

A stochastic field is a set of random values defined over a field of variables by using the field specification (e.g., the mean value and variance). In this work, the stochastic permeability field is generated by using the HYDRO_GEN program (Bellin and Rubin, 1996). The HYDRO_GEN is an open source program that generates the random values in 2D with an assigned covariance function (variogram model). The HYDRO_GEN program utilizes five different covariance functions: Power law semivariogram, Gaussian, exponential, Whittle isotropic, and Mizell isotropic model. A set of random values created by the assigned covariance function, is called one realization.

The exponential covariance function is used in this work to create different realizations of the permeability field, since it is the standard covariance function used in the literature (e.g., Stauffer, 2009; Saadatpoor, 2009).

Exponential model

The variogram is the average of squared difference between the paired data:

$$\gamma(l) = \frac{1}{2N(l)} \sum_{(j,k)|l_{jk}=l} (v_j - v_k)^2 \tag{4.4}$$

where,

$\gamma(l)$ = variogram
l = specific length, [L]
$N(l)$ = total numbers of data that exist within the specific length l, [-]
$v_j - v_k$ = difference between parameters that lay within the specific length l

The standard equation of exponential variogram model comes is:

$$\gamma(l) = 1 - \exp\left(-\frac{3l}{a}\right) \tag{4.5}$$

where,

a = practical range, [L]

The covariance function reaches a constant value at large distances. It means that the changes in data between different points (or location) become independent. The distance, in which the properties change independently, is called sill. The practical range in Eq. (4.4) is a distance, at which the variogram values reaches 95% of the sill.

The exponential model has linear behavior close to the origin. However, it raises much steeper than the other models, but then it flattens out more gradually.

4.4.2 Stochastic simulation of 0.5 mm-GBS

The heterogeneity of the permeability field can be scaled to the capillary pressure field by the Leverett J-function function (1941) (see section 3.4).

Fig. 4.17 shows the modified relative permeability- and capillary pressure-saturation relationships for two grid blocks of 0.5 mm-GBS. The values of permeability modifier are equal to $\zeta_1 = 0.8$ and $\zeta_2 = 1.2$. A permeability modifier larger than one creates a higher permeability and a lower capillary pressure (Fig. 4.17). Therefore, applying different values of permeability modifiers in TOUGH2 creates heterogeneous parameter fields.

In TOUGH2, the modification of the capillary pressure (presented in Eq. (3.19)) is applied only to the entry pressure. Hence, the saturation-dependent function (i.e., $S_e^{-1/\lambda}$ in Eq. (2.41) or $\left(S_e^{-1/m} - 1\right)^{1/n}$ in Eq. (2.36)) remains unchanged by Leverett scaling. Fig. 4.17b shows how the entry pressure is scaled by the permeability modifiers.
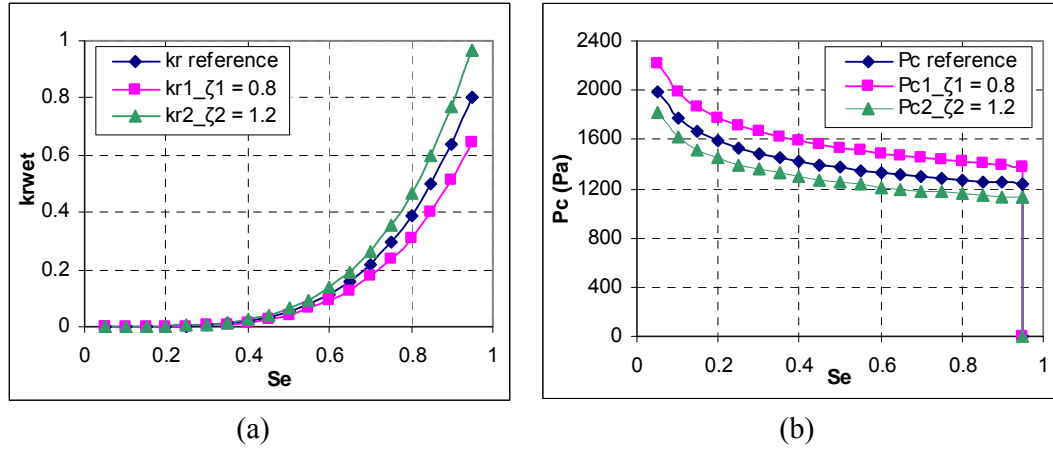
Fig. 4.17: Comparison of: (a) modified relative permeability-saturation relationships, and (b) capillary pressure-saturation relationships, of two gird blocks with $\zeta_1 = 0.8$ and $\zeta_2 = 1.2$ in 0.5 mm-GBS.

The experimental values of the mean and the standard deviation of the permeability field of the 0.5 mm-GBS, are equal to $k_{mean} = 9.23 \times 10^{-11}$ m^2 and $\sigma_k = \pm 0.36 \times 10^{-11}$ m^2, respectively (see Table 2.3). Therefore, the variance of the stochastic permeability field becomes equal to $\sigma_k^2 = 1.29 \times 10^{-23}$ m^4, which is used in the HYDRO_GEN program.

The 0.5 mm-GBS is considered as an isotropic porous medium (i.e., the permeability changes the same in principal directions) with a correlation length equal to 2 cm in the horizontal and vertical direction.

Fig. 4.18 shows the stochastic permeability field created by the exponential covariance function for the 0.5 mm-GBS. The cell size is equal to $l_x \times l_y \times l_z = 0.25 \times 0.25 \times 0.25$ cm. Stauffer et al. (2009) estimated the size of REV about 2 cm from the irregular borderline, when the fully saturated pack drained only by the gravity forces (for details see Stauffer et al., 2009). The same REV size is considered in this work, because the specifications of the experiments conducted by Stauffer et al. (2009) were similar to the ones performed by Krauss (2007).

The stochastic permeability field in Fig. 4.18 exhibits a sub-scale heterogeneity, since the heterogeneity was generated for cell sizes smaller than the REV-scale and larger than the pore-scale.

The results of the stochastic simulation are presented in Fig. 4.19 for injection rates equal to $Q_1 = 10$, $Q_4 = 146$ and $Q_{11} = 844$ ml/min. The comparison of the theoretical results shown in Fig. 4.19 with the experimental images of the gas distribution shown in Fig. 4.12, reveals that the correlated stochastic heterogeneity (i.e., a heterogeneity that is created by a covariance function) can represent only the average geometry of gas distribution.

Fig. 4.18: Stochastic permeability field created by exponential covariance function for 0.5 mm-GBS. The cell size is $l_x = l_y = l_z = 0.25$ cm.

The correlated heterogeneity of the permeability field that is shown in Fig. 4.18 is weak, because most of the stochastic values are close to the mean value (see the distribution of green in Fig. 4.18). This weak heterogeneity merges the modified capillary pressure values close to the reference capillary pressure. The weak heterogeneity in both permeability and capillary pressure fields is the reason that the stochastic simulation yields only the average parabolic geometry of gas flow pattern.

Q_1 Q_4 Q_{11}

Fig. 4.19: Visualization of stochastic simulation using exponential covariance function in 0.5 mm-GBS. The cell size is $l_x = l_y = l_z = 0.25$ cm.

In summary, applying the stochastic correlated permeability and capillary pressure fields in continuum models, can only generate the average properties of gas distribution when the experimental variance of permeability is used. This variance leads to a weak heterogeneity, which creates the nearly parabolic gas distribution close to the one

observed in the homogeneous simulation. The validity of this conclusion will be also tested for the 1 mm-GBS in the next section.

4.4.3 Stochastic simulation of 1 mm-GBS

Similar to 0.5 mm-GBS, the HYDRO_GEN program was used to create the stochastic permeability field of the 1 mm-GBS. The mean value and standard deviation of the permeability field are equal to $k_{mean} = 5.50 \times 10^{-10}$ m^2 and $\sigma_k = \pm 0.14 \times 10^{-10}$ m^2 (see Table 2.1). Fig. 4.20 shows the isotropic permeability field generated by exponential covariance function, when the cell size was equal to $l_x \times l_y \times l_z = 0.5 \times 0.5 \times 0.5$ cm and correlation length was 2 cm. Fig. 4.21 illustrates the results of the stochastic simulation by applying the heterogeneous permeability field shown in Fig. 4.20.
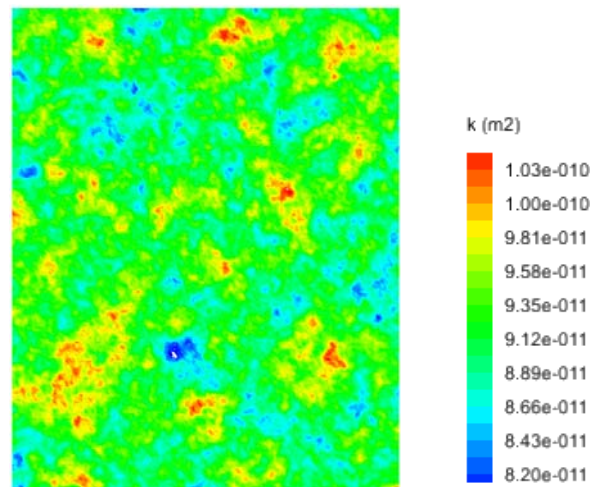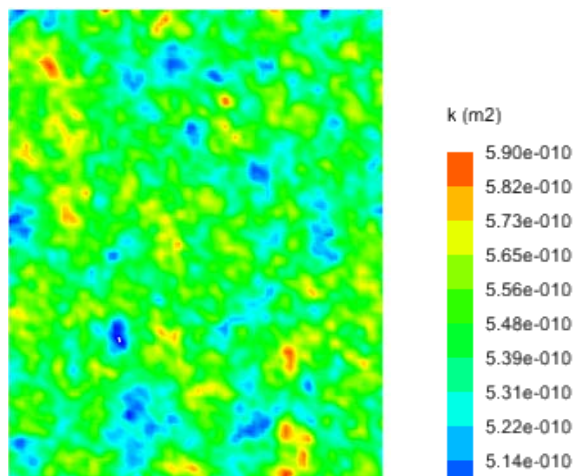

Fig. 4.20: Stochastic permeability field created by exponential covariance function for 1 mm-GBS. The cell size is $l_x = l_y = l_z = 0.5$ cm.
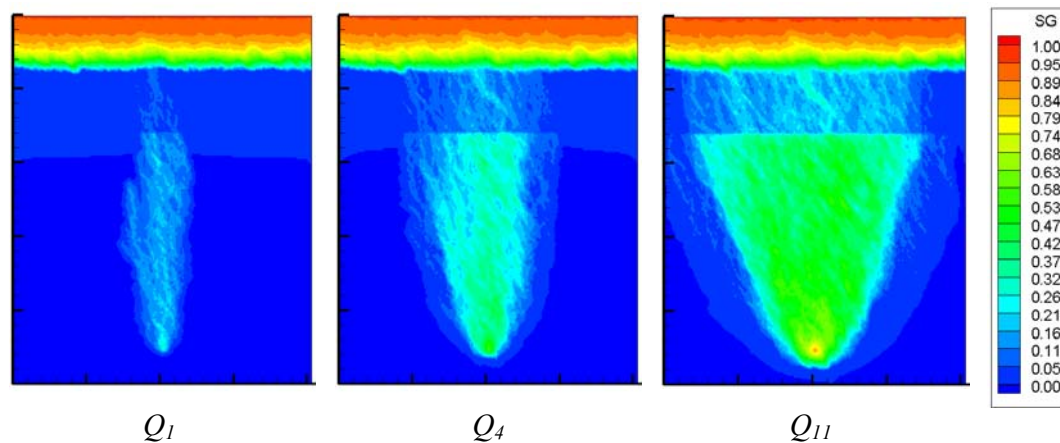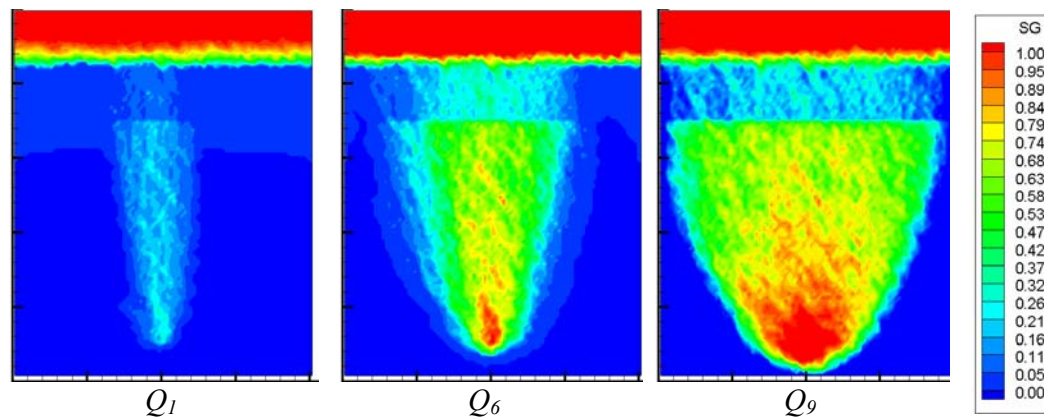

Fig. 4.21: Visualization of stochastic simulation using exponential covariance function in 1 mm-GBS. The cell size is $l_x = l_y = l_z = 0.5$ cm.

Comparison of the gas distribution in Fig. 4.21 with the experimental images (in Fig. 4.2b, Fig. 4.10e and Fig. 4.10h) confirms that the correlated heterogeneity based on the experimental variance, can only create the heterogeneous gas distribution.

In conclusions, applying the correlated stochastic heterogeneity in a continuum model (e.g., TOUGH2) is not able to create the gas channels observed in the experiments. The weakness of correlated heterogeneity created by covariance functions is a possible the reason for that.

4.4.4   Sub-scale simulation of 1 mm-GBS

As Stauffer et al. (2009) argued, a sub-scale simulation that applies the pore-scale heterogeneity is able to generate stochastic channelized gas flow pattern.

Stauffer et al. (2009) chose uniform distribution of pore radii and assumed that the permeability and capillary pressure vary with r^2 and r^{-1}, respectively. Therefore, the heterogeneity of pore radii creates the uncorrelated heterogeneity in permeability and capillary pressure fields. They generated the random distribution of pore radii and approximated the entry pressure by the Laplace-Young equation.

The same method is used to create the uncorrelated heterogeneous permeability and capillary pressure fields. The uniform distribution of pore radii is created by using the minimum and maximum pore radii, which are estimated experimentally (see Table 2.2). A random pore radius is assigned to each grid block that has the size of $l_x = l_y = l_z = 0.5$ cm. the stochastic heterogeneity is sub-scale, since the cell size are smaller than the REV.

The mean value and standard deviation of the permeability field are calculated after scaling the heterogeneity of pore radii into that field. These values are equal to $k_{mean} = 5.50 \times 10^{-10}$ m^2 and $\sigma_k = \pm 3.67 \times 10^{-10}$ m^2 for 1 mm-GBS. The mean value is equal to the absolute permeability of 1 mm-GBS (Table 2.3), but the standard deviation is much higher than the experimental value in Table 2.3. It means that the heterogeneous permeability field, which is estimated by the uniform-distributed pore radii, is stronger than the fields created by covariance function.

Fig. 4.22 shows the stochastic permeability field, which is obtained from the uniform-distributed pore radii. A comparison between Fig. 4.20 and Fig. 4.22 reveals that the heterogeneity in Fig. 4.20 is a smooth distribution close to the mean permeability value. In contrast, the heterogeneity shown in Fig. 4.22 is an a random distribution of the smallest and the largest permeability vales, in which only some infrequent cells have the mean permeability value.

Fig. 4.23 compares the experimental and theoretical gas distribution at the steady-state, when uncorrelated heterogeneity was applied for different injection rates $Q_1 = 10$, $Q_6 = 1377$ and $Q_9 = 2901$ ml/min.

In spite of correlated heterogeneity, the uncorrelated random pore-scale heterogeneity can create the stochastic channelized gas flow pattern for all injection rates (compare Fig. 4.21 and Fig. 4.23). Even though, the geometric similarity between the experimental and theoretical flow pattern is better for the lower injection rates.
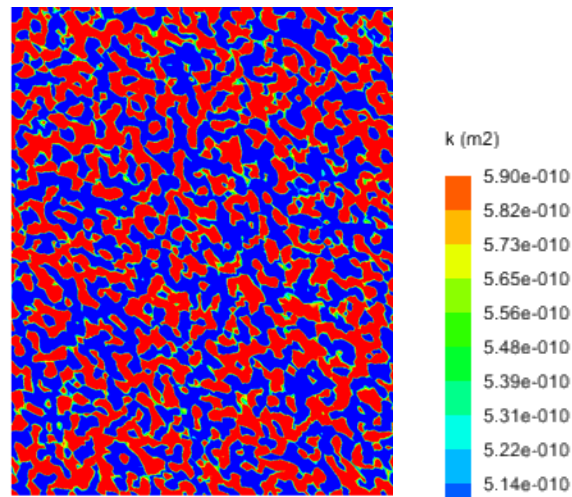
Fig. 4.22: Stochastic permeability field created by uniform-distributed pore radii for 1 mm-GBS. The cell size is $l_x = l_y = l_z = 0.5$ cm.

Q_1 Q_6 Q_9
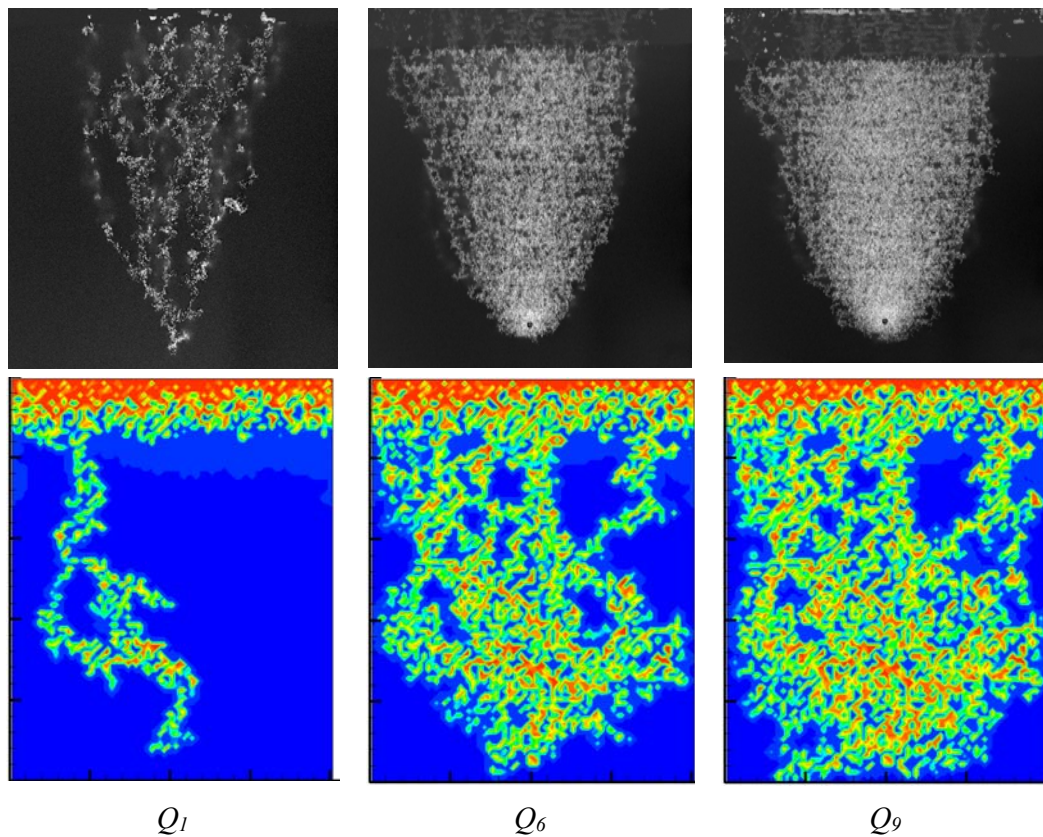
Fig. 4.23: Comparison of experimental (first row) and theoretical gas distribution of uncorrelated heterogeneity (second row). The cell size is $l_x = l_y = l_z = 0.5$ cm.

Stauffer et al. (2009) conducted only a qualitative comparison of gas distribution, and proposed the geometric similarity as a proof that the sub-scale simulation is able to generate the stochastic channelized gas flow pattern. This statement is controversial to many authors (see Chapter 1) stated that the continuum models can only yield the average flow properties. Therefore, a quantitative investigation is performed to check the ability of sub-scale simulation in prediction of average flow properties. The comparison of gas volumes in Table 4.6 reveals that the uncorrelated heterogeneity in sub-scale simulation yields theoretical gas volume much higher than the experimental values. Since the simulation model was created based on the experimental values, the only reason for this strong deviation is the strong heterogeneity of the permeability and capillary pressure fields. This is a dilemma how to estimate the sub-scale simulation: in one hand the uncorrelated heterogeneity generates the stochastic gas channels, on the other hand this strong heterogeneity leads to high gas volumes.

Table 4.6: Experimental and theoretical gas volume for injection rates presented in Fig. 4.23.

	$Q_1 = 10$ (ml/min)	$Q_6 = 1377$ (ml/min)	$Q_9 = 2901$ (ml/min)
Experimental measurement of V_g (ml)	18.25	93.33	134.15
Simulation value of V_g (ml)	32.25	88.92	235.72

Physically, the strong heterogeneity in permeability values results in a highly stochastic capillary pressure field. Since the higher capillary force dominates the buoyancy force, the stochastic gas channels develop more in horizontal direction. The wide distribution of the theoretical gas distribution shown in Fig. 4.23 confirms this statement. In addition, strong capillary force accumulates the gas phase, and results in a higher integral gas volume. Consequently, the uncorrelated stochastic simulation can confirm some parts of arguments by Stauffer et al. (2009), because of the strong deviation between the theoretical and experimental gas volume. Further research is needed to clarify the above mentioned dilemma about the sub-scale approach. Furthermore, the log-normal pdf function could describe the pore size distribution more accurate than the other functions (e.g., the uniform pdf function) (see Kosugi, 1996). Fig. 4.24 displays the log-normal and uniform distribution of pore radii in 1 mm-GBS (the r_{min} and r_{max} of the 1 mm-GBS are listed in table 2.2), in which the correlated distribution is more reliable than the uniform one.
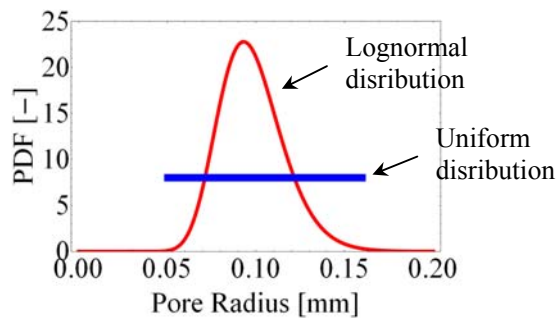
Fig. 4.24: Comparison of uniform and lognormal distributions of pore radii in 1 mm-GBS.

4.5 Conclusion

The most important conclusions of this chapter are listed as follows:

1. The local geometry of gas plume was investigated and proved that the phenomenological model developed by Selker et al. (2007) (i.e., the near-source region by an ellipsoid and the far-source region by a square-root relationship), predicts the extension of gas plume in near- and far-source regions with high degree of prediction ability. Since Selker's model considers the gas plume as an ensemble of distinct gas channels, only a dense capillary network can be described by this model. In case of low flow rates or a sparse capillary network, Selker's model cannot predict the gas distribution and dynamic multi-phase flow modeling is required.

2. The dynamic multi-phase model can describe the gas flow pattern that occurs in reality, if the key parameters of this model are estimated by experimental values. In this work, the values of gas saturation, entry pressure, porosity, absolute permeability and its variance were measured by independent experiments. In addition, the capillary pressure-saturation relationship was derived by Kosugi-relationship (1996) depending on a realistic log-normal pore size distribution. The maximum and minimum pore radii were estimated by realistic packing parameters. The Kosugi-relationship was calibrated by the experimental entry pressure. This calibrated relationship was the basis for the continuum model TOUGH2. For mathematical convenience, the Kosugi-relationship was fitted by the nearly identical curves: the van Genuchten-Mualem and Brooks-Corey model. Consequently, the calibrated continuum model has no degree of freedom to estimate the model parameters. This may be one reason for the excellent prediction ability of the continuum model for the important gas volume-injection rate relationship.

3. The simulation results of continuum model using van Genuchten-Mualem and Brooks-Corey model showed high degree of prediction ability in estimation of integral flow properties (i.e., gas volume) for both 0.5 mm- and 1 mm-GBS. In this work, the qualitative investigation (i.e., gas flow pattern) and quantitative measurement (i.e., the gas volume-injection rate dependence) of TOUGH2 simulation proved that the continuum model obtains the average flow properties, because it was developed based on continuum assumption that introduces effective properties at REV-scale.

4. The parameters of the constitutive relationships should be chosen to avoid the infinite pore radius. Otherwise, an arbitrary large pore can create a very steep conductivity function close to the full-saturation condition. The comparison of experimental and theoretical results, which were obtained by van Genuchten-Mualem and Brooks-Corey model, demonstrates the threshold in pore radii can significantly affect the simulation results. The van Genuchten-Mualem model creates a too wide gas plume and a smooth transition in gas saturation at the gas-water interface. The Brooks-Corey model creates a sharp transition in gas saturation, which is more reasonable according to the experimental observations. Consequently, the Brooks-Corey model is superior to the van Genuchten-Mualem model, since it takes into account the existence of a finite

entry pressure (i.e., existence of an upper maximum radius in pore size distribution).

5. The continuum model (e.g., TOUGH2) cannot simulate the transition from coherent to incoherent flow pattern, since it assumes continuum phases and can only be applied if the stability or coherence condition is satisfied in the multi-phase flow system (compare the experimental and theoretical results of $Q_g = 10$ ml/min in Fig. 4.16).

6. Continuum modeling with weak stochastic heterogeneity that is created by a covariance function and the experimental variance, cannot catch the essential features of the dynamic experimental gas flow pattern. In a weak heterogeneous permeability and capillary pressure field, most of the stochastic values are close to the mean value. In this work, the correlated heterogeneity in permeability and capillary pressure field, which was created by an exponential covariance function, represents only the average parabolic-geometry of gas distribution. In other words, a continuum model applying weak heterogeneity cannot describe the channelized flow pattern (i.e., single stochastic gas channels).

7. As discussed, there is a controversy in the literature if the continuum modeling can describe the channelized flow pattern. Stauffer et al. (2009) argued that a continuum model which is based on sub-scale heterogeneity yields a reasonable description of channelized gas flow pattern. This statement was proved by using strong random heterogeneous permeability and capillary pressure fields, which were created by a uniform pore size distribution. As discussed, the sub-scale continuum model can confirm some parts of the Stauffer's argument, namely it can create stochastic channelized flow. On the other hand the comparison of the theoretical and experimental gas volumes-injection rate relationship shows that the sub-scale continuum model gives too large gas volumes. Since the mean values of the porosity, the permeability and the entry pressure were estimated by experimental values, the only reason for this strong deviation is the strong heterogeneity of the corresponding stochastic fields. This is the dilemma of the sub-scale continuum model: on the one hand the strong heterogeneity generates the stochastic gas channels, on the other hand this strong heterogeneity leads to too large gas volumes. Further research is needed to clarify this dilemma.

5   Gas Injection at the Leuna Test Site

Micro-organisms are able to degrade a variety of organic contaminants (e.g., the aromatics like benzene and toluene, polycyclic aromatic hydrocarbons (PAH) like Naphthalene, and chlorinated hydrocarbons like chlorobenzene). Some of these micro-organisms are facultative anaerobic (i.e., they use oxygen as electron acceptor during the degradation process), and some of them are purely aerobic (i.e., they need oxygen to survive) (Beckmann, 2006). Furthermore, some contaminants (e.g., methyl tertiary butyl ether (MTBE)) are persistent in the anaerobic surroundings, and can be only degraded under aerobic conditions (Finneran and Lovely, 2001; Nyer et al., 2002). Therefore, the rate of in-situ bio-degradation will be enhanced, if oxygen is provided by reactive walls. The reactive walls use different injection methods: (1) solid phase injection (i.e., oxygen-releasing compounds), (2) liquid phase injection (i.e., dissolved oxygen), and (3) gas phase injection (i.e., direct gas injection).

In recent years, direct gas injection has been applied as an effective and cost-efficient method in comparison to the other methods (Fields et al., 2002). This method creates a broad zone of trapped gas bubbles within the porous media, in which the gas concentration increases in the groundwater flowing through (Fry et al., 1997). Air and Oxygen gas can be supplied in all amounts in direct gas injection. In addition, the direct gas injection does not need any special equipment for installation and injection processes. If the injection processes are performed accurately, the main part of the pore-spaces can be covered and results in high efficiency. Most of the problems that may occur in direct gas injection are related to inadequate information of the subsurface heterogeneity and the gas transport processes through the heterogeneous porous media.

In direct gas injection, two key parameters should be considered: (1) the distribution of gas phase within the heterogeneous porous media, and (2) the mass transfer from the gas phase into the water phase. When the distribution of gas phase becomes dense and homogeneous, the efficiency of direct gas injection to remove the contamination increases. But, the remediation is not completed without dissolution of oxygen in water phase. Therefore, the dissolution time to provide the oxygen for aerobic micro-organisms should be considered. Extensive experimental and theoretical investigations carried out for both constraints, at different scales (e.g., analysis of mass transfer process by Beckmann (2005) and gas flow pattern by Krauss (2007) at the bench-scale).

The mass transfer process (dissolution) in gas injection has been studied intensively over the last two decades (Semprini et al., 1990; Hoeppel et al., 1991; Fry et al., 1997; Luckner et al., 2001; Geistlinger et al., 2005; Beckmann (2006)). But, there are only limited works to investigate the efficiency of different gas injection scenarios on gas distribution at heterogeneous filed sites (Clayton, 1998).

This chapter focuses on direct gas injection that is carried out at Leuna test site to investigate the parameters (e.g., injection rate and injection time) of an efficient gas injection at the field-scale. An efficient gas injection refers to an injection process, in which the injected gas reaches to the contaminated area and the gas dissolves in water and stimulates the bio-degradation processes.

The experimental test site of this work is located in the eastern side of the chemical industry complex of Leuna at the southern part of Saxony-Anhalt state, and 30 km from both cities of Halle (Saale) and Leipzig. Fig. 5.1 locates the Leuna test site on the map. The groundwater monitoring at the Leuna test site shows a significant contamination in

the aquifer. The most relevant contaminants are petroleum hydrocarbons, aromatics (e.g., benzene, toluene, ethyl benzene and xylenes commonly referred to as BTEX compound), MTBE, polycyclic aromatic hydrocarbons (PAH), chlorinated hydrocarbons. Since these contaminants can be removed by aerobic bio-degradation processes, it was decided to inject oxygen and stimulate the bio-degradation process. The importance of choosing an appropriate flow regime to perform an efficient gas injection is investigated during the gas injection processes at Leuna test site. The hypotheses for the field-scale injection are derived from the results of the bench-scale experiments, and will be presented in the next section.

Fig. 5.1: Location of Leuna test site 30 km from cities Halle (Saale) and Leipzig (Google map).

5.1   Field-scale hypotheses derived from bench-scale experiments

Geistlinger et al. (2006) presented the principles for minimizing the free energy of an undulating gas channel and proposed a length scale-dependent transition from unstable incoherent to stable coherent flow (see section 3.2.1 in Geistlinger et al. (2006) paper). They emphasized the importance of considering the scale-dependent transition in flow pattern when the gas injection is performed at the larger scale. In other words, the transition phenomenon should be considered in generalization of the results from bench-scale experiments to the field-scale. However in this work, the results of bench-scale experiments were used to obtain the field-scale hypotheses, but the oxygen gas were injected with different scenarios to investigate the effect of scale on gas flow pattern.

To illustrate the hypotheses of gas injection in test site, a 2D realistic permeability profile, which consists of fine sand/coarse sand/fine sand sandwich structure in area of $L_x \times L_y = 35 \times 12$ m, is constructed in Fig. 5.2. The coarse sand has the high permeability and is contaminated by organic contaminants like BTEX and MTBE. Oxygen gas injection is applied at this field to remediate the contaminant.

In standard gas injection, oxygen gas would be injected directly into the contaminated layer (Fig. 5.2b). Assuming that the stability condition is satisfied (i.e., $Q_g > Q_{critical}$), one would anticipate the stable coherent channelized flow. However, this flow is transported only by few gas channels or a sparse channeling network. This would be

the worst case for the bioremediation process. If the injection rate in high permeable zone increases, the flow within the channels will increase, but the number of gas channels remains constant. Consequently, the gas saturation will only increase slightly. The lower fine sand layer (Fig. 5.2c) would be a more efficient location for gas injection, in which the injection rate creates stable flow with a large lateral extension of gas flow in the fine sand layer. The gas injection should create an unstable flow into the coarse sand layer, because of the grain-size dependent transition (see Fig. 1.4 in Chapter 1). The incoherent bubbly flow results in high gas saturation of trapped gas as Krauss (2007) has observed for 2 mm-GBS (see section 4.2.1). It means that the gas injection within the fine sand is an efficient injection, which creates high values of gas saturation through the contaminated area.
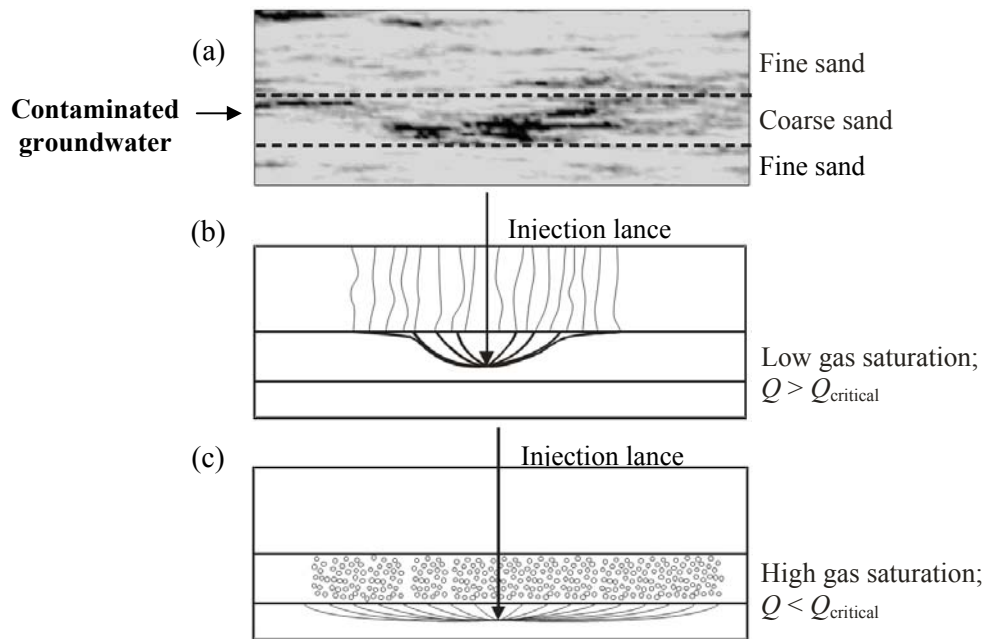
Fig. 5.2: Illustration of: (a) a realistic test site with heterogeneous permeability distribution, (b) stable gas flow created by direct gas injection in high permeable layer, (c) unstable gas flow created by direct gas injection in fine sand below the high permeable layer (Geistlinger et al., 2006).

Field-scale hypotheses

Working hypotheses for gas injection processes in field-scale (e.g., at Leuna test site) is derived from the results of laboratory experiments performed in bench-scale by Krauss (2007). As discussed in Chapter 4, the gas flow pattern is a function of injection rate, grain size and pore space geometry. Also, it was revealed that the transition in flow pattern in bench-scale depends both on the grain size and injection rate (see Fig. 1.4 in Chapter 1). Therefore, it is hypothesized that these key parameters also determine the flow pattern at the field-scale. Hence, the injection rate was chosen as a variable to conduct specific flow pattern. The description of competition between the forces in incoherent flow, which was described in section 2.2.1, showed that the incoherent flow may be developed at low injection rates. The higher injection rates create higher

pressure forces that may stabilize the coherent gas channels. The experimental observations by Krauss (2007) confirmed these results (see the results of gas injection in 1 mm-GBS in section 4.2.1).

The incoherent flow pattern establishes high gas saturation due to a dense network of trapped gas bubbles through the invasion zone, but in coherent flow the gas flows through the established coherent channels. On the other hand, the phenomenological high injection rate influences the larger area of the porous medium.

Therefore, the main strategy of gas injection in test site is high flow rate injection to invade a large area, and low flow rate injection to create maximum gas saturation by trapped gas bubbles.

As a result, for an efficient gas injection the following factors are important:

1. Determining the fine-scale heterogeneity in horizontal and more important in vertical directions.
2. Investigation of the geological layering (e.g., thin clay lenses or layers).
3. Determining the injection regime: continuous injection, pulsed injection, low-pressure injection or high pressure injection.

Before applying the continuum models (e.g., TOUGH2) to simulate the gas flow patterns at field-scale, one has to check whether the stability condition is satisfied to achieve stable coherent flow (i.e., $Q_g > Q_{critical}$, see section 2.2.2). Also, It is necessary to investigate whether the simulation length (i.e., the extension of model used in simulation) is smaller than the estimated length-scale, at which the flow pattern is coherent, because the flow pattern may be change by increasing the scale. In addition, the realistic capillary pressure-saturation relationship should also be estimated for simulation of channelized flow pattern.

However, the simulation of gas injection is simplified in modeling, but the heterogeneity of the porous media highly influences the multi-phase flow. The simulation of gas injection in bench-scale revealed that applying the heterogeneity in permeability- and capillary pressure-saturation relationships dramatically changes the simulation results (compare the simulation results of 1 mm-GBS in sections 4.3.4 and 4.4.3). Therefore, the simulation of gas injection in field-scale is performed by applying the heterogeneity in permeability- and capillary pressure-saturation relationships.

Thus, four different injection regimes (injection scenarios) were conducted at Leuna test site by using the described field-scale hypotheses. These injection scenarios are smart combination of low injection rate (or low pressure injection (LPI)) and high injection rate (or high pressure injection (HPI)).

To optimize the direct gas injection in field-scale, a proper simulation model is needed, which consists of the variety of field site properties (e.g., geological properties, permeability value, and etc.). The simulation model was used to investigate these field scenarios, in which most of the parameters are taken from the measured values at field site. Before discussing the modeling results of field-scale gas injection, a short overview of different measurements used for the parameterization of the test site model, will be presented.

5.2   Monitoring network

The direct oxygen injection can be applied successfully at the test site, if sufficient information about its hydro-geological properties (e.g., porosity, absolute permeability, and velocity of groundwater) and geochemical properties (e.g., the type of contaminants) are available. In addition, providing the accurate properties of the test site is important to build a model that simulates the multi-phase flow similar to the fluid flow occurring in reality. Therefore, determination of the subsurface heterogeneity and distribution of the contaminants are the first steps of designing and optimizing the injection process. Fine-scale heterogeneity often plays an important role in managing the groundwater flow and remediation of groundwater contaminant. Therefore, identification of preferred gas-flow paths in the horizontal direction (e.g., high permeable loose structure, sandy to medium-coarse grains layers) and gas barriers in vertical direction (e.g., low permeable dense structure, fine grains layers, high clay and silt content) are critical.

The horizontal permeability dramatically affects the gas distribution of injected gas in horizontal direction, especially if injected gas has to be reached the contaminant which is spread throughout a wide area. The permeability values in horizontal direction changes continuously within a geological layer. These observations necessitated the measuring of permeability distribution in horizontal direction, and applying this heterogeneity in simulation. Therefore, the permeability values should be measured in different location of test site to give the opportunity of measuring the mean and the variance of the distribution of permeability values.

In gas injection, gas moves upward because of buoyancy forces. Therefore, measuring the permeability in vertical direction becomes important. However, the permeability in horizontal direction is measured, but there is a big difference in horizontal and vertical permeability due to the different sedimentation. It means that the vertical permeability should be measured and investigated separately. In vertical direction, presence of the clay lenses is the most important heterogeneity that changes the permeability values. Fig. 5.3 shows schematically an oxygen injection in a contaminated area, in which the clay lenses affected the gas flow. This figure shows how the clay lenses or lower permeability sediments act as gas-blocking lenses.
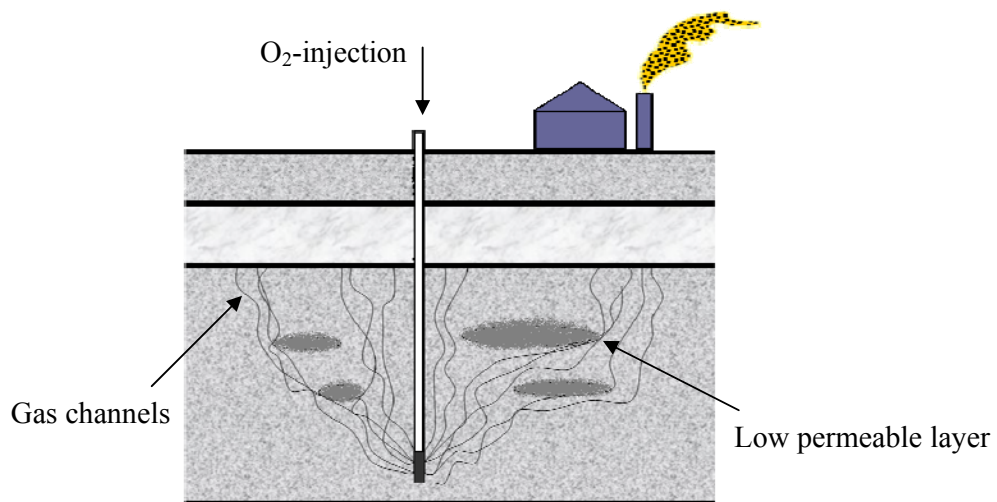

Fig. 5.3: Illustration of gas distribution in a heterogeneous aquifer.

In addition to the permeability values in horizontal and vertical direction, the porosity values and the capillary pressure-saturation relationship should be measured or estimated. The porosity value is used to estimate the required gas volume for injection, and the entry pressure of capillary pressure-saturation relationship gives the estimation of pressure should be supplied in injection processes.

Therefore, different tools and probes were installed at the Leuna test site to measure and estimate the properties of test site. The direct-push sampling method is used in this work to perform subsurface investigations. The direct-push (DP) is a method that can measure depth-dependent properties by driving the hollow steel rods into the ground. The sampling tools are attached at the end of steel rods and collect the soil samples. In addition, the DP rods can be equipped with different probes to provide in-situ measurements of subsurface properties (e.g., electrical resistivity, gas saturation, and temperature). The advantage of DP sampling method is the variety of measuring tools that can be attached to the DP rods. Comparing with the traditional drilling methods, the DP sampling method is fast and inexpensive for studying the subsurface unconsolidated sediments.

In addition, the column test, and sieve analysis are interpreted to investigate the sediment characterization. These characterizing methods are described briefly in this section.

5.2.1 Direct-push injection logging

The direct-push injection logging (DPIL) are assembled at the University of Tübingen (Centre for Applied Geosciences) to provide the hydraulic conductivity data in horizontal direction with high-resolution. The filter element in DPIL is used to measure the hydraulic resistance of the flow through the sediments. The resistance to the flow is interpreted as the inverse of the hydraulic conductivity. In other words, the measured data by DPIL characterizes the hydraulic conductivity in the vicinity of the injection point. In overall, eight DPIL were operated up to 11 m depth in Leuna with a vertical resolution of 30 cm to 50 cm. The measured hydraulic conductivity values range between 1.3×10^{-4} m/s and 8.78×10^{-6} m/s, which can be interpreted as hydraulic conductivity in horizontal direction.

5.2.2 Direct-push electrical-conductivity logging

If the chemical properties of the fluid within the pores do not vary too much, the electrical conductivity of saturated media highly depends on the clay content. The higher clay content conducts higher electrical conductivity (Schulmeister et al., 2003).

The direct-push electrical-conductivity logging (DPEC) can show the presence of the lenses or thin impermeable layers at the test site. Contrary to DPIL, the DPEC does not measure the vertical hydraulic conductivity, but provides the estimation of location, thickness and lateral extension of low permeable zones and is therefore the main database for estimating the vertical permeability.

McCray (2000) emphasized that the high capillarity of clay influences the capillary-related flow. For instance, the dry clay will exert capillary suction on wetting phase (e.g., water) and allow the capillary transport the wetting phase into the clay. On the other hand, the wetted clay tends to act as a capillary barrier to the non-wetting phase (e.g., air). In this case, the non-wetting fluid may enter to the clay, if the pressure in the non-wetting phase is great enough to overcome the capillary force of wetted clay. These phenomena greatly influence the air flow in the subsurface during the sparging.

Therefore, characterization of thin impermeable layers of clay by DPEC in vertical direction becomes important (Christy et al., 1994). In addition, the information of DPEC is used to find an appropriate place the injection lance.

At test site, 12 DPEC measuring probes were conducted up to the depth of 10.7 m. The electrical conductivity was measured in milli-Siemens/m as the reciprocal of electrical resistance. The measuring data are collected online with the Geo-probe device (Soil Conductivity Instrumentation Case SC-150, Geoprobe software: Image Direct Soil Conductivity 4.0).

5.2.3   Sieve analysis and column test

The sieve analysis, which were carried out nearby the sensor field, were used in this work by assuming the same rock types extend in sensor field (see SAFIRA project, Remediation Research in Regional Contaminated Aquifers, UFZ Leipzig-Halle, 2006).

The Rosetta database (Schaap, 2002; free download from http://www.cals.arizona.edu/research/rosetta/index.html) was used to estimate the hydraulic properties of rock types obtained in sieve analysis. Rosetta database considers 12 rock types, which are classified based on the percentage of silt, sand and clay. The triangle classification of soil texture in Rosetta database is presented in Fig. 5.4.

For instance, a soil sample that consists of 30 % sand, 10 % clay and 60 % silt, is classified as silt loam based on triangular (see the red symbol in Fig. 5.4). The properties of the soil sample are considered equal to the properties of the rock class that soil sample belongs to.
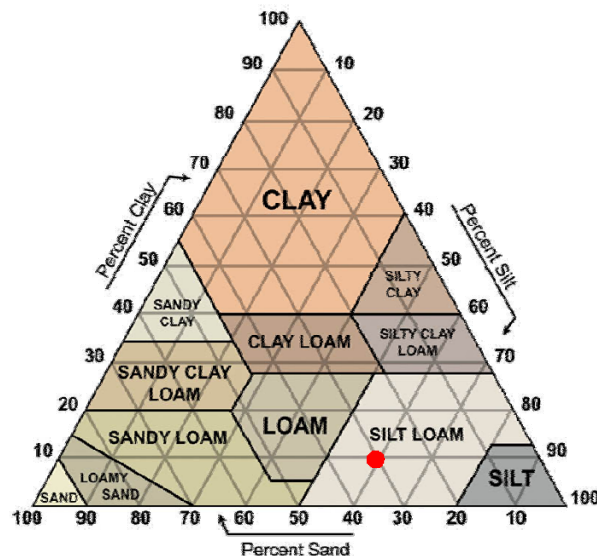
Fig. 5.4: Triangular classification of soil texture in Rosetta database (U.S. Department of Agriculture (USDA), 1951).

In addition to the sieve analysis, the 36 column tests were used to determine the geological properties of the soil texture (e.g., porosity and bulk density) at sensor field. The hydro-geological properties (i.e., porosity, horizontal and vertical permeability) and 3D geological structure can be determined by using the survey investigation and measurement results at the test site. In addition, for evaluation of the modeling results the in-situ gas distribution has to be measured with high spatial and temporal

resolution. Therefore, a dense sensor array (i.e., the set of in-situ sensors and probes) was installed at the Leuna test site. The sensor array is designed and installed at the Leuna test site in the course of ProinoII project, which was performed by UFZ (Helmholtz Center for Invionmental Research) and Sensatec GmbH. The sensor array is used to create a model by measuring geological properties and to validate the simulation results by measuring gas saturation distribution. The in-situ sensor array installed in Leuna test site will be described in the next section.

5.3   In-situ sensor array

Different sensors were installed at the Leuna test site to measure the gas saturation and the concentration of dissolved gas during and after the injection processes at different depths. Therefore, the measurement at the test site has high resolution that facilitates the investigation of gas flow in 3D, and gives the opportunity to compare the measured and simulated gas saturation.

The sensor array consist of five moisture sensors (Sensatec, GmbH, Germany), 16 redox-potential sensors (Sensatec, GmbH, Germany), 16 temperature sensors (Sensatec, GmbH, Germany), and 55 oxygen sensors (Presens GmbH, Germany).

The moisture sensors are developed based on the time domain reflectometry (TDR) method, which is a reliable method to measure the volumetric water content. The volumetric water content in the aquifer was measured during and after the injection processes. From a local reduction in water content during the injection, the volumetric gas content and gas saturation profile can be determined.

The principal of TDR method is measuring the velocity (or transit time) of an electromagnetic pulse through a sample. The pulse is sent at the end of the TDR-probe, and then returns to its source after passing the porous medium.

The redox-potential sensors measure the tendency of the soil solution in transferring the electrons. In redox-potential sensor, a platinum wire is buried into the soil and conducted the electrons between the soil and a voltmeter, which is connected to a reference electrode. The voltmeter measures the voltage needed to stop the current of electrons between the platinum wire and the reference electrodes.

The temperature sensor is used to measure the temperature while increasing the temperature is an evidence of microbial activity.

The oxygen sensor consists of polymer optical fiber (POF) (PreSens GmbH, Regensburg, Germany) with a polished tip, which is coated with a planar oxygen-sensitive foil (PS) (PreSens GmbH, Regensburg, Germany). The end of the POF is covered with a steel tube to protect both the POF and SF. The oxygen sensor evaluates the phase shift between the excitation light and fluorescence response from SF that has advantage of measuring the oxygen concentration independently of the flow velocity and without oxygen consumption. In the presence of oxygen the phase angle decreases. The oxygen concentration was measured by a oxygen meter (Fibox, PreSens GmbH, Regensburg, Germany, smaller than 0.05° phase resolution), which the sensor is attached to.

In this work, the Leuna test site refers to a rectangular area of 60 × 25 m. Fig. 5.5a shows the Leuna test site where all the sensors and probes (i.e., sensor array) were installed. While, the injection processes were performed within a smaller area of 5 × 10 m, which is called sensor field. The arrangement of sensors and injection lances within the sensor field is also shown in Fig. 5.5b.

Since all the injection processes and gas saturation measurements were carried out at the sensor field, therefore an overview of sensor field will be presented.

An overview of sensor field

Fig. 5.5b shows the locations of sensors and injection points. In this figure, the moisture, redox-potential and oxygen sensors are numbered with TDR, Eh and Opt, respectively. Each lance is named by the sensor that was operated on that location. For instance, the moisture sensors were operated only at the location of TDR1, TDR2, TDR3, TDR4, and TDR5. In Leuna test site, two lances GP11 and TDR2 were chosen for gas injecting (see Fig. 5.5b). While these two lances were surrounded by measuring sensors, the experimental properties (e.g., gas saturation, dissolved oxygen, and temperature) can be measured with high resolution (i.e., the gas saturation can be measured at least within a radius of 30 or 50 cm). When the gas was injected at one of these two lances, the other lance was used for measuring the gas saturation. The following simulation aims to investigate the distribution of gas saturations at TDR2, when gas was injected at the GP11. The locations in Leuna test site are named in accordance to the installed sensor. In Fig. 5.5b, the Eh refers to the redox-potential sensor, and the optode sensors, which utilized the optical measurements, are shown by Opt. In this figure, TDR is also used to number the moisture sensors.

(a)   (b)
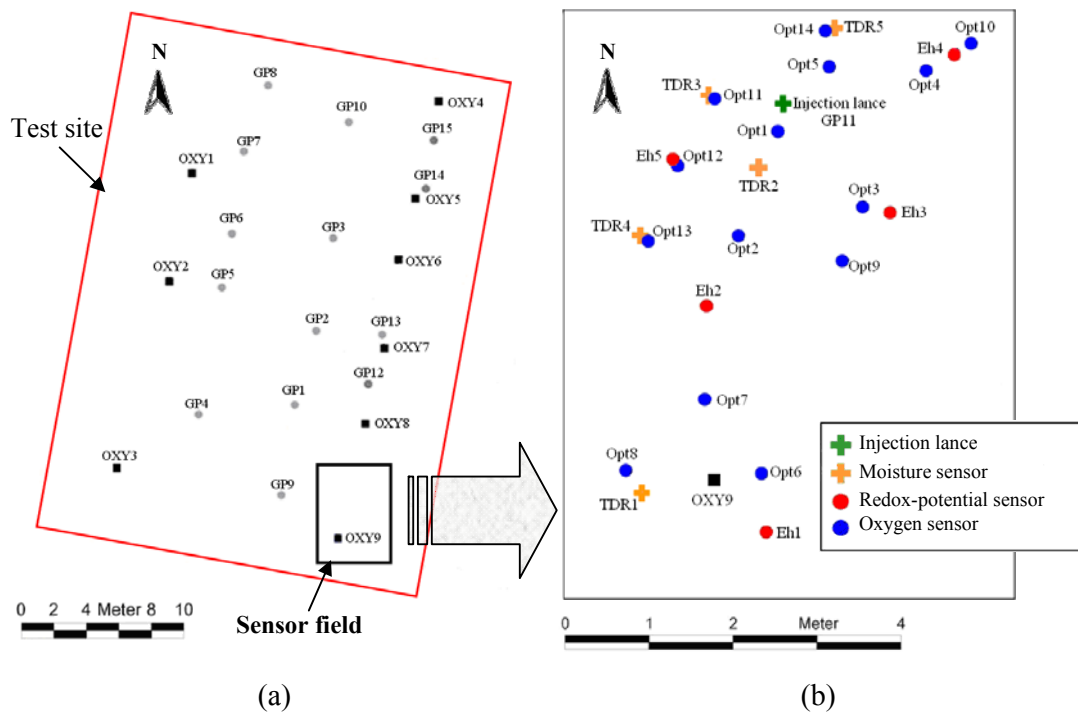
Fig. 5.5: The arrangement of sensors and injection lances in the sensor field.

5.4   The art of gas injection

For injection processes at the Leuna test site, the control variables are flow rate (i.e., injection rate, injection pressure), fumigation (i.e., pulsed, continuous, progressive, variable), and the bulk volume of the injected gas. The hypotheses of the injection were described in section 4.1. Therefore LPI and HPI were performed at the Leuna test site to investigate the incoherent and coherent flow pattern.

5.4.1 Gas injection scenarios at GP11

In all injection experiments at the Leuna test site, 3 m³ of pure oxygen gas was injected into the water-saturated aquifer. Table 5.1 listed the name and the specification of injection scenarios (e.g., method, injection rate, injection pressure, and injection time) performed at GP11. The name of injection scenario counts the injection process by the numbers. At the Leuna field site, the gas injected by LPI and HPI that refers to $Q_g < 33$ l/min and $Q_g \geq 33$ l/min, respectively.

Table 5.1: Gas injection scenarios carried out at GP11.

Injection scenario	Method	Injection condition	Injection time (min)
E1	LPI	25 l/min, 1.8 bar	120
E2	LPI	3 l/min, 0.8 bar	996
E3	HPI	40 l/min, 8.0 bar	75
E4	HPI/ LPI	HPI: 40 l/min, 8.0 bar LPI: 3 l/min, 0.8 bar	390

The scenario E1 is the first injection scenario at GP11, in which the gas was injected with $Q_g = 25$ l/min. Then the injection rate was decreased to 3 l/min in scenario E2. In contrast to LPI, a very high injection rate (e.g., 40 l/min) was applied in scenario E3.

Since the LPI and HPI have some advantages and disadvantages, a combination of both injection methods were applied in the scenario E4. In scenario E4, 1.68 m³ of gas was injected by HPI, and 1.32 m³ by LPI. The HPI created a broad distribution of injected gas, and then LPI created high saturation of trapped gas bubbles. In the working hypotheses, namely the HPI leads to coherent flow and LPI leads to incoherent flow pattern.

During and after the injection process, the variables and properties (e.g., oxygen saturation) are measured by the in situ sensor array. In this work, the time intervals of measurement are referred to t_1, t_2 and t_3, which are listed in the Table 5.2 for the corresponding scenarios of Table 5.1. Comparing the time intervals in Table 5.1 and Table 5.2 reveals that the t_1, t_2 and t_3 correspond to the measuring time during gas injection, at the end of gas injection and after gas injection.

Table 5.2: Time intervals of saturation measurements at the Leuna test site.

Injection scenario	t_1 (min)	t_2 (min)	t_3 (min)
E1	30	120	240
E2	-	1020	1140
E3	15	75	120
E4	40	480	540

5.4.2 Measurement of gas saturation at Leuna test site

The visualization technique (e.g., the one was used to obtain the 2D images in bench-scale experiments) cannot be utilized at the Leuna test site to obtain the images of gas saturation in 2D or 3D. But, investigation of gas distribution is still important. Therefore, at the Leuna test site, the influence of gas injection in the sediment in horizontal direction (i.e., ROI) becomes an important parameter where the maximum cross-sectional area should be influenced. The ROI is significantly influenced by the

injection rate. The ROI should be measured in horizontal direction of parabolic gas plume, not at the diagonal line.

Fig. 5.6 represent one example of ROI investigation when gas injected in GP11. In this figure, the actual distances that the gas phase has to travel to reach the observation point at Opt2, are much higher than the ROI value, which is measured horizontally equal to 3.16 m in Fig. 5.6.
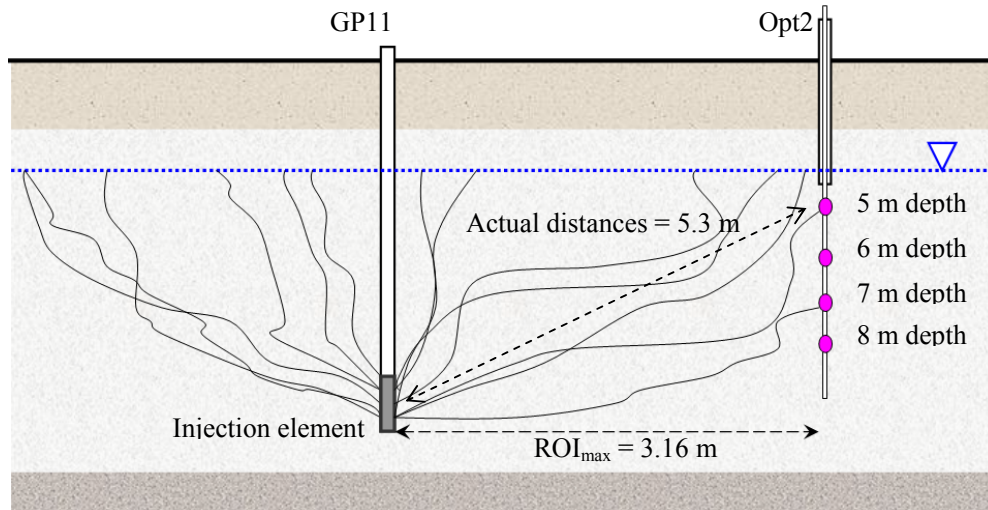
Fig. 5.6: Measurement of ROI at the OPT25 when gas is injected in GP11.

The Table 5.3 listed the maximum and mean values of ROI when gas was injected at GP11 and noticeable gas saturation (i.e., $S_g > 0.05$) was measured at the lances. The maximum ROI relates to the most far lances where the gas saturation was measured.

Table 5.3: The maximum and mean values of ROI in gas injection process at GP11.

	Injection scenario			
	E1	**E2**	**E3**	**E4**
Maximum detectable ROI (m)	2.02	2.02	3.16	3.83
	Opt3 at 7 m	Opt3 at 7 m	Opt 2 at 5 m	Opt2 at 2 m
Mean value of ROI (m)	1.55	1.39	1.57	1.94

The simplifying assumptions (e.g., the cylindrical gas distribution with an average porosity of 30 % and a dynamic gas content equal to 10 %) are considered to estimate the theoretical ROI. By using these assumptions, the ROI is calculated equal to 2.4 m for 3 m³ gas injection. The maximum ROI in Table 5.3 for HPI scenarios (e.g., E3 and E4) are higher than the expected ROI, while the ROI in LPI scenarios (e.g., E1 and E2) did not reach to the expected ROI.

The differences between the ROI of LPI and HPI are significant (i.e., the average value of differences is about 1.8 m). It is because of the buoyancy forces that force the gas moves upward when the injection rate is low. In high injection rate, the buoyancy forces are not strong and gas distributed more in horizontal direction.

Fig. 5.7 shows the gas saturation profile measured by moisture sensor at location TDR3. The gas saturation was measured at three different time intervals (i.e., t_1, t_2, and t_3) for all four injection scenarios. The representative geological profile for the sensor field is shown in Fig. 5.7. This profile was obtained at the location of OXY9. This geological profile is used to calibrate the gas saturation measurements and to estimate the properties of the rock types. The measured gas saturation was analyzed to recognize the gas flow pattern.

In Fig. 5.7b, the measurement of gas saturation in E2 does not show any changes at different time intervals. The reason is that the gas was injected with low injection rate equal to $Q_g = 3$ l/min. The most probable flow regime was incoherent bubbly flow, in which the gas injection created high saturation of trapped gas bubbles. Since the gas phase consists of trapped gas bubbles, a significant change in gas distribution is rather unlikely. Only after a certain dissolution time, the bubble size is shrunk and they can move upward as long as they were trapped again (Beckmann, 2007). The upward moving of gas bubbles will increase, since the hydrostatic pressure decreases.

On the other hand, large differences were observed in E3 between the gas saturation at different time intervals (see Fig. 5.7c). The measured saturation decreased dramatically after stopping the injection in scenario E3, in which the gas was injected with high flow rate $Q_g = 40$ l/min. Comparison of gas saturation at t_2 and t_3 shows that the gas saturation of lower layers is decreased, while it is increased at the upper layers. The simultaneous decreasing and increasing of the gas saturation can be interpreted as coherent channelized flow, in which the gas flows within the stabilized channels after stopping the injection process and decreases the gas saturation at the lower layers.
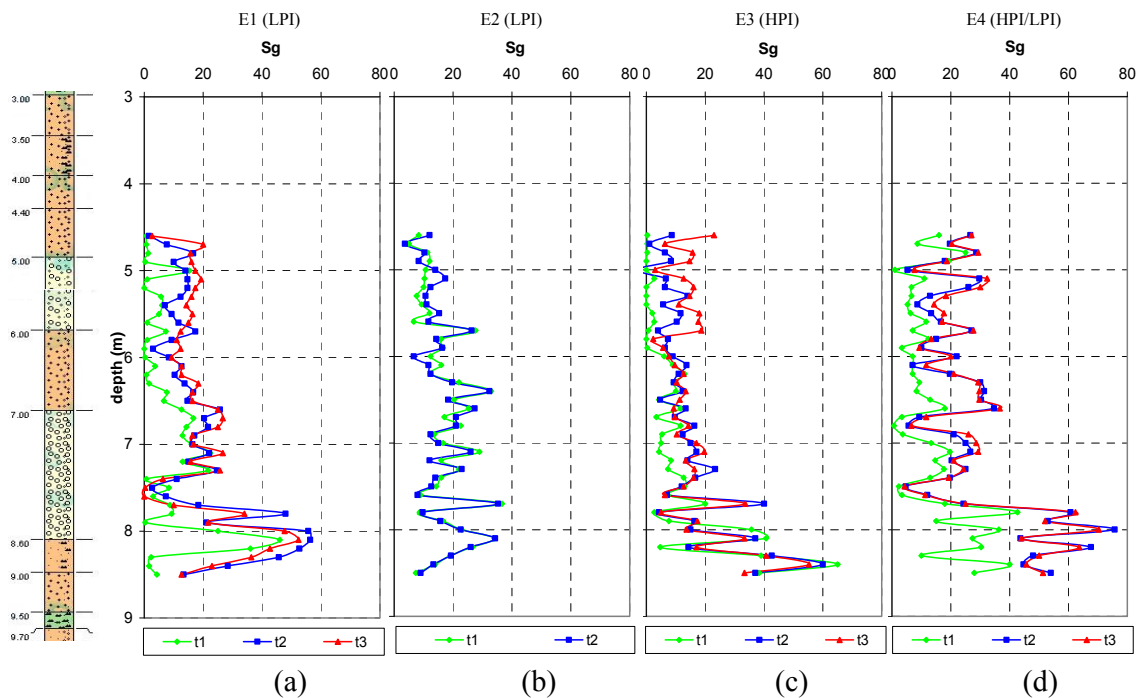

Fig. 5.7: Gas saturation measurement at TDR2 for scenarios: (a) E1, (b) E2, (c) E3, (d) E4 at time intervals t_1, t_2, and t_3.

The average values of gas saturation measured within four different sediment classes were calculated and presented in Table 5.4.

The average values of gas saturation show that the well-sorted sand has minimum range of gas saturation, while the fine sand has significantly the highest gas contents.

The fine sand could store the gas up to a saturation of 26.8 % (E4). Based on Eq. (2.27a), Eq. (2.27b) and Eq. (2.30), the pore size distribution depends on grain size. Therefore, fine sand has smaller pore sizes compared with medium-coarse sand and fine-medium gravel. If the Hagen-Poiseuille law is valid for the flow through the pores, then smaller pore radii result in smaller permeability values. Therefore, the porous medium with smaller pore radii accumulates higher gas saturation to conduct the same permeability values that a porous medium with larger pore radii has. Therefore, the fine sand could store higher gas saturation as residual or trapped gas bubbles.

The comparison of the gas saturation in different injection method reveals that LPI scenarios yielded a higher gas saturation compared with HPI. The differences in gas saturation of LPI and HPI vary from 2.1 % within the fine to medium gravel, to 5.8 % within the well sorted sand. This conclusion confirms the hypotheses of section 5.1 that stated the LPI creates higher gas content than HPI within the porous media.

The HPI/LPI scenario yields high gas saturation and efficiency regards to LPI and HPI in test site.

Table 5.4: Average gas saturations measured at TDR2.

		Average value of gas saturation (%)			
	Injection scenario	fine sand	well-sorted sand	medium-coarse sand	fine-medium gravel
LPI	E1and E2	-	13.33	14.75	16.80
HPI	E3	19.17	7.53	10.66	14.67
HPI/LPI	E4	26.78	7.48	22.13	30.01

5.5 Continuum modeling of gas injection scenarios

The results of stochastic simulation in Chapter 4 revealed that the TOUGH2 program can accurately predict the average properties (e.g., average gas volume). In this section, the heterogeneous permeability and capillary pressure fields were applied in continuum model to simulate the injection scenarios E1, E3 and E4. In addition, the simulation work utilized the inverse modeling to calibrate the model. The measurements of sensor array were used to validate the simulation results.

5.5.1 Specification of simulation model

The dimension of the simulation model was $L_x \times L_y \times L_z = 6.8 \times 6.8 \times 6.8$ m, in which the injection lance (i.e., GP11) was placed at the center. The size of one grid block in the simulation model was $l_x \times l_y \times l_z = 0.2 \times 0.2 \times 0.2$ m that implied 34 grid blocks in each direction. Fig. 5.8 shows the top view of the discretized model in respect to the sensor field.
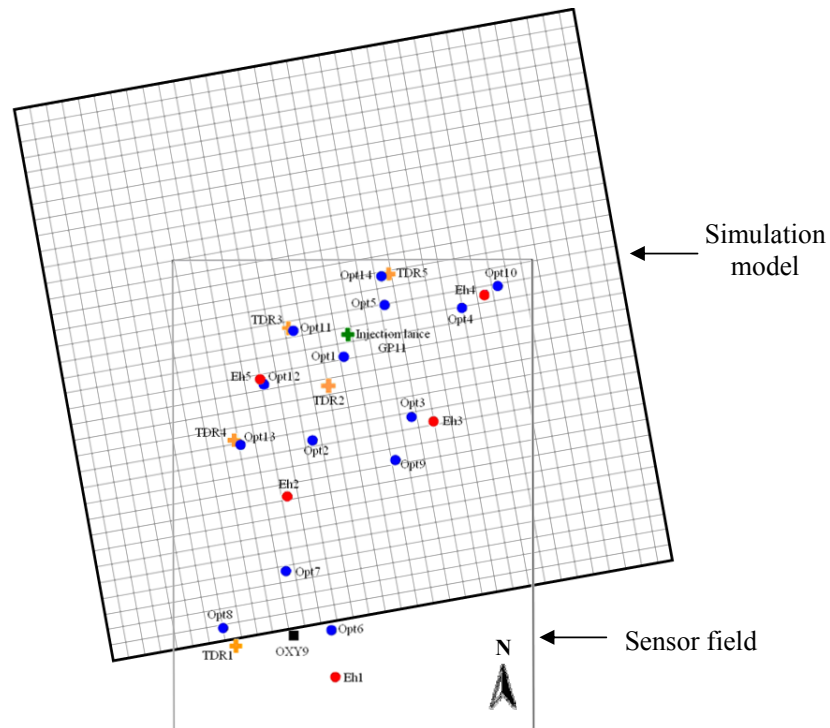
Fig. 5.8: Top view of discretized model respect to the sensor field.

Measurement in test site declared that an impermeable layer extended at the top and the bottom of the aquifer. But, still there is a connection between the saturated and unsaturated zones at the top of the aquifer.

The distribution of water saturation at capillary-gravity equilibrium was used as the initial condition for injection part. In order to create the equilibrium condition, the Dirichlet boundary condition is applied at the top and bottom of the model. For the boundary condition in injection process, infinite acting is considered in all direction similar to the condition at the test site.

The results of direct-push sampling, DPIL, DPEC, and column tests were used to estimate the geological structure (i.e., the extension and the thickness of each rock types) in sensor field. The results of sieve analysis performed in SAFIRA project were also used as evidence to estimates the properties of rock types by using the Rosetta database. The parameters of the consecutive relationships for different rock types in sensor field are listed in Table 5.5. The vertical permeability is considered ten times smaller than the horizontal permeability in this work. This proportionality is not valid in general circumstances.

Table 5.5: Parameters of consecutive relationships for the rock types of the sensor field.

Parameter		Rock type 1	Rock type 2	Rock type 3	Rock type 4	Rock type 5	Rock type 6
Porosity (%)		36	36	36	36	36	34
Permeability $(m^2) \times 10^{12}$	x-direction	2	1	1	1	1	1×10^{-1}
	y-direction	2	1	1	1	1	1×10^{-1}
	z-direction	2	1	9×10^{-1}	1×10^{-1}	5×10^{-2}	1×10^{-3}
Relative permeability in Brooks-Corey model	λ in Eq. (2.42)	3.17	3.15	3.15	3.15	3.15	3.14
Capillary pressure (Pa) in Brooks-Corey model	α_p (m^{-1})	5.0	3.6	3.6	3.6	3.6	1.08
	λ in Eq. (2.41)	3.05	3.0	3.0	3.0	3.0	3.00

5.5.2 Application of Heterogeneity in Continuum Modeling

At the Leuna test site, several geological survey and logs were acquired. This database was used to create the stochastic permeability fields. SGSIM (Sequential Gaussian Simulation program, Deutsch & Journel, 1998), which is a geo-statistical program of GSLIB library (Geostatistical Software Library, Deutsch & Journel, 1998), was used to create a stochastic permeability field in 3D. The SGSIM is based on a conditioned algorithm (i.e., the algorithm is forced to yield the measured permeability values at the different locations of the test site). Hence, each realization has the same permeability values at these locations of the measured data. Fig. 5.9 shows one realization of stochastic permeability field created by SGSIM for the simulation model.
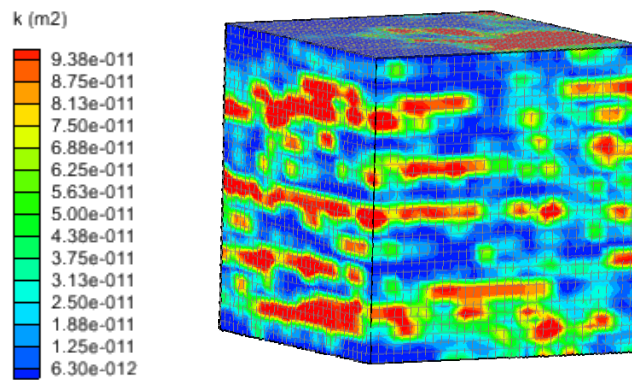
Fig. 5.9: Conditioned heterogeneous permeability field for the simulation model.

The buoyancy-driven gas flows are essentially determined by the geometry of clay lenses and thin layers of clay, which act as the gas barriers. Therefore, investigation of low permeable horizon becomes important and has to taken into account within a realistic model.

In this work, the measurements of DPEC and moisture sensors were used to determine the depth and the lateral extension of the low permeable layers. In Fig. 5.7, the horizons that show similar trend in gas saturation measurements of different scenarios, could indicate the same rock characterization. Based on the gas saturation measurement at TDR2, four horizons of low permeable layers (e.g., clay, silty-fine sand, and silty-medium gravel) were considered at the depth of 5, 5.8, 7.8 and 8 m.

Fig. 5.10 shows the measurements of DPEC at GP11, which represents the high variation of properties in vertical direction.

The clay content results in high values of electrical conductivity. Therefore at the location of GP11, the low permeable layers should be placed at the depth of 7 - 10 m, because the electrical conductivity of these depths shows significant increase. This investigation confirms that the low permeable layers are placed at the depth of 7.8 and 8 m, which was proposed based on the gas saturation measurement at TDR2.
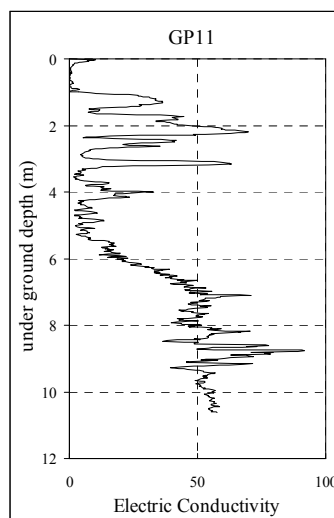
Fig. 5.10: Measurement of DPEC in vertical direction at GP11.

5.6   Simulation results and discussion

In this section, first the effect of heterogeneous fields created by SGSIM is presented, and then the effect of low permeable layers in vertical direction is investigated. Finally, one set of simulation result for different injection scenarios is illustrated.

Fig. 5.11 shows the distribution of gas saturation measured by the moisture sensor at TDR2 (green curve), and is compared with the theoretical gas saturations obtained from stochastic simulations (blue and red curves). The both theoretical curves were obtained based on two different realizations of stochastic permeability field, which are equal probable and based on the same constraints (i.e., mean value, variance and covariance function). But, distribution of simulated gas saturations in Fig. 5.11 reveals the effect of different realizations.
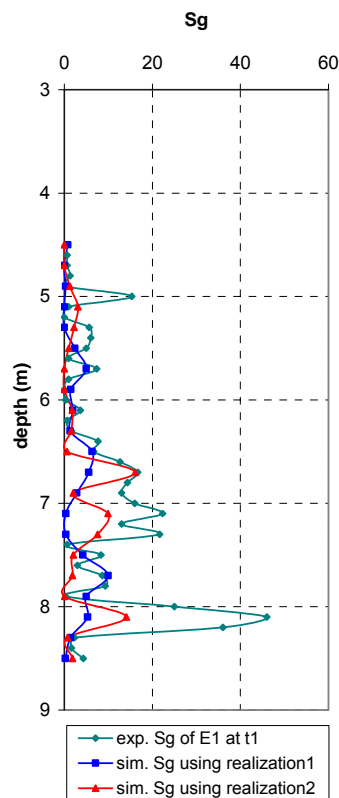
Fig. 5.11: Comparison of experimental gas saturation obtained at TDR2 with the simulated gas distribution created by two equal-probable realizations, for scenario E1 at interval time t_1.

The flow pattern in scenario E2 was incoherent bubbly flow and the continuum model cannot describe the incoherent flow due to the continuity assumptions. Therefore, the simulation results of scenarios E1, E3 and E4 (blue curves) are presented in Fig. 5.12 at time interval t_1, in which six rock types were considered in vertical direction.

The calculated curves are clearly showing the trend of experimental measurements in all scenarios. It is obvious that it is not possible to obtain the exact match for all experiments, but the simulation results are in reasonable agreement with the experimental gas saturation profile in Fig. 5.12.

The simulation results were visualized in 3D by Groundwater Modeling System (GMS 7.1, Aquaveo, LLC) that includes the interpolation algorithms. The interpolation algorithm helps to create the continuous distribution of multi-phase flow properties (e.g., gas saturation and, gas pressure and dissolved gas concentration).

Fig. 5.13 shows the 3D visualization of gas distribution obtained by stochastic simulation, when the layered heterogeneity in vertical direction and the stochastic heterogeneity in horizontal direction are applied.
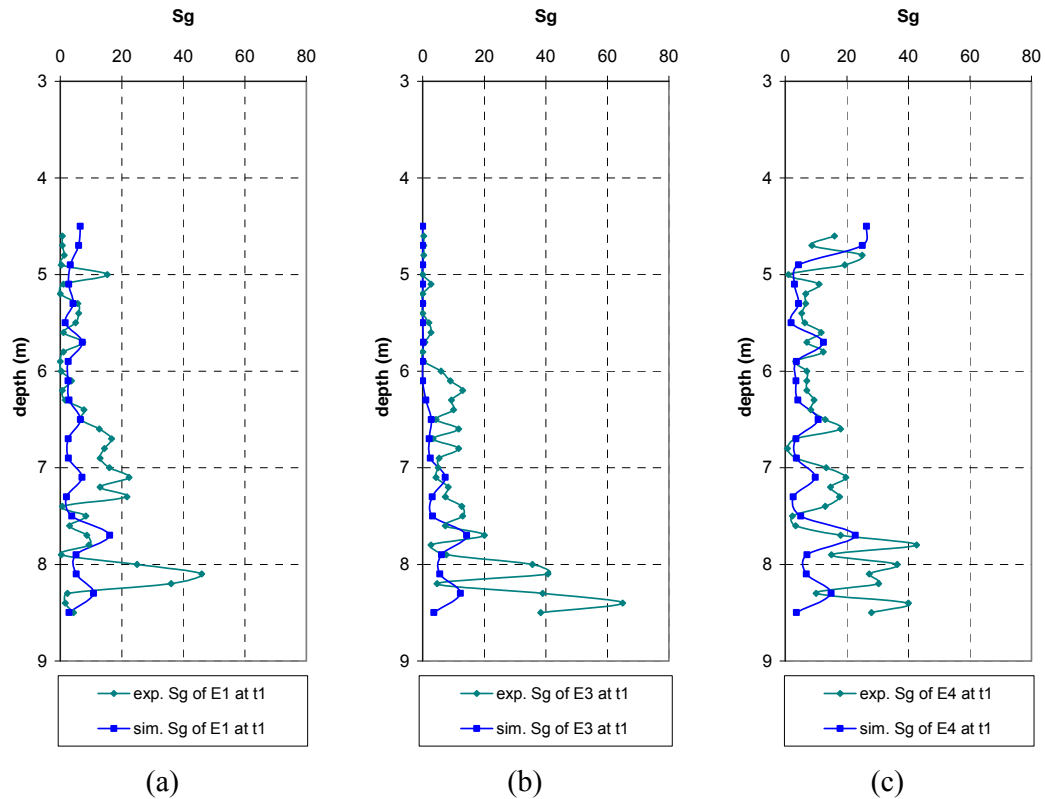
Fig. 5.12: Simulation results with R2 realization and five rock classes for all scenarios E 1.1, E 2.1, E 3.1 and E 4.1 from (a) to (d), respectively.

The results of gas injection at the test site show that, the incoherent flow pattern results in more trapped gas (see Fig. 5.7), while the stochastic simulation results in Fig. 5.13 revealed that coherent flow influences a wider zone (e.g., in scenario E2). Therefore, if a wide zone with high residual gas saturation is desired in test site, the gas should be injected with a combination of these two injection scenarios. Our experimental investigations in test site showed that LPI (e.g., injection rate less than 3 l/min) creates incoherent flow, and flow pattern in HPI (e.g.,, injection rate bigger than 25 l/min) is coherent flow.
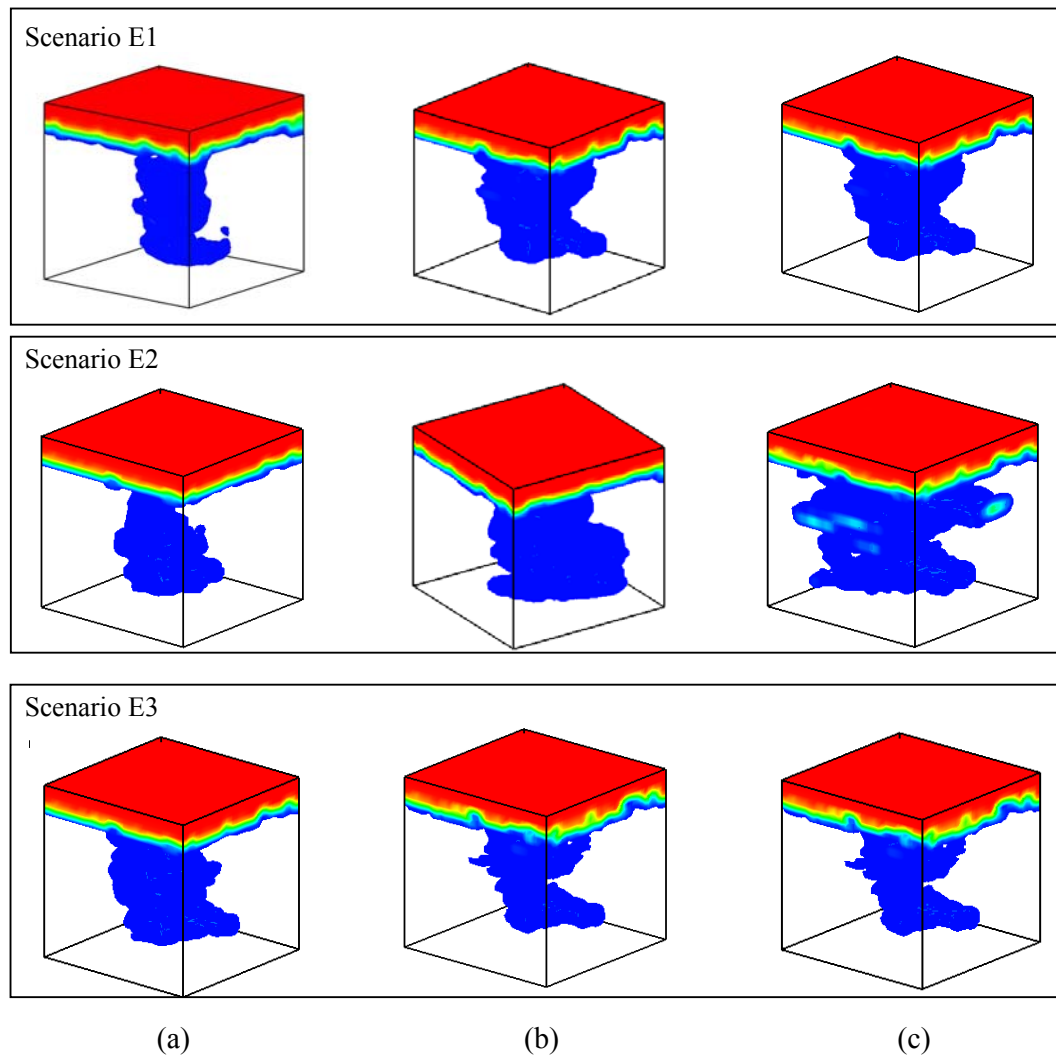
Fig. 5.13: The 3D visualization of gas saturation through the simulation model for scenarios E1, E3 and E4 at time intervals t_1, t_2 and t_3. The layered heterogeneity in vertical direction and stochastic heterogeneity in horizontal direction were applied.

5.7 Conclusions
The gas injection hypotheses at the Leuna test site were developed based on the results of gas injection in bench-scale experiments. The most important conclusions of modeling the gas injection at the field-scale are:

1. The discrete models (e.g., the pore network modeling or Lattice-Boltzmann simulation), which are usually used in simulation of small domains, cannot simulate the multi-phase flow occurred in large domains of field-scale. Therefore, continuum model, which handles the large numbers of grid blocks, was used to simulate the multi-phase flow occurred at the large domains in the field-scale.

2. The continuum model used to simulate the direct gas injection in HPI and coupled HPI/LPI should:
   (a) be a multi-phase flow model (i.e., the models that ignore the gas flow are not suitable, for instance the model applies the Richards equation).
   (b) take the heterogeneity in permeability and capillary pressure fields into account.
   (c) be able to use the field data (e.g., the geological data, the measured gas saturation during the injection) as conditioning parameters.

3. In general, minor changes in the permeability values result in strong differences in simulation results. The geological survey was used to create an accurate model that represent the fluid flow occurred at the test site. There is a common rule in this case: more geological data results in a successful forecast of gas dispersion in the subsurface simulation model. Due to the higher accuracy of geological information, which comes from the large number of installed sensors in the field, the final conclusions of this work are more reliable.

4. Applying the geological measurements alone does not give the perfect simulation results, which exactly match the experimental measurements, because of the complexity of the physical processes occurred within the porous medium. The inverse modeling should be applied to adjust and correct the estimated geological properties (e.g., the parameters of the relative permeability- and capillary pressure-saturation relationships).

5. The movement of gas plume by the buoyancy mostly depends on vertical permeability. Hence, the vertical and horizontal permeability should be implemented independently in numerical modeling. Although, the layering classification is used in this work to imply the effect of heterogeneity in vertical direction, but it is also possible to create the uncorrelated stochastic permeability field in vertical direction.

6. The optical system cannot be installed at the test site to track the 3D fluid flow in field-scale experiments. Hence, the simulation models can be used to create the gas distribution in 3D by the using the sensor measurements. The spatial gas distribution in 3D can be correlated to the heterogeneity in matrix, similar to the computer tomography (e.g. NMR and X-ray).

Therefore, the 3D simulation by the continuum model can be used to optimize the direct gas injection.

7. The stochastic simulations show the broad range of possible realistic gas distribution within a heterogeneous permeability field. As emphasized, the SGSIM takes into account all the available data (i.e., mean values and variances). In opposite, the standard deterministic layer approach takes only into account the mean value for each layer. Therefore, a stochastic simulation is superior to the deterministic approach.

8. Applying the stochastic heterogeneity creates one realization out of hundreds possible realizations. Therefore, the nature of creating a stochastic heterogeneous field poses nonstandard challenges in obtaining the exact gas flow pattern in test site. Consequently, the stochastic simulation may not give the exact gas distribution observed in experimental measurements. Since no exact simulation results can be obtained, the strategy is choosing the best estimation results.

6   Closure

6.1   Summary and Conclusions

This dissertation is intently focused on investigation and simulation of coherent channelized flow pattern that develops in direct gas injection in bench- and field-scale experiments.

Many authors (e.g., Lundegard and Andersen, 1996; McCray and Falta, 1997; Hein et al., 1997; van Dijke and van der Zee, 1998) stated that the continuum models are able to show the experimental gas distribution. While, several authors (e.g., Thomson and Johnson, 2000; Glass et al., 2000; Selker et al., 2007; Geistlinger et al., 2009) argued that the continuum model can only obtain the average flow properties and is not able to model the single stochastic gas channels. Therefore, the injection processes at bench- and field-scales were simulated by TOUGH2 program (Pruess, 1999) to examine the ability of continuum model in representing the coherent channelized flow pattern.

In Chapter 4, a 2D model was created to simulate the direct gas injection carried out by Krauss (2007) in bench-scale experiments. Since the key parameters of this model were estimated by experimental values, this model can describe the gas flow pattern that occurs in reality. The simulation results of continuum model using different constitutive relationships (van Genuchten-Mualem (1980) and Brooks-Corey model (1966)) showed that the continuum model can only describe the average flow properties, because it is based on the continuum assumption (i.e., it introduces effective properties at REV-scale).

The main conclusion of this work is that a good calibrated continuum model by a set of independent parameters (e.g., gas saturation, permeability, entry pressure, packing density) has an excellent prediction ability for average flow behavior. Both the area of influence and the important gas volume-injection rate dependence show an excellent agreement to the experimental values for the 0.5 mm- and 1 mm-GBS, respectively. Furthermore, this study shows for the first time that the constitutive relationship is crucial to simulate the gas distribution accurately. The van Genuchten-Mualem (1980) model, which is the standard constitutive relationship in the literature, yields a too wide gas plume and a smooth transition in gas saturation at the gas-water interface. Contrary, the Brooks-Corey model (1966) yields the sharp transition in the gas saturation that is experimentally observed. Consequently, the Brooks-Corey model is superior to the van Genuchten-Mualem model, since it considers the existence of a finite entry pressure (i.e., existence of an upper maximum radius in pore size distribution) and its results are more reasonable according to the experimental observations. However, the numerical solution of the Brooks-Corey model is sometimes unstable and the computer time at least doubles compared to the van Genuchten-Mualem model.

Since the porous media is heterogeneous, it is critical to apply the appropriate heterogeneity in simulation model that can represent the specification of flow properties occurred in reality. Applying different heterogeneity in simulation of gas injection in bench-scale experiments revealed that the continuum modeling with weak stochastic heterogeneity, which is created by a covariance function and the experimental variance, cannot represent the essential features of the experimental gas flow pattern. In other words, a continuum model applying weak heterogeneity can represent only the average parabolic-geometry of gas distribution, not the single stochastic gas channels.

Stauffer et al. (2009) argued that a continuum model that utilizes the sub-scale heterogeneity can obtain a reasonable description of channelized gas flow pattern. This statement was examined by using strong heterogeneous permeability and capillary pressure fields, which were created by a uniform pore size distribution. The quantitative comparison of the theoretical and experimental gas volumes showed that applying the sub-scale heterogeneity in continuum model gives too large gas volumes, although it can represent the stochastic channelized flow. These observations create a dilemma of the sub-scale continuum modeling.

The field-scale 3D simulation in Chapter 5 aimed to represent how the results in bench-scale can be generalized to the larger scales. Since the optical system cannot be installed at the test site to track the 3D fluid flow, the 3D simulation by the continuum model can be used to create the spatial gas distribution correlated to the heterogeneity in matrix, and to optimize the direct gas injection at test site.

Therefore, a 3D model was developed to simulate the injection processes, which were carried out at the Leuna test site. The geological information that was obtained by the large number of installed sensors at the test site, was used to create an accurate model. There is a common rule in this case: more geological data results in a successful forecast of gas flow in simulation model.

However, the geological survey was used to create an accurate model, but it cannot obtain the perfect simulation results due to the complexity of the physical processes occurred within the porous medium. Therefore, the inverse modeling should be applied to adjust and correct the estimated geological properties. In simulation of gas injection at Leuna test site, the inverse modeling was used to modify the geological properties (e.g., the parameters of the relative permeability- and capillary pressure-saturation relationships).

To apply the heterogeneity, the stochastic permeability field was created by SGSIM, which takes into account all the available data (i.e., mean values and variances). Since the movement of gas plume by the buoyancy forces mostly depends on vertical permeability, the vertical and horizontal permeability should be implemented independently in numerical modeling. In Chapter 5, the layering classification was used to imply the effect of heterogeneity in vertical direction. As the standard deterministic layer approach takes into account only the mean value for each layer, therefore the stochastic heterogeneity is superior to the deterministic approach.

The nature of creating a stochastic heterogeneous field is creating one realization out of hundreds possible realizations, that may pose nonstandard challenges in obtaining the exact gas flow pattern in test site. Since the stochastic simulation may not give the exact gas distribution observed in experimental measurements, the strategy is choosing the best estimation results.

6.2 Outlook

The results presented in this study deserve further investigations on simulation of direct gas injection in both bench-scale and field-scale. Some directions for future research include the following aspects:

1. The simulation of this work was restricted to a two-phase flow system that consists of gas and water. In gas injection process, which aims to remove the contaminants by bio-degradation processes, three-phase flow occurs due to the movement of gas, water and non-aqueous phases. Several studies have been done (e.g., by Juanes, 2003) to simulate the three-phase flow through the porous media, that can be utilize in simulation of bio-degradation processes. Although, three-phase flow model demands more detailed geological information and also higher computational time and cost.

2. For further work, creating a stochastic heterogeneous permeability field in vertical direction, which has a specific correlation length, may describe the buoyancy-driven flow better than the deterministic layer approach. Since the vertical permeability has lower degree of correlation, the Transition Probability Geo-statistical Software (TPROGS) can create the uncorrelated stochastic permeability values. TPROGS uses the rules of Markov chain model.

3. Whether TOUGH2 program is a well developed program, it is highly sensitive to the model parameters that may create a lots of convergence problems. The most important problem was the implementation of the heterogeneous fields. Working on TOUGH2-source code in order to handle the difficulties in numerical calculation would solve lots of simulation problem.

4. Further research is needed to solve the dilemma that involves the prediction ability of sub-scale modeling, which Stauffer et al. (2009) proposed to create the single stochastic gas channels: On the one hand the strong heterogeneity generates the stochastic gas channels, on the other hand this strong heterogeneity leads to too large gas volumes.

References

Adams, J. A., and Reddy, K. R. (1997): the effect of grain size distribution on air sparging efficiency. In situ and on-site bioremediation, vol. 1, ed. B. C. Alleman and A. Leeson, 165-172. Columbus, Ohio: Battelle Press.

Bachmat, Y., and Bear, J. (1986): Macroscopic modeling of transport phenomena in porous media. 1: The continuum approach. Transport in Porous Media, 1:213 –240.

Baviere, M. (2007): Basic Concepts in Enhanced Oil Recovery Processes, London, Elsevier Applied Science. ISBN 1-85166-617-6

Bear, J. (1972): Dynamics of Fluids in Porous Media, Environmental Science Series, Elsevier, New York. Reprinted with corrections, Dover, New York, 1988.

Beckmann, A. (2006): Direct Oxygen Injection Experiments and Investigation of Multi-Component Mass Transfer Processes, PhD Dissertation, Technischen Universität Bergakademie Freiberg, Freiberg

Bellin, A., and Rubin, Y. (1996): HYDRO_GEN: A new method for the generation of random functions, code description and user's guide, http://www.ing.unitn.it/~bellin/frames/hydrogen.php.

Bellin, A., and Rubin, Y. (1996): HYDRO_GEN: A spatially distributed random field generator for correlated properties, Stochastic Hydrology and Hydraulics 10:253-278, Springer-Verlag.

Brauns, J., And Wehrle, K. (1989): Untersuchung der Drucklufteinblasung in die gesättigte Bodenzone (In-situ-Strippen)-Modellversuche. Abschlußbericht zum Forschungsvorhaben (AZ: 12/0415.1) der Landesanstalt für Umweltschutz B.-W.; Karlsruhe, 56.

Brooks, M. C., Wise, W. R., and Annable, M. D. (1999): Fundamental changes in situ air sparging flow patterns, Ground Water Monitoring and Remediation, 19(2), 105-113.

Buckley, S., E., and Leverett, M., C. (1942): Mechanism of fluid displacement in sands, Trans. AIME, 146, 107-116.

Burdine, N. T. (1953), Relative permeability calculations from pore size distribution data, Trans. AIME, 198, 71.

Carcoana, A. (1992): Applied Enhanced Oil Recovery, Prentice Hall, ISBN 0-13-044272-0.

Chatzis, I., Morrow, N. R., and LIM, H.T. (1983): Magnitude and Detailed Structure of Residual Oil Saturation. Soc. of Petroleum Engineers J. 23(2), p. 311-326.

Chen, M. R., Hinkley, R. E., and Killough, J. E. (1996): Computed tomography imaging of air sparging in porous media, Water Resources Research, 32 (10): 3013-3024.

Christy, C. D., Christy, T. M., and Wittig, V. (1994): A percussion probing tool for the direct sensing of soil conductivity, in Proceedings of the 8th national outdoor action conference, National Ground Water Association, Columbus, OH.

Cinar, Y., Riaz, A., and Tchelepi, H.A. (2008): Experimetal study of CO2 injection into saline formations, SPE journal, July 2008.

Clayton, W. S. (1998): Afield and laboratory investigation of air fingering during air sparging, Ground Water Monit. and Rem., 18 (3) (1998), 134–145.

Corey, A. T. (1977): Mechanics of heterogeneous fluids in porous media. Water Resour Publ, Fort Collins (CO); 1977.

Dror, I., Berkowitz, B., and Gorelick, S. M. (2004): Effects of air injection on flow through porous media: Observations and analyses of laboratory-scale processes. Water Resources Research, 40 (9), doi: 10.1029/2003WR002960.

Elder, C. R., and Benson, C. H. (1999): Air channel formation, size, spacing, and tortuosity during air sparging, Ground Water Monitoring and Remediation, 19 (3): 171-181.

Fields, K. Gibbs, J., Condit, W. (2002): Air Sparging: A Project Manager's Guide, Batelle Press, Columbus, Ohio.

Finneran, K. T., and Lovley, D. R. (2001): Anaerobic degradation of methyl tert-butyl ether (MTBE) and tert-butyl alcohol (TBA). Environ. Sci. Technol., 35 (9), 1785-1790.

Fry, V. A., Selker, J. S., Gorelick, S. M. (1997): Experimental investigations for trapping oxygen gas in saturated porous media for in situ bioremediation. Water Resour. Res., 33 (12), 2687-2696.

Geistlinger, H., Beckmann, A., Lazik, D. (2005): Mass Transfer between a Multi-Component trapped Gas Phase and a mobile Water Phase: Experiment and Theory. Water Resour. Res., vol. 41, W11408, doi:10.1029/2004WR003885.

Geistlinger, H., Krauss, G., Lazik, D., Luckner, L. (2006): Direct gas injection into saturated glass beads: Transition from incoherent to coherent gas flow pattern. Water Resour. Res., vol. 42, W07403, doi:10.1029/2005WR004451.

Geistlinger, H., Lazik, D., Krauss, G., Vogel, H-J (2009): Pore-scale and continuum modeling of gas flow pattern obtained by high-resolution optical bench-scale experiments. Water Resour. Res., vol. 45, W04423, doi:10.1029/2007WR006548.

Gomez-Hernandez, J. J., and Journel, A. G. (1993): Joint sequential simulation of multi-Gaussian fields, Soarez A, editor. Troja'92, vol. 1, Kluwer Academic Publisher; p. 85–94.

Hein, G. L., Gierke, J. S., Hutzler, N. J., Falta, R. W. (1997): three-dimensional experimental testing of a two-phase flow-modeling approach for air sparging, Ground Water Monit. and Rem., 1997, 222–230.

Ho, C. K., and Webb, S. W. (2006): Gas Transport in Porous Media, Elsevier, Amsterdam.

Hoeppel, R. E., Hinchee, R. E., Arthur, M. F. (1991): Bioventing of soils contaminated with petroleum hydrocarbons. J. Indust. Microbio., 8, 141-146.

Honarpour, M., Koederitz, L., Harvey, A. H. (1986):Relative permeability of petroleum reservoirs, C.R.C. Press, Boca Raton, Florida, ISBN: 084935739X.

Johnson, R. L., Johnson, P. C., McWhorter, D. B., Hinchee, R. E., Goodman, I. (1993): An overview of in situ air sparging, Ground Water Monit. Rem., 13 (4), 127-135.

Juanes, R. (2003): Displacement theory and multiscale numerical modeling of three-phase flow in porous media, PhD Dissertation, University of California, Berkeley.

Kosugi, K. (1996), Lognormal distribution model for unsaturated soil hydraulic properties, Water Resour. Res., 32(9), 2697–2703, doi:10.1029/96WR01776.

Krauss, G. (2007): Direkt-Gasinjektion in wassergesättigte poröse Medien: Visualisierung und Quantifizierung von Gas-Phasen-Verteilung und –Bewegung, PhD Dissertation, Technischen Universität Bergakademie Freiberg, Freiberg

Lazik, D., Geistlinger, H., Krauss, G., Beckmann, A., and Schirmer, M. (2002): Untersuchungen zum Strömungsverhalten und zur Lösungskinetik von Gasen im Mehrphasensystem Aquifer. Grundwasser, 7 (3): 146-155.

Lee, M. D., and Raymond, R. L. (1991): Case history of the application of hydrogen peroxide as an oxygen source for in situ bioreclamation. In in situ bioreclamation applications and investigations for hydrocarbon and contaminated site remediation, Hinchee, R. E., and Olfenbuttel, R. F., eds., Butterworth-Heinemann, Boston, MA, pp. 429-436.

Leverett, M. C. (1940): Capillary behavior in porous solids, AIME, vol. 142, pages 152-169, paper number 941152-G.

Li, K., and Horne, R. N. (2006): Comparison of methods to calculate relative permeability from capillary pressure in consolidated water-wet porous media, Water Resource Research, vol. 42, W06405, doi: 10.1029/2005WR004482.

Luckner, L.; Ehbrecht, H.; Rößner, U. (2001): In situ-Reinigung kontaminierter anoxischer Grundwasserleiter durch sauerstoffangereichertes Infiltrationswasser. Wasser Abwasser, 142 (11), 774-781.

Lundegard, P.D and Andersen, G. (1996): Numerical simulation of air sparging performance. In: Proceedings of the Petroleum Hydrocarbons and Organic Chemicals in Ground Water: Prevention, Detection, and Restoration Conference. Natl. Ground Water Assoc., Dublin, OH, pp. 461-476.

McCray, J.E. (2000): Mathematical modeling of air sparging for subsurface remediation: state of the art, Journal of Hazardous Materials, 72 (2000) 237–263.

McCray, J. E., and Falta, R. W. (1997): Numerical simulation of air sparging for remediation of NAPL contamination, Ground Water, 35(1), 99– 110.

McWhorter, D. B., and Sunada, D. (1990): Exact integral solutions for two-phase flow, Water Resources Research, vol. 26, No. 3, pages 399-413, March 1990.

Morrow, N. R., and Songkran, B. (1981): Effects of viscous and buoyancy forces on non-wetting phase trapping in porous media. In: D.O. Shah, (Ed.), Surface Phenomena in Enhanced Oil Recovery, Plenum Press, New York, NY, 1981.

Mualem, Y. (1976): A new model for predicting the hydraulic conductivity of unsaturated porous media. Water Resour Res, 12:513–22.

Muskat, M. (1949): Physical Principles of Oil Production, McGraw-Hill, New York.

Nyer, E. K., Davis, J. S., and King, I. (2002): Oxygen revisited. Ground Water Monit. Rem., 22 (3), 44-49.

Pan, C., Hilpert, M., and Miller, C. T. (2004): Lattice-Boltzmann simulation of two-phase, Water Resource Research, vol. 40, W01501, doi:10.1029/2003WR002120.

Parker, J. C., R. J. Lenhard, and T. Kuppusamy (1987), A parametric model for constitutive properties governing multiphase flow in porous media, Water Resour. Res., 23(4), 618– 624.

Peterson, J. W., Lepczyk, P. A., and Lake, K. L. (1999): Effect of sediment size of influence during groundwater remediation by air sparging: A laboratory approach, Environ. Geology 38(1), p. 1-6.

Pennell, K. D., Abriola, L. M., Pope, G. A. (1996): Influence of viscous and buoyancy forces on the mobilization of residual tetrachloroethylene during surfactant flushing. Environmental Science and Technology, 30 (4): 1328-1335.

Peterson, J. W., Murray, K. S., Tulu, Y. I., Peuler, B. D., and Wilkens, D. A. (2001): Airflow geometry in air sparging of fine-grained sands, Hydrogeology Journal, 9 (2): 168-176.

Peterson, J. W. and Murray, K. S. (2003): Grain-size heterogeneity and subsurface stratification in air sparging of dissolved-phase contamination: Laboratory experiments-field implications, Environmental and Engineering Geoscience, 9 (1): 71-82.

Pruess, K., Oldenburg, C., Moridis, G. (1999): TOUGH2 user's guide, version 2.0, Rep. LBNL-43134, Lawrence Berkeley Natl. Lab., Berkeley, California.

Purcell, W. R. (1949): Capillary pressures—Their measurement using mercury and the calculation of permeability, Trans. AIME, 186, 39.

Reddy, K. R., and Adams, J. A. (2001): Effects of soil heterogeneity on airflow patterns and hydrocarbon removal during in situ air sparging. Journal of Geotechnical and Geoenvironmental Engineering, 127 (3): 234-247.

Reddy, K. R., and Adams, J. A. (2000): Effect of groundwater flow on remediation of dissolved-phase VOC contamination using air sparging. Journal of Hazardous Materials, 72 (2-3): 147-165.

Rogers, S. W., and Say Kee, O. (2000): Influence of porous media, airflow rate, and air channel spacing on benzene NAPL removal during air sparging. Environmental Science and Technology, 34 (5): 764-770.

Roosevelt, S. E., and Corapcioglu, M. Y. (1998): Air bubble migration in a granular porous medium: Experimental studies, Water Resources Research, 34 (5): 1131-1142.

Rosetta database (Schaap, University of Arizona, 2002, free download from http://www.cals.arizona.edu/research/rosetta/index.html

Roth, K. (2006): Soil Physics, Lecture Notes, Institute of Environmental Physics, University of Heidelberg, v1.0

Rubin, Y. (2003): Applied stochastic hydrogeology, University Press.

Saadatpoor, E., Bryant, S. L., Sepehrnoori, K. (2009): Effect of capillary heterogeneity on buoyant plumes; a new local traping mechanism, GHGT 2009, Energy Procedia, 1 (2009) 3299-3306.

Sahimi, M. (1995): Flow and Transport in Porous Media and Fractured Rock, 482 pp., John Wiley, Hoboken, N.J.

Schirmer, M. (2001): Assessment and implementation of in situ groundwater remediation approaches, Habilitation, University of Tübingen.

Selker, J. S., Niemet, M., McDuffie, N. G., Gorelick, S. M. and Parlange, J. Y. (2007): The local geometry of gas injection into saturated homogeneous porous media, Transport Porous Media, 68(1), 107 – 127, doi:10.1007/ s11242-006-0005-0.

Semer, R., Adams, J. A., and Reddy, K. R. (1998): An experimental investigation of air flow patterns in saturated soils during air sparging, Geotech. Geol. Eng. 16, 59–75.

Semprini, L., Roberts, P. V., Hopkins, G. D., McCarty, P. L. (1990): A field evaluation of in situ biodegradation of chlorinated ethenes: Part 2, results of bio-stimulation and biotransformation experiments. Ground Water, 28 (5), 715-727.

Stauffer, F., Kong, X.Z., and Kinzelbach, W. (2009): A stochastic model for air injection into saturated porous media, Advances in Water Resources, 32 (2009) 1180–1186, doi:10.1016/j.advwatres.2009.03.010.

Thomson, N.R., and Johnson, R.L. (2000): Air distribution during in situ air sparging: an overview of mathematical modelling, Journal of Hazardous Materials, 72 (2000) 265–282.

Unger, A. J. A., Sudicky, E. A., and Forsyth, P. A. (1995): Mechanisms controlling air sparging for remediation of heterogeneous formations contaminated by dense non-aqueous phase liquids, Water Resources Research, 31(8), 1913-1925.

U.S. Department of Agriculture (USDA) (1951): Soil survey manual, U.S.Dep. Agric. Agric. Handb., 18, 503 pp.

Van Dijke, M. I. J., van der Zee, S. E. A. T. M. (1998): Modelling of air sparging in a layered soil; numerical and analytical approximations, Journal of Geophysical Research, vol. 34, No. 3, pages 341–353.

van Genuchten, M.T. (1980): A closed-form equation for predicting the hydraulic conductivity of unsaturated soils. Soil Sci. Soc. Am. J. 44:892–898.

Vinsome, P. K. W. and Shook, G. M. (1993): Multi-purpose simulation, J. Pet. Sci. Eng., 9: 29-38.

Vogel, H-J., Tölke, J., Schulz, VP., Krafczyk, M., and Roth, K. (2005): Comparison of a Lattice–Boltzmann model, a full-morphology model, and a pore network model for determining capillary pressure–saturation relationships. Vadose Zone Journal, vol. 4, page 380–388, doi:10.2136/vzj2004.0114.

Vogel, H.-J., Weller, U., and Schlüter, S. (2010): Quantification of soil structure based on Minkowski functions, Computers and Geosciences, Volume 36 (10), 1236-1245, doi:10.1016/j.cageo.2010.03.007.

Weber, L. (2007): Untersuchungen zur Direktgasinjektion im Aquifer in Technikum- und Feld-Maßstab, PhD Dissertation, Technischen Universität Bergakademie Freiberg, Freiberg.

Wilson, R. D., Mackay, D. M., Cherry, J. A. (1997): Arrays of unpumped wells for plume migration control by semi-passive in situ remediation, Ground Water Monit. Rem., 17 (3),185-193.

Wong, R. C. K., and Wibowo, R. (2000): Tomographic evaluation of air and water flow patterns in soil column, Geotechnical Testing Journal, 23 (4): 413-422.

Curriculum Vitae

Surname:	Samani
First name	Shirin
Date of birth:	22 March 1983
Citizen of:	Iran

Education

2008– Present	PhD candidate Technischen Universität Bergakademie Freiberg, Freiberg, Germany
2005 – 2007	M.Ing. in Reservoir Engineering (GPA: 3.7/4) University of Calgary, Calgary, Alberta M.Sc. In Reservoir Engineering (GPA: 3.7/4) Petroleum University of Technology, Tehran, Iran
2001 - 2005	B.Sc. in Reservoir Engineering (GPA: 3.6/4) Petroleum University of Technology, Ahwaz, Iran

Scientific Carrier

May 2008–December 2011	**Researcher** Department of Soilphysics, Helmholtz Zentrum für Umweltforschung-UFZ Halle, Germany
April–June 2010 September–February 2010	**Teaching Assistant** Course: Remediation of groundwater contamination; Innovative Technologies Location: Thechnische Universität Bergakademie Freiberg, Germany Instructor: Prof. Helmut Geistlinger at Technical University of Freiberg
March 2008	**Teaching Assistant** Course: Advanced Well Test Analysis and Reservoir Engineering Location: Petroleum University of Technology, Iran Instructor: Prof. M. Pooladi-Darvish at University of Calgary
January–December 2007	**Research Assistant** Location: Tehran Research Center, Tehran, Iran Advisor: Prof. M. Pooladi-Darvish, Dr. R. Kharrat, and Dr. B. Rostami Research Area: Gas Assisted Gravity Drainage; conceptual modeling

Declaration

I hereby declare that I completed this work without any improper help from a third party and without using any aids other than those cited. All ideas derived directly or indirectly from other sources are identified as such.
In the selection and in the use of materials and in the writing of the manuscript I received support from the following person:
Prof. Dr. Helmut Geistlinger

Persons other than those above did not contribute to the writing of this thesis. I did not seek the help of a professional doctorate-consultant. Only persons identified as having done so received any financial payment from me for any work done for me.
This thesis has not previously been submitted to another examination authority in the same or similar form in Germany or abroad.

Shirin Samani
Halle (Saale), 03.11.2011